Detailed nacelle dynamics

Hansen, Anders Melchior

Published in:
Research in aeroelasticity EFP-2006

Publication date:
2007

Document Version
Publisher's PDF, also known as Version of record

Risø-R-Report

Research in Aeroelasticity EFP-2006

Edited by Christian Bak

Risø-R-1611(EN)

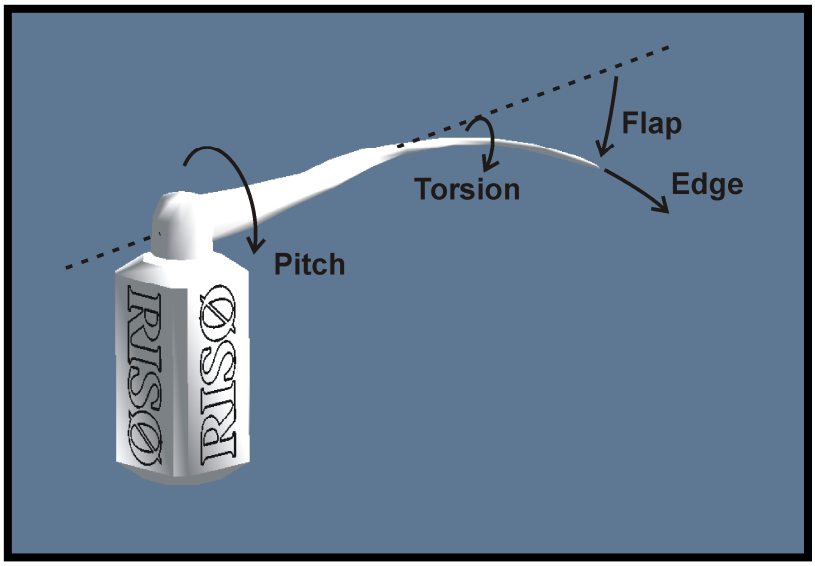

Risø National Laboratory
Technical University of Denmark
Roskilde, Denmark
July 2007

Author: Edited by Christian Bak
Title: Research in Aeroelasticity EFP-2006
Department: Wind Energy Department

Risø-R-1611(EN)
July 2007

Abstract :
This report contains the results from the Energy Research Project ”Program for Research in Applied Aeroelasticity, EFP-2006” covering the period from 1. April 2006 to 31. March 2007. A summary of the main results from the project is given in the following. The aerodynamics for rotors incl. spinner and winglets were clarified and the needed premises for an optimal rotor were explained. Also, the influence of viscous effects on rotor blades was investigated and the results indicated a range of optimum tip speed ratios. The use of winglets for wind turbine rotor was investigated and it was found that they can be used successfully, but that down-wind and short winglets are most efficient. Investigating a strategy for reduction of loads and vibrations at extreme wind speeds showed that there are considerably uncertainties in the numerical models and that the main concluding remark is that measurements on a real blade or a real turbine are needed to further conclude the investigation.

In the study of flutter and other torsional vibrations of blades at large deflections, modeling and analysis of the dynamics of a hydraulic pitch system for a 5 MW wind turbine was carried out. It was shown that the compressibility of the hydraulic oil introduced a dynamic mode in the pitch bearing degree of freedom. Also, investigating flutter for blades at large deflections showed that the flutter limit for a 5MW blade was moved significantly compared to blades without large deflections. The influence of modeling nacelle components was investigated by developing a generalized method to interface dynamic systems to the aeroelastic program HAWC2 and by exemplify by modeling the nacelle of an aeroelastic wind turbine model in a more detailed way by including a single planet stage of a gearbox. This simplified gearbox model captures in essence the splitting of the driving torque from the rotor shaft to the frame of the nacelle and to the generator.

Investigating the influence of wind shear on power and the interaction with cyclic pitch showed that there is a considerable uncertainty in modeling this rather common inflow case for a rotor. The implementation of the BEM model to handle this flow case can be carried out in different ways and the results of two advanced models have not so far been validated. In the new Aeroelastic Research Programme EFP2007 the investigations will be continued and the aspect of influence of individual pitch control on the blades will also be considered.

ISSN 0106-2840
ISBN 978-87-550-3610-9

Contract no.:
ENS 033001/33032-0083

Group's own reg. no.:
1110057-01

Sponsorship:
Danish Energy Authorities

Cover :
From Figure 7-4, page 76 in Chapter 7 “Dynamics of a hydraulic pitch system”

Pages: 118
Tables: 6
References: 79

Information Service Department
Risø National Laboratory
Technical University of Denmark
P.O.Box 49
DK-4000 Roskilde
Denmark
Telephone +45 46774004
bibl@risoe.dk
Fax +45 46774013
www.risoe.dk

Contents

Preface

The Energy Research Project "Program for Research in Applied Aeroelasticity, EFP-2006" was carried out in cooperation between Risø National Laboratory and the Technical University of Denmark (DTU) from 1 April 2006 to 31 March 2007. From the onset of the project, six milestones were defined which represent the main areas of the research activity. Apart from the work on the milestones, also analyses of current problems and further development of the existing models were carried out.

Several researchers at the DTU and Risø have been involved in the project work and have contributed to the research presented in this report. To enable reference to the different parts of the report, the names of the authors are indicated for each chapter. It should, however, be emphasized that the report is not a detailed report of the complete activity within the project. Thus, not all of the contributors to the project appear as authors to the different chapters. For a detailed description of the results from the project, please see Chapter 11, in which a complete list of publications in the project can be found.

At DTU, the following researchers from the Fluid Mechanics Section of the Department of Mechanical Engineering have been involved in the project:

Kurt S. Hansen
Martin O.L. Hansen
Robert Mikkelsen
Wen Zhong Shen
Jens Nørkær Sørensen
Niels Troldborg
Stig Øye

At Risø, the following researchers from the Aeroelastic Design Group have contributed to the project:

Peter B. Andersen
Christian Bak
Franck Bertagnolio
Thomas Buhl
Mac Gaunaa
Anders M. Hansen
Morten H. Hansen
Jeppe Johansen
Gunner C. Larsen
Torben J. Larsen
Helge A. Madsen
Helen Markou
Flemming Rasmussen
Niels N. Sørensen
Kenneth Thomsen

1 Summary

This report contains the results from the Energy Research Project "Program for Research in Applied Aeroelasticity, EFP-2006" covering the period from 1. April 2006 to 31. March 2007. The project partners are Risø National Laboratory and The Technical University of Denmark (DTU). The overall objectives of the project are to ensure the development of an aeroelastic design complex, which can provide the basis for the next generation of wind turbines and make new design concepts possible. The project forms a strategic cooperation between Risø, DTU and the wind turbine industry with emphasis on obtaining a suitable balance between long-term strategic research, applied research and technological development. To obtain synergy between the different subjects and to ensure an optimal, dynamic cooperation with the industry, while maintaining the continuity of the research, the project is organized as a research program within applied aeroelasticity with a combination of research activities with specific short-term targets within one year and general continuous long-term research activities. This research project has been the ninth in a row of one-year projects, which has ensured a continuous development since 1997, where the activity in this row of projects is described in [1], [2], [3], [4], [5], [6], [7] and [8].

Risø and DTU develop an aero-elastic design complex which provides the basis for the next generation of wind turbines

1.1 Main results from the project

The main emphasis of the activity in the project was put on the milestones which were defined in the project proposal. Furthermore, there has been activity on the further development of tools and models in "the aeroelastic design complex" which consists of 3D Navier-Stokes models, aeroacoustic models, airfoil- and blade design, aeroelastic codes and loads, aeroelastic stability, control and new concepts. Also, there have been investigations of subjects of fundamental character, which often constitute long-term research, e.g. correction of the BEM model concerning the radial variation in induction. A summary of the main results from the project is given in the following, however with a milestone concerning wind tunnel tests that has been postponed one year.

A new analytical method to determine the loading on an optimum wind turbine rotor has been developed

Clarification of the aerodynamics for rotors incl. spinner and winglets

The investigations are divided into three parts: 1) The optimum rotor, 2) Key parameters in aerodynamic rotor design and 3) Winglets.

1) A new analytical method to determine the loading on an optimum wind turbine rotor has been developed. The method enables to determine the optimum circulation distribution from Goldstein's function at all operating conditions. The proposed procedure for calculation of Goldstein's function and corresponding torque and thrust coefficients completes the traditional theory. The optimum characteristics are given as a function of the pitch of the wake.

Investigating the influence of tip speed ratio and Reynolds number on aerodynamic rotor design showed that rotors should not rotate too fast

2) The influence of the tip speed ratio and the Reynolds number on power efficiency was investigated. It showed that for 2D airfoil sections with c_l-c_d ratio between 50 and 200 the local speed ratio should be between 2.4 and 3.8 to obtain maximum local power efficiency. Also for the 2D case, it showed that the Reynolds number was very important for the airfoil performance with variations in c_l-c_d ratio between 50 and 180 for Reynolds numbers between 200.000 and 9mio. Investigation of C_P for rotors with three blades was made and showed that with the assumption of constant maximum c_l/c_d along the entire blade, the design tip speed ratio changed from X_{design}=6 to X_{design}=12 for c_l/c_d=50 and

c_l/c_d=200, respectively, with corresponding values of C_P=0.46 and C_P=0.525. Thus the design tip speed ratio and C_P are very dependent on the airfoil efficiency. For real rotors with requirements to airfoil thicknesses the investigation showed that rotors in the 1kW size should be designed with a tip speed ratio of 5.5 whereas rotors in the 5MW size should be designed with tip speed ratios between 6.5 and 8.5.

Investigating the use of winglets with a free-wake lifting-line model showed that winglets could increase power efficiency

3) The investigation of the use of winglets on wind turbine rotors showed that winglets can be used successfully to increase the power efficiency. The investigation also showed that the positive effect of winglets on power production is due to a reduction of tip losses, and is not connected with a downwind shift of wake vorticity. In the study a new free-wake lifting line code was developed, and comparisons with CFD computations on an optimal non-wingletted wing showed remarkable agreement between the results. The specific results from the investigation were that:

- downwind winglets are more effective than upwind ones of the same length
- The increase in power using winglets is smaller than what may be obtained by extending the wing radially with the same length. However, for small winglets (<2%), the same increase can be obtained for a corresponding increase in radius using downwind winglets
- The results are not very dependent on the radius of the bend between the main wing and the winglet, but the efficiency increases slightly for bend radii above 25% of the winglet height for the 2% downwind winglet case investigated

Strategy for reduction of loads and vibrations at extreme wind speeds (parked rotor/idling)

Edgewise blade vibrations in stand still was investigated and showed the need for measure-ments on a real wind turbine

There are a number of ways to circumvent edgewise vibrations depending on whether the problem is believed to be physical or of a purely numerical nature. If the problem is purely numerical, the models in the aeroelastic codes must be refined. This is continuously being done e.g. by implementing a dynamic deep stall model. However, if the problem is believed to have a real-life counterpart, active control of e.g. pitch angle or yaw angle could be adopted. Aeroelastic computations showed that there is a large deviation from the mean yaw moment for the minimum and maximum moments in the regions where negatively damped edgewise vibrations are seen. This could be used in an active control of the turbine to avoid the critical AOA. Idling speeds in the excess of 25% of the maximum tip speed resulted in a positively damped edgewise vibration for this wind turbine operating at a certain angle of attack. However, idling in wind speeds of 50 m/s with 25% of the maximum tip speed can cause other critical loads which need to be investigated. The main concluding remark must be that measurements on a real blade or a real turbine are needed to further conclude this investigation.

Flutter and other torsional vibrations of blades at large deflections

A hydraulic pitch system was modeled, which showed that the compres-sibility of the oil introduced a dynamic mode in the pitch bearing

Modeling and analysis of the dynamics of a hydraulic pitch system for a 5 MW wind turbine was carried out. It was shown that the compressibility of the hydraulic oil introduces a dynamic mode in the pitch bearing degree of freedom. This mode may obtain a negative damping if the proportional gain on the actuator position error is defined too large relative to the viscous forces in the hydraulic system and the total rotational inertia of the pitch bearing degree of freedom. A simple expression for the stability limit of this proportional gain was derived which can be directly used for tuning the gain based on the Ziegler-Nichols method. Computation of the transfer function from a harmonic pitch reference signal to the actual pitch response indicated that the hydraulic

pitch system can be approximated as a low-pass filter with some appropriate limitations on pitching speed and acceleration. The structural model of the blade includes the geometrical coupling of edgewise bending and torsion for large flapwise deflections. This coupling is shown to introduce edgewise bending response of the blade for pitch reference oscillations around the natural frequency of the edgewise bending mode, in which frequency range the transfer function from reference to actual pitch angle cannot be modeled as a simple low-pass filter.

Investigation of flutter for blades with large deflections showed that blade deformations has a strong effect on the dynamics of the blade

An investigation of flutter for blades with large deflections showed that blade deformation which can occur at normal operation of a turbine has a strong effect on the dynamics of the blade.

- The undeformed blade has a flutter instability at rotational speeds above approximately two times the maximum tip speed. The same route to flutter for the pre-deformed blade is delayed such that it becomes instable at approximately 2.4 times the maximumn tip speed, which is a 23 % higher rotational speed.
- The deformation of the blade introduces a new route to flutter, which becomes unstable at around 1.7 times the maxium tip speed, i.e., a 16 % lower rotation speed compared to the flutter instability for the undeformed blade.
- Furthermore, the first edgewise dominated mode couples to the first flapwise motion and becomes increasingly negatively damped for increasing rotational speed.

The influence of modelling nacelle components

An inclusion of a simplified gear box model in the aeroelastic code HAWC2 resulted in altered dynamics of the nacelle components

A generalized method to interface dynamic systems to the aeroelastic program HAWC2 has been developed. The method has been examplified by modeling the nacelle of an aeroelastic wind turbine model in a more detailed way by including a single planet stage of a gearbox. This simplified gearbox model captures in essence the splitting of the driving torque from the rotor shaft to the frame of the nacelle and to the generator.

It was shown that the inclusion of the simplified gearbox model results in altered dynamics of the nacelle components where the free-free vibration mode of the drive train contributes more to both the shaft torque and the tower top moment responses and therefore also to the internal gearbox stresses.

The results were based on a simplified gearbox model, however, any gearbox model which can be formulated as a set of differential equations can now be interfaced to the aeroelastic model in HAWC2. This makes it possible to base future conclusions on even more detailed gearbox models with more degrees of freedom and to include dynamic models of e.g. the generator and the electrical grid.

Finally, a parameter study of the dynamics of the support structure was made. It was found that for realistic values of mass and stiffness associated with ring wheel rotation, two eigenfrequencies may appear in the low frequency range (both were a kind of free-free modes which differ in the way the ring wheel rotates). This should be considered in the design of the drive train.

Investigating the wind shear showed considerably uncertainty in the modeling of a rather common inflow case

The influence of wind shear on power and the interaction with cyclic pitch

The investigation of the influence of wind shear in the inflow showed that there is a considerable uncertainty in modeling a rather common inflow case for a rotor. The implementation of the BEM model to handle this flow case can be carried out in different ways, and the results of two advanced models have not so far been validated. In the new Aeroelastic Research Programme EFP2007 the investigations will be continued,

and the aspect of influence of individual pitch control on the blades will also be considered.

1.2 References

[1] Madsen, H.A. (Red.) ”Forskning i Aeroelasticitet. Rapport for EFP-97” (in Danish), Risø-R-1066(DA), Forskningscenter Risø, Roskilde, August 1998

[2] Madsen, H.A. (Red.) ”Forskning i Aeroelasticitet – EFP-98” (in Danish), Risø-R-1129(DA), Forskningscenter Risø, Roskilde, August 1999

[3] Madsen, H.A. (Red.) ”Forskning i Aeroelasticitet – EFP-99” (in Danish), Risø-R-1196(DA), Forskningscenter Risø, Roskilde, November 2000

[4] Madsen, H.A. (Red.) ”Forskning i Aeroelasticitet – EFP-2000” (in Danish), Risø-R-1272(DA), Forskningscenter Risø, Roskilde, Juli 2001

[5] Madsen, H.A. (Red.) ”Forskning i Aeroelasticitet EFP-2001” (in Danish), Risø-R-1349(DA), Forskningscenter Risø, Roskilde, December 2002

[6] Bak, C. (Red.) ”Forskning i Aeroelasticitet EFP-2002” (in Danish), Risø-R-1434(DA), Forskningscenter Risø, Roskilde, Februar 2004

[7] Bak, C. (Red.) ”Forskning i Aeroelasticitet EFP-2004” (in Danish), Risø-R-1509(DA), Forskningscenter Risø, Roskilde, Maj 2005

[8] Bak, C. (Ed.) ”Research in Aeroelasticity EFP-2005”, Risø-R-1559(EN), Risø National Laboratory, Roskilde, Denmark, May 2006

2 Two modifications of the BEM method based on validation with results of actuator disc simulations

Helge Aagaard Madsen

In the Aeroelastic Research Programme EFP-2005 [1] a comprehensive investigation of the blade element momentum (BEM) model was carried out based on comparisons with numerical actuator disc (AD) simulations. The objective was to investigate in particular the inboard rotor aerodynamics initiated by the new rotor designs of Enercon with big root chords, and with the blade root ending on the spinner. The main result of this investigation was that the BEM model underestimates the local *CP* on the inner part of the blade because the effect of the pressure variation from the rotation of the wake is disregarded in the BEM model. However, it was also shown, by comparisons with numerical actuator disc results, that in general the integrated *CP* for the whole rotor was in good correlation with the numerical AD results because the BEM model overestimates the *CP* on the outboard part of the rotor. The causes of this deviation have been further investigated in the present project, and a correction model to the BEM model has been developed which compensates for this deviation. A correction model to BEM for the influence of the pressure from the wake rotation was already presented in the EFP-2005 project [1] and it means that two corrections models are now available for the BEM model, which increases the correlation of this model with numerical AD results substantially. These models will be presented below.

The BEM model underestimates local CP on the inboard part of the rotor and overestimates in the tip region.

2.1 The main deviations between BEM results and numerical AD results

To illustrate the overall tendency in the deviations between the BEM model and AD simulations, a comparison is made of the results for a constant rotor loading of 0.95 on the main part of the rotor, which decreases linearly to zero at the root of the blade to

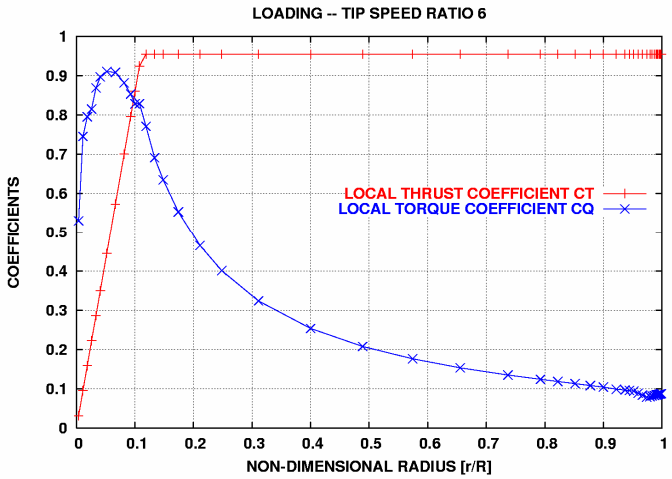

Figure 2-1 A constant thrust coefficient CT as function of radius and the corresponding tangential loading for an ideal rotor (airfoil C_D = 0) at a tip speed ratio of 6.

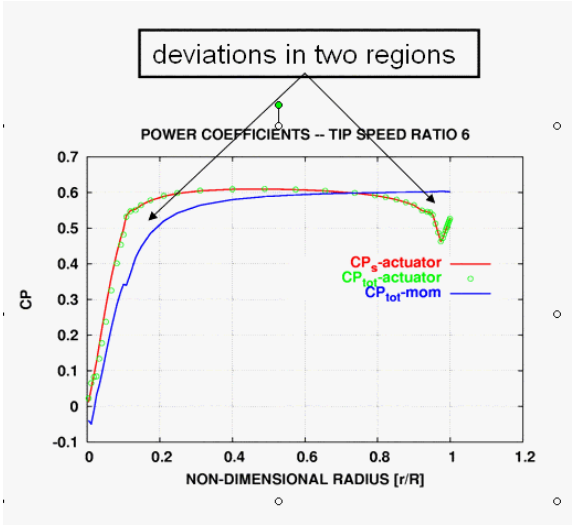

Figure 2-2 The variation of local CP for the loading shown in Figure 2-1 computed by an AD model and by the BEM model. For the AD model the local CP is derived in two ways; CP_s is the power coefficient based on shaft power and CP_{tot} is derived from an equation for the energy conversion in the flow – see [1] for details.

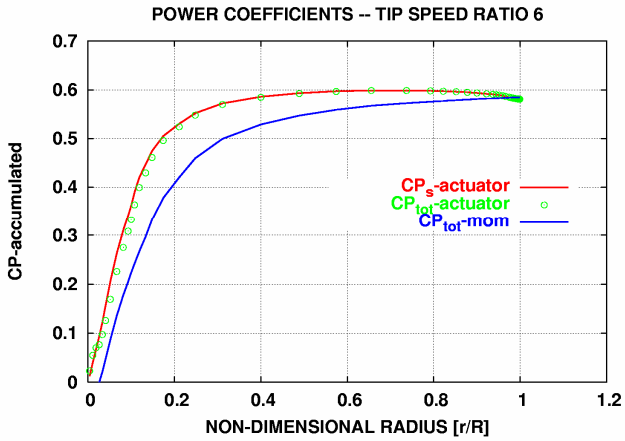

Figure 2-3 The accumulated CP curves derived from the local CP curves of Figure 2-2. This means that the curves show the average CP from the rotor center and to the actual radial position. The value of the curves at non-dimensional radius 1 thus shows the average CP for the whole rotor.

avoid induced velocities approaching infinity, Figure 2-1. For an ideal rotor (airfoil drag C_D equal to zero) the corresponding tangential loading *CQ* can be derived and depends, besides of *CT,* only on the actual tip speed ratio which is 6 in the present case. The details about how the AD simulations are performed and how the correlation is between *CT* and *CQ* can be found in [1].

The comparison of the local *CP* for this loadform, Figure 2-2 , shows that the BEM model underestimates *CP* on the inboard part of the rotor and overestimates *CP* on the outer part of the rotor. However, the average *CP* for the whole rotor is almost the same for the BEM and the AD model as shown with the accumulated *CP* curves in Figure 2-3, which at non-dimensional radius 1 show the average *CP* for the whole rotor. This means that the underestimation of *CP* on the inboard part of the rotor is almost cancelled by the over-prediction on the outer part of the rotor.

In the following, a correction model to be implemented in the BEM model for each of the deviations will be presented.

2.2 Correction model for the influence of the pressure variation from wake rotation

As mentioned above, the deviation on the inboard part of the rotor is due to the neglection of the pressure term from wake rotation in the BEM model, as discussed in

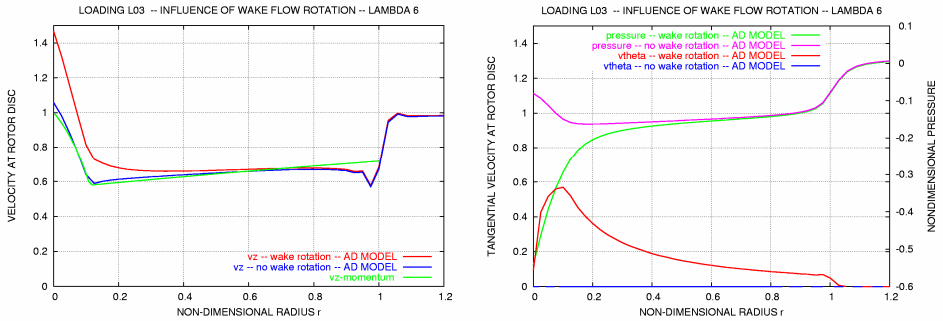

Figure 2-4 To the left is shown the computed axial velocity computed with the AD model with and without wake rotation included and compared with BEM results. To the right is shown the pressure variation at the rotor disc computed with and without wake rotation which corresponds to the tangential velocity also shown.

details in [1]. An illustration of the mechanism is shown in Figure 2-4. When the wake rotation is not included in the AD model (no tangential volume forces applied), the axial velocity at the rotor disc correlates well with the BEM result. On the contrary, increased velocity (less axial induction) is seen when wake rotation is included. To the right in Figure 2-4 is shown the reduction of the pressure towards the rotor center when wake rotation is included. This reduced pressure will accelerate the flow and even increase the velocity above free stream velocity, as seen in the left figure of Figure 2-4, although there is an axial loading on the rotor.

The mechanism behind the increased axial velocity due to wake rotation is thus simple, and the same is the proposed correction model to the BEM model. The correction model contains two steps:

- Compute the radial pressure variation at the rotor disc from the induced tangential velocity distribution.
- Derive the axial velocity component corresponding to this pressure variation and add it to the local velocity at the disc (free stream velocity minus induction).

The procedure was derived and shown in [1] but a brief description is repeated here so that a complete presentation of the corrections of the BEM model are available here.

The pressure term from the wake rotation is computed as:

$$p_{wake} = -\int_1^r \frac{v_t^2}{r} dr \qquad (2\text{-}1)$$

where v_t is the tangential velocity computed in the BEM code: $v_t = a' r\Omega$. The minus sign on the integral indicates a pressure deficit. It should be noted that all the variables are non-dimensionalized [1] and the integration is from the rotor tip (r=1) to r.

From the linearized equations for the actuator disc flow (Glauert [2] pp. 365) we have:

$$\frac{\partial vz}{\partial x} = -\frac{\partial p}{\partial x} + X \qquad (2\text{-}2)$$

where X is the axial volume force. Integrating this equation, the velocity correction term vz_{wake} should be equal to p_{wake}. However, comparisons with the numerical results from the AD model indicates that it is not the full pressure deficit that is converted to an increased velocity. The following relation gives the best correlation with numerical AD results:

A simple correction of the BEM model for the influence of the pressure term from wake rotation has been proposed

$$vz_{wake} = 0.7\, p_{wake} \qquad (2\text{-}3)$$

The factor 0.7 has been tested for a number of different loadings and the reason why the full conversion from pressure to velocity is not obtained is probably due to the second order terms disregarded in Equation (2-2). It should also be noted that the pressure term originating from the wake rotation shows a discontinuity across the rotor disc because the tangential velocity jumps from zero just in front of the rotor to its full value just behind it. The axial velocity term vz_{wake} is thus also discontinuous across the disc, but in the AD simulations the discontinuities can be seen as steep gradients in the axial direction, both for the pressure and for the velocity term related to the wake rotation. The discontinuities might also explain why the velocity term does not reach its full value.

The axial velocity vz_{cor1} corrected for the rotation of the wake is then:

$$vz_{cor1} = (1-a) + vz_{wake} \qquad (2\text{-}4)$$

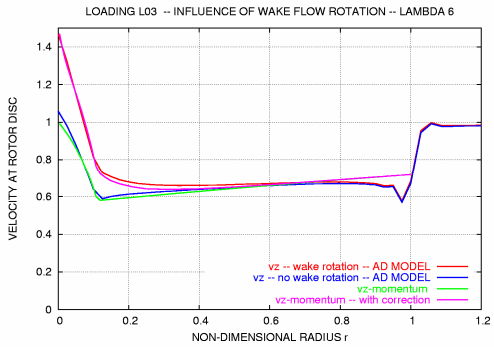

Figure 2-5 *The effect of the correction of the BEM model to include an additional velocity term from the wake pressure due to wake rotation. Correlation with the AD model is now excellent on the majority part of the blade, both for the velocities shown to the left and the accumulated power coefficient to the right. However, the decrease in velocity at the tip of the blade is not modeled with the BEM code.*

2.3 Correction model for the decreased inflow in the tip region due to wake expansion

The other characteristic deviation, when comparing the BEM model with AD results, is the reduced inflow at the tip region that is not modeled by the BEM model. This is illustrated in Figure 2-6 where the induction for a constant loading is shown. The BEM

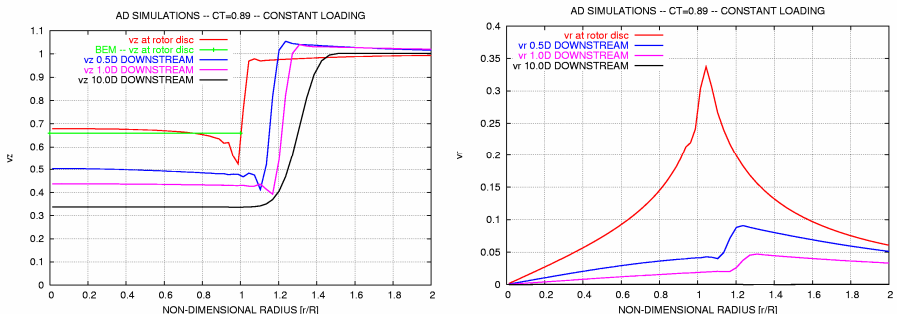

Figure 2-6 Illustration of the reduced inflow at the tip region and how the profiles become more constant for increasing downstream distance from the rotor disc. To the right is shown how the radial velocity profiles develop. The radial velocity is a good measure of rate of expansion.

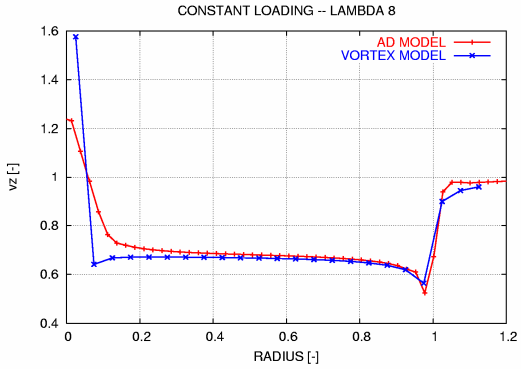

Figure 2-7 A comparison of the axial velocity profile at the rotor disc, computed with the AD model and a vortex model [3], respectively. Constant loading at a tip speed ratio of 8.

model gives a constant induction whereas the AD model shows a decreasing velocity (larger induction) at the tip region, but with the opposite tendency towards the rotor center. However, just 1 diameter (D) downstream, the velocity profile is almost constant and far downstream it has become completely constant. The corresponding radial velocity profiles shown to the right in Figure 2-6 are a good measure of the rate of expansion and show clearly the big difference in rate of expansion at the rotor disc to the conditions further downstream.

In Figure 2-7 the AD results are compared with the results from a free vortex model [3] developed by Mac Gaunaa at Risoe. There is a good correlation between the two models and in particular the reduced inflow at the tip region is predicted exactly in the same way.

The above results indicate that the reduced inflow at the tip region are due to the wake expansion or more specifically the rate of wake expansion. A simple vortex model for a constant loaded AD with a cylindrical wake gives a constant induction over the disc as shown by Øye [4]. However, for an expanding vortex sheet, the induction is no longer constant. This explains why the velocity distribution just 1D down stream is almost constant as shown above in Figure 2-6 because the wake from this point and further downstream is almost cylindrical.

In the proposed correction model to be included in the BEM model the reduced inflow in the tip region is therefore based on the assumption of a close relation between the radial velocity distribution *vr* at the disc and the reduced inflow *dvz*. These two parameters *dvz* and *vr* are shown in Figure 2-8. The corresponding radial velocity profiles are shown to the right in Figure 2-8.

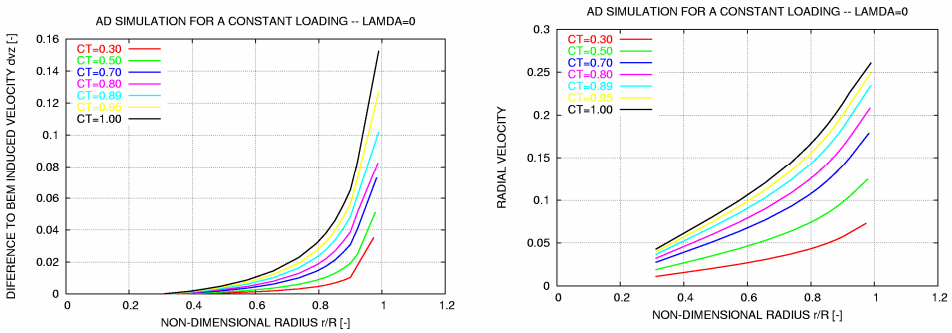

Figure 2-8 In the figure to the left the difference in axial velocity dvz comparing BEM and AD results for a constant loading. To the right is shown the radial velocity profiles from the AD simulations.

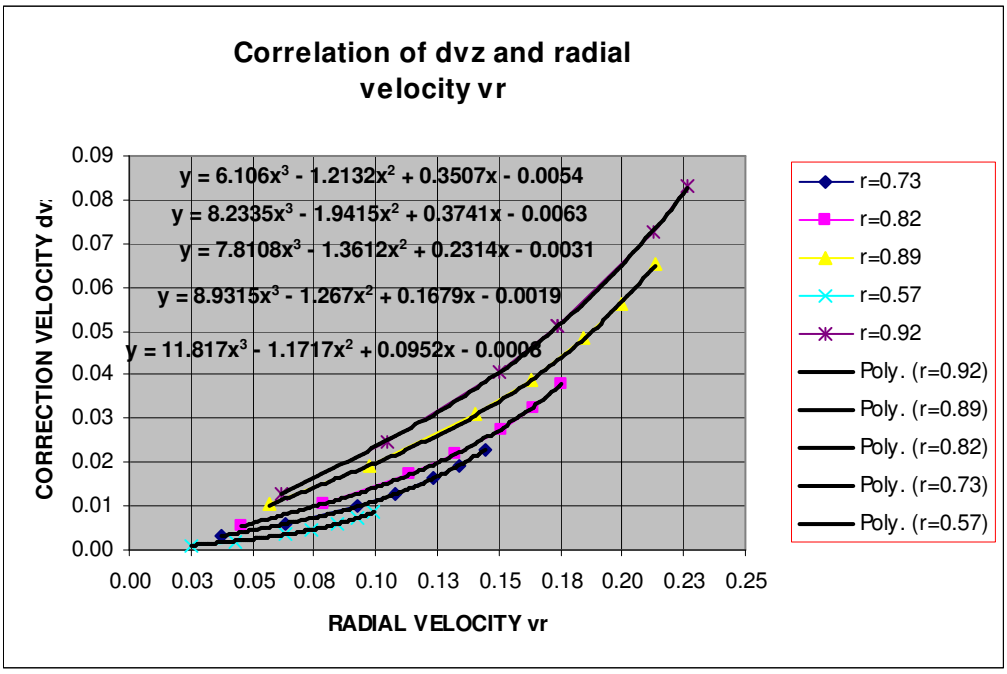

Figure 2-9 Correlation chart between radial velocity and axial correction velocity dvz.

The correlation between *vr* and *dvz* at different radial positions are shown in Figure 2-9 and approximated with third order polinomial trendlines. The variation of the factors in each of these polynomia is now derived as function of radius with the following result:

Coefficient *k3* on x^3: $k3 = -15.83r + 20.73$ *(2-5)*

Coefficient *k2* on x^2: $k2 = -0.52r - 0.90$ *(2-6)*

Coefficient *k1* on *x:* $k1 = 1.58r^2 - 1.63r + 0.51$ *(2-7)*

The small constant term in the polynomia is disregarded as we want to be sure that *dvz* is zero for *vr* equal to zero.

The variation of *dvz* is thus written as:

$$dvz(r) = k3\,vr(r)^3 + k2\,vr(r)^2 + k1\,vr(r) \qquad (2\text{-}8)$$

However, with the BEM method *vr* cannot be derived directly. Therefore, we make use of an analytical solution for the flow through a lightly loaded, 2D actuator strip as derived by Madsen [5].

$$vr = \frac{\Delta p}{4\pi}\ln\left(\frac{z^2 + (r+1)^2}{z^2 + (r-1)^2}\right) \qquad (2\text{-}9)$$

Here, Δp is the pressure drop across the actuator strip and *z, r* is axial and lateral direction.

For the present application it has been tested that the following version of the above equation gives a good correlation with AD model predictions of *vr*:

$$vr = \frac{1}{2.24}\frac{CT_{av}}{4\pi}\frac{0.04^2 + (r+1)^2}{0.04^2 + (r-1)^2} \qquad (2\text{-}10)$$

where CT_{av} is the local, average thrust coefficient derived as:

$$CT_{av} = \frac{\int_0^r CT\,2\pi r\,dr}{\pi r^2} \qquad (2\text{-}11)$$

Now, *CT* is derived as the thrust coefficient corresponding to the axial induction after the pressure correction in eq. (2-4). We derived this *CT* by the inverse of the *CT(a)* relation written as:

$$CT = 2.48a_{cor}^3 - 4.38a_{cor}^2 + 3.86a_{cor}$$

where a_{cor} is the induction corresponding to the corrected axial velocity vz_{cor1} given by eq. (2-4):

$$a_{cor} = (1 - vz_{cor1}) \qquad (2\text{-}12)$$

The final axial velocity vz_{cor2} after the correction for the reduced inflow at the tip is derived as:

$$vz_{cor2} = f_{massflow}(vz_{cor1} - dvz) \qquad (2\text{-}13)$$

The constant $f_{massflow}$ is the ratio of the mass flow in the uncorrected BEM and the mass flow after the two corrections terms are introduced:

$$f_{massflow} = \frac{\int_0^1 vz\, 2\pi r\, dr}{\int_0^1 (vz_{cor1} - dvz)\, 2\pi r\, dr} \qquad (2\text{-}14)$$

The mass flow correction was introduced because the general tendency in the comparison of the uncorrected BEM with AD results is that the integrated CP compares well for the two models.

2.4 Validation of the two corrections in the BEM model

The same case as shown in Figure 2-1 to Figure 2-3 is used again for validation of the BEM correction models, denoted BEMcor model

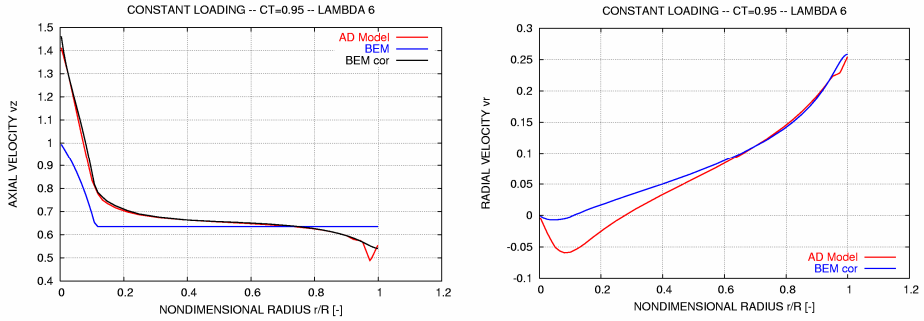

Figure 2-10 The axial velocity profiles to the left and radial velocity profiles to the right, computed by the AD model, the BEM model and the BEM model with the two correction sub models.

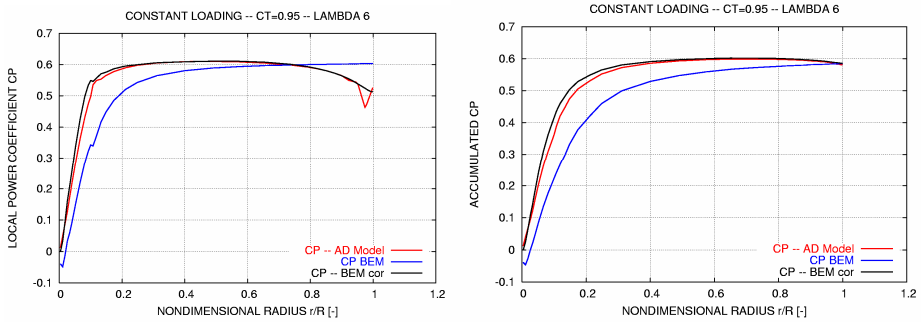

Figure 2-11 Local CP to the left and accumulated CP to the right, computed by the AD model, the BEM model and the BEM model with the two correction sub models.

There is an excellent correlation between the axial velocity profiles computed with the BEMcor model and the AD results, Figure 2-10. Also the radial profiles compare well although there are some deviations on the inboard part. However, here the radial velocity has no influence on the corrections. The same good correlation holds for the local *CP* in the left graph in Figure 2-11 and in the accumulated *CP* in the right graph.

The BEMcor model is next tested on a loading corresponding to constant induction on the major part of the rotor and at a tip speed ratio of 8, Figure 2-12 and Figure 2-13. As above the correlation between the BEMcor model results and the AD results are excellent. It can also be noticed that the local CP exceeds clearly the Betz limit on parts of the rotor whereas this is not predicted with the BEM model.

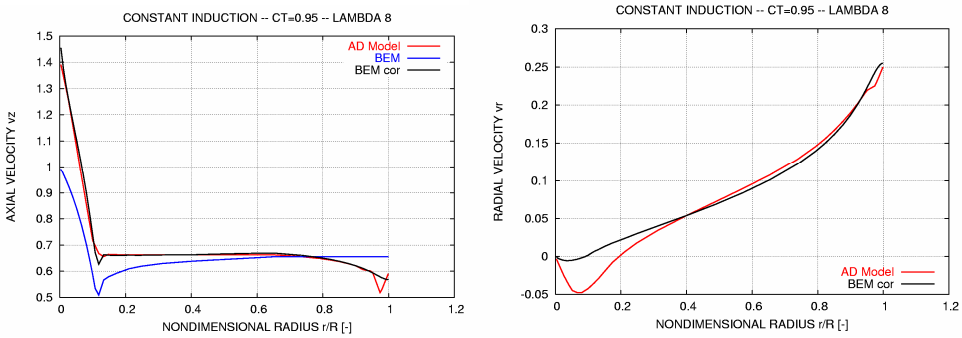

Figure 2-12 The axial velocity profiles to the left and radial velocity profiles to the right, computed by the AD model, the BEM model and the BEM model with the two correction sub models.

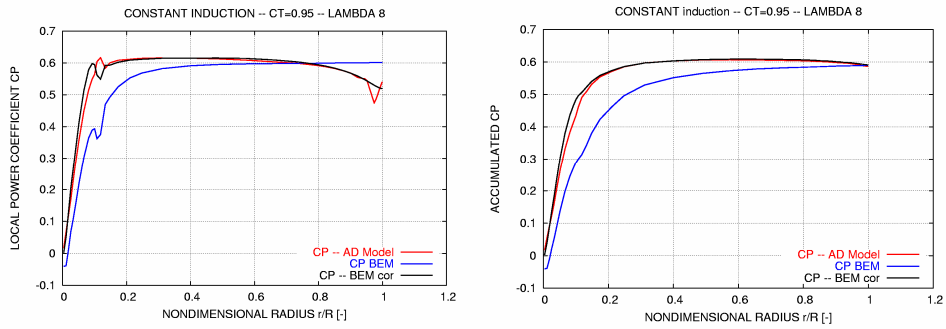

Figure 2-13 Local CP to the left and accumulated CP to the right, computed by the AD model, the BEM model and the BEM model with the two correction sub models.

2.5 References

[1] Madsen, H.A., Mikkelsen, R., Johansen, J., Bak, C., Øye, S., and Sørensen, "Inboard rotor/blade aerodynamics and its influence on blade design". In report Risø-R-1559(EN) "Research in Aeroelasticity EFP-2005", Risø National laboratory, May 2006 edited by Christian Bak.

[2] Glauert, H. "Airplane Propellers". Volume IV in Aerodynamic Theory edited by William Fredrick Durand. The Dover edition 1963.

[3] Gaunaa, M. and Johansen, J. "Determination of Maximum Aerodynamic Efficiency of Wind Turbine Rotors with Winglets". To be presented at the conference TWIND2007 to be held at DTU in Denmark, August 2007.

[4] Øye, S. "A simple vortex model". In proceedings of the third IEA Symposium on the Aerodynamics of Wind Turbines, ETSU, Harwell, 1990, pp. 4.1-5.15.

[5] Madsen, H.A. “A CFD Analysis of the Actuator Disc Flow compared with Momentum Theory Results”. In proceedings of IEA Joint Action of 10th Symposium on Aerodynamics of Wind Turbines, Edinburg, December 16-17, 1996 edited by B.M. Pedersen, pp. 109-124.

3 The Optimum Rotor: Circulation Distributions and Operating Regimes

J. N. Sørensen and V. L. Okulov

We here present new results on the classical work of the optimum rotor. The emphasis is put on vortex theory for which we have developed a new analytical method to determine the loading on an optimum wind turbine rotor. The first part of the work is a repetition of results using momentum theory. This is included in order to validate and compare the new model at simplified situations, such as a rotor operating without swirl and/or a rotor with infinitely many blades.

3.1 The Optimum Rotor

Various classical theories for optimum rotors are considered

In the following we consider various classical theories for the optimum rotor. First we show the Betz limit using axial momentum theory. Next we consider a rotor with an infinite number of blades using general momentum theory. Finally, we analyse a realistic rotor with a finite number of blades using a new solution of the Goldstein circulation function.

Optimum Rotor: Rankine-Froude Theory

First, a simple axial momentum theory by Rankine and Froude is considered

We first consider the simple axial momentum theory as it originated by Rankine [1], W. Froude [2] and R.E. Froude [3]. Here we consider axial flow past an actuator disk representing the axial load on a rotor. Denoting by V_0 the undisturbed wind speed and by v_{z_0} the velocity in the rotor plane, the axial interference factor is defined as

$$a = 1 - \frac{v_{z_0}}{V_0}, \tag{3.1}$$

From one-dimensional axial momentum theory we obtain the following expression for the axial load (thrust) and power extraction

$$T = 2\rho A v_{z_0}(V_0 - v_{z_0}) = 2\rho A V_0^2 a(1-a), \tag{3.2}$$

$$P = u_{z_0} T = 2\rho A V_0^3 a(1-a)^2, \tag{3.3}$$

where ρ is the density of air, A denotes the rotor area and $u_{z_0} = V_0 - v_{z_0}$ is the axial velocity induced by wake in the rotor plane. Introducing dimensionless power and thrust coefficients, C_P and C_T, defined as, respectively,

$$C_T = T/(\tfrac{1}{2}\rho A V_0^2) = 4a(1-a), \tag{3.4}$$

$$C_P = P/(\tfrac{1}{2}\rho A V_0^3) = 4a(1-a)^2, \tag{3.5}$$

the maximum power that can be extracted from a stream of air contained in an area equivalent to that swept out by the rotor corresponds to the maximum value of the power coefficient. We get that

An important result is that the maximum power efficiency is $C_{P,max}=16/27$

$$C_{P\max} = \frac{16}{27} = 0.593 \quad \text{for} \quad a = \frac{1}{3}. \tag{3.6}$$

This result is usually referred to as the Betz limit and states the upper maximum for power extraction. However, it does not include the losses due to rotation of the wake, and therefore it represents a conservative upper maximum.

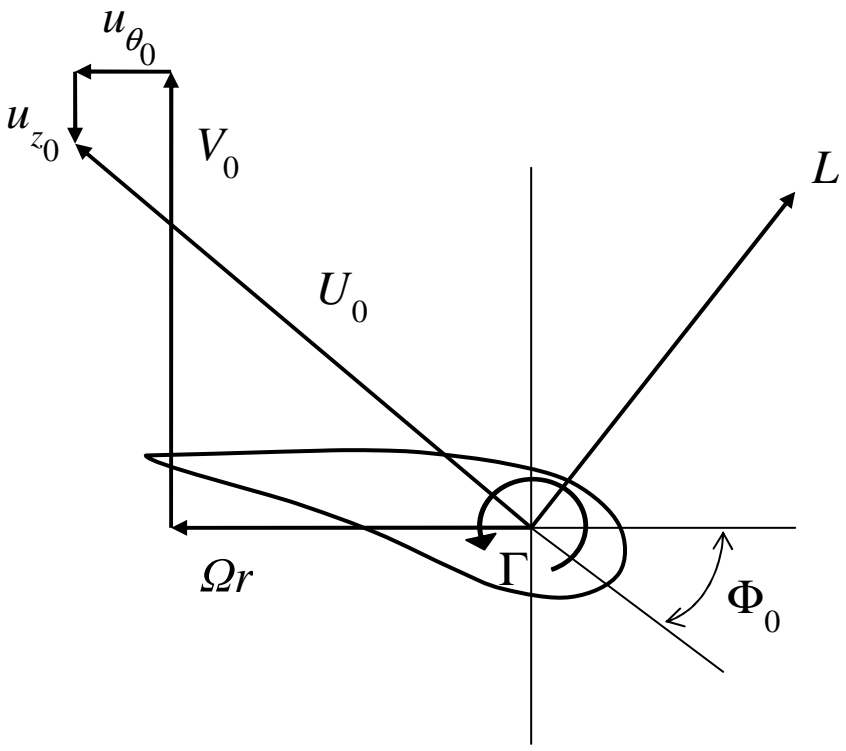

Figure 3-1 Velocity triangle in the rotor plane of a wind turbine

Optimum Rotor: General Momentum Theory

Secondly, a general momentum theory by Glauert is considered

Utilizing general momentum theory Glauert [4] developed a simple model for the optimum rotor that included rotational velocities. In this approach Glauert treated the rotor as a rotating actuator disk, corresponding to a rotor with an infinite number of blades. Denoting by Ω the angular velocity of the rotor blade and by u_{θ_0} the azimuthal velocity in the rotor plane, we define the azimuthal interference factor as

$$a' = \frac{u_{\theta_0}}{\Omega r}. \tag{3.7}$$

In Figure 3-1 we show of the velocity vectors for a blade element at radial position r. The local relative velocity, U_0, is perpendicular to the induced velocity $\vec{u} = \left(u_{z_0}, u_{\theta_0}\right)$ and the lift $\vec{L}$ (ignoring drag). Employing Euler's turbine equation, we get

$$P = \rho \Omega \int r u_\theta u_{z_0} dA, \tag{3.8}$$

where $u_\theta = u_\theta(r)$ is the azimuthal velocity in the wake. For a rotor with an infinitely number of blades it can be shown that the induced velocity in the rotor plane approximately is half of the one in the wake ($u_\theta = 2u_{\theta_0}$). Considering the flow through annular elements of area $dA = 2\pi r dr$, we get

$$P = 4\pi\rho\Omega^2 V_0 \int (1-a)a' r^3 dr. \tag{3.9}$$

Introducing the tip speed ratio, $\lambda = \Omega R / V_0$, and dimensionless radius, $x = r/R$, where R is the radius of the rotor, the power coefficient reads

$$C_P = \frac{8}{\lambda^2} \int_{x=0}^{1} (1-a)a' x^3 dx. \tag{3.10}$$

Since the integral involves two dependent variables, we need to derive yet a relation between a and a' in order to determine the conditions under which the integral attains a maximum. This is accomplished by inspection of the velocity triangle in Figure 3-1. Since the total induced velocity is normal to the relative velocity, we get

$$\tan\Phi = \frac{(1-a)V_0}{(1+a')r\Omega} = \frac{a' r\Omega}{aV_0}, \tag{3.11}$$

resulting in the following relation

$$\lambda^2 x^2 a'(1+a') - a(1-a) = 0. \tag{3.12}$$

Now the task is to optimize equation (3.10) subject to the constraint (3.12). Using variational calculus (see Glauert [4] or Wilson and Lissamann [5]), we get

$$a' = \frac{1-3a}{4a-1}, \tag{3.13}$$

Such that

$$a' x^2 \lambda^2 = (1-a)(4a-1). \tag{3.14}$$

From equations (3.13) and (3.14) it is readily seen that the operating range for an optimum rotor is $1/4 \le a \le 1/3$. The variation in $a, a', a'x^2\lambda^2$ and x are given in table 1 (reproduced from [5]).

Table 3-1 Flow conditions for the optimum actuator disk.

a	a'	$a'x^2\lambda^2$	λx
0.25	∞	0	0
0.27	2.375	0.0584	0.157
0.29	0.812	0.1136	0.374
0.31	0.292	0.1656	0.753
0.33	0.031	0.2144	2.630
1/3	0	0.2222	∞

Table 3-2 Power coefficient as function of tip speed ratio for the optimum actuator disk.

λ	$C_{P\max}$
0.5	0.288
1.0	0.416
1.5	0.480
2.0	0.512
2.5	0.532
5.0	0.570
7.5	0.582
10.0	0.593

The general momentum theory shows a varying maximum efficiency depending on the tip speed ratio

Combining equations (3.12) and (3.13) and integrating equation (3.10), the power coefficient may be obtained as a function of tip speed ratio. The result is shown in table 2, from which it is seen that the power coefficient approaches 0.593 for large tip speed ratios.

It shall be mentioned that these results are valid only for a rotor with an infinite number of blades and the analysis is based on the assumption that the rotor can be optimized by considering each blade element independently of the remaining blade elements.

Optimum Rotor: Vortex Theory

Finally, the vortex theory is considered to take into account e.g. tip loss

The flow over a real rotor with a finite number of blades is very different from the properties of the flow models used in the previous section to describe the optimum rotor. Indeed, important phenomena such as tip losses and azimuthal dependencies of the induced velocities are neglected in the momentum theory of the optimum rotor. An alternative model is the vortex theory in which each of the rotor blades is represented by a bound vortex line. Using this technique, the bound vorticity serves to produce the local lift on the blades while the trailing vorticies induce the velocity field in the rotor plane and in the wake. The induced velocity field is determined using the induction law of Biot-Savart. The fundamental expression for the forces acting on a propeller is most conveniently expressed by the Kutta–Joukowsky theorem, which in vector form reads

$$d\vec{L} = \rho\vec{U}_0 \times \vec{\Gamma} dr \,, \tag{3.15}$$

where dL is the lift force on a blade element of radial dimension dr, U_0 is the resultant relative velocity and Γ is the bound circulation. Let u_{θ_0} and u_{z_0}, be the circumferential and axial components of the velocity, induced by the free vortex wake behind the rotor, at a blade element in the rotor plane. Then, in accordance with Figure 3-1, we can write the local torque, dQ, and the local thrust dT of the rotor as follows

$$dQ = \rho\Gamma\left(V_0 - u_{z_0}\right) r dr \,, \tag{3.16}$$

$$dT = \rho\Gamma\left(\Omega r + u_{\theta_0}\right) d\mathbf{r} \,. \tag{3.17}$$

Integrating these quantities along each blade and summing up, we get the following expressions for power and thrust

$$P = \rho B\Omega \int_0^{R_0} \Gamma\left(V_0 - u_{z_0}\right) r dr \,, \tag{3.18}$$

$$T = \rho B \int_0^{R_0} \Gamma\left(\Omega r + u_{\theta_0}\right) dr \,, \tag{3.19}$$

where B is the number of blades. In order to derive the relations for an optimum rotor we impose a small but arbitrary continuous circulation perturbation $\varepsilon\Delta\Gamma(r)$ on an existing distribution of circulation. Thus, the additional torque and thrust read

$$\delta Q = \rho\left(V_0 - u_{z_0}\left(r\right)\right)\varepsilon\Delta\Gamma\left(r\right) r dr \,, \tag{3.20}$$

$$\delta T = \rho\left(\Omega r + u_{\theta_0}\left(r\right)\right)\varepsilon\Delta\Gamma\left(r\right) dr \,, \tag{3.21}$$

where ε is a small constant. We now seek the conditions under which a change in circulation from the initial distribution, at constant thrust does not change the power yield. Employing variational calculus the change in torque and thrust read

$$\delta Q = \varepsilon\rho \int_0^R \left(V_0 - u_{z_0}\right)\Delta\Gamma(r) r dr \,, \tag{3.22}$$

$$\delta T = \varepsilon\rho \int_0^R \left(\Omega r + u_{\theta_0}\right)\Delta\Gamma(r) dr \,. \tag{3.23}$$

Maintaining the torque unchanged, i.e. keeping $\delta T = 0$, we seek the conditions for which a maximum is achieved for the total power. This can only be obtained when the perturbed power yield is zero, i.e. for $\delta P = \Omega\delta Q = 0$. Instead of going through a formal derivation, Betz [6] showed that this condition is satisfied if

$$r\tan\Phi_0 = r\left[V_0 - u_{z_0}\left(r\right)\right] \Big/ \left[\Omega r + u_{\theta_0}\left(r\right)\right] = \Lambda \,, \tag{3.24}$$

where Λ is a constant that does not depend on the radial distance. By inspection it is readily seen that $\delta T = \delta P = 0$ while $\delta Q / \delta T = \Lambda$, indicating that an extremum has been achieved. From equation (3.24) it is seen that maximum efficiency is obtained when the pitch of the trailing vortices is constant and each trailing vortex sheet translates backward as an undeformed regular helicoidal surface.

Using potential flow theory and infinite series of Bessel functions Goldstein [7] derived the circulation distribution corresponding to an undeformed helical screw surface. In the following we employ Goldstein's circulation function $G(r)$ as it was later used by Theodorsen [8] and Wald [9]. This function expresses the optimum circulation corresponding to a helicoidal vortex sheet translated with constant speed, and is in dimensionless form defined as

$$G(r) = \Gamma(r) / hw = B\Gamma\Omega / 2\pi w(V_0 + w), \tag{3.25}$$

where $h = 2\pi r \tan\Phi / B = 2\pi(V_0 + w) / B\Omega$ is the axial distance between adjacent turns of the helicoidal sheets and w the backward velocity of the vortex system with respect to the surrounding fluid. It should be pointed out that Goldstein, assuming light loading, wrote V_0 where Theodorsen put $V_0 + w$. The distribution of $G(r)$ will be derived in the following, but first we derive an expression for translated axial speed w. In Figure 3-3 we sketch the velocity triangle in a planar cut of the translating helicoidal screw surface.

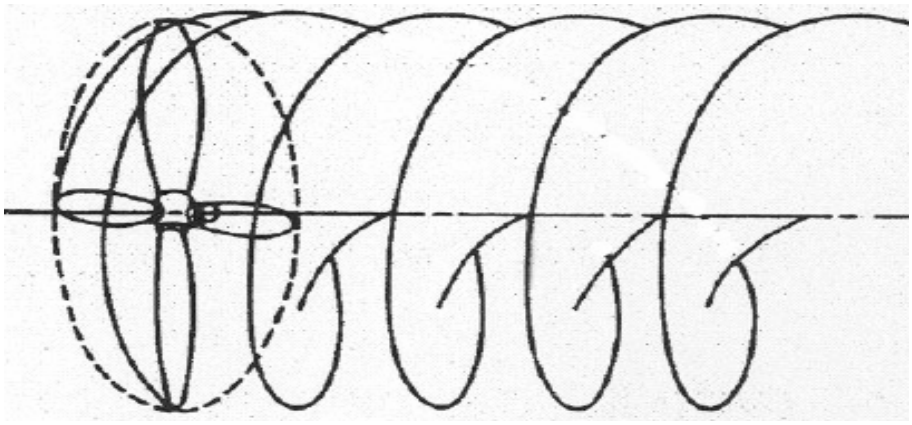

Figure 3-2 Sketch of undeformed helical screw surface corresponding to the wake of an optimum rotor ([7]).

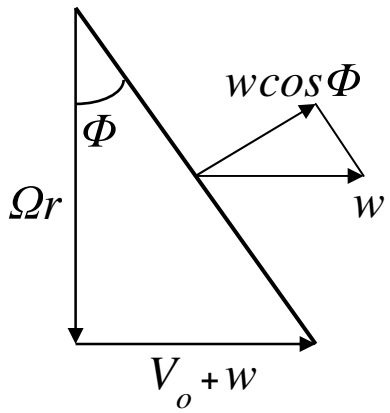

Figure 3-3 Sketch of the velocity triangle in a planar cut of the helicoidal screw surface.

Since it is translated with constant axial speed w, the induced velocity comprises only the component $w\cos\Phi$ that is 'pushed' normal to the screw surface. The induced velocities are therefore given as

$$u_\theta = -w\cos\Phi\sin\Phi \quad \text{and} \quad u_z = w\cos^2\Phi\,, \tag{3.26}$$

where Φ is the angle between the vortex sheet and the rotor plane (see Figure 3-3). Specification of the trigonometric functions in (3.26) allow us to find a correlation between u_z, u_θ and *w,* given by Goldstein [7]

$$u_\theta = -wxl\Big/\left(l^2 + x^2\right) \text{ and } u_z = wx^2\Big/\left(l^2 + x^2\right), \tag{3.27}$$

where $x = r/R_0$ and $2\pi l/R_0$ are the non-dimensional radius and the distance between turns of the fixed helicoidal sheet, respectively. In fact, equations (3.26) and (3.27) fix the ratio $u_\theta/u_z = -l/x = -\tan\Phi$ which, for a given radius, is constant everywhere on the helicoidal sheets, although the induced velocities may change along the wake.

Inserting the Goldstein function (3.25) into equations (3.18) and (3.19), and introducing dimensionless variables equations (3.4) and (3.5), we get

$$C_P = 2\sigma\overline{w}\left(1+\overline{w}\right)\left(I_1 - \overline{w}I_3\right), \text{ and } C_T = 2\sigma\left(\overline{w}\left(1+\overline{w}\right)I_1 - \overline{w}^2 I_2\right) \tag{3.28}$$

where $\overline{w} = \dfrac{w}{V_0}$; $\sigma = A_{wake}/A$ and $I_1 = 2\int_0^1 G(x)\,x\,dx$; $I_2 = 2\int_0^1 G(x)\dfrac{lx^2\,dx}{x^2+l^2}$,

$I_3 = 2\int_0^1 G(x)\dfrac{x^3\,dx}{x^2+l^2}$.

Differentiating C_P with respect to $\overline{w}$ yields the maximum value $C_{P,\max}$, resulting in

$$\overline{w} = \frac{1}{3I_3}\left(\sqrt{I_2^2 + I_1 I_3} - I_1 - I_3\right). \tag{3.29}$$

It now remains to compute the distribution of circulation or the Goldstein circulation function $G(x)$ for the vortex sheet which corresponds to the helicoidal configuration and to relate this to the distribution at the propeller itself. Goldstein [7] was the first to derive a solution to the general potential flow problem posed by Betz [6]. He considered two-bladed and four-bladed propellers and expressed the function $G(x)$ via a trigonometrical series of Kaptain type. However, such are the difficulties of computation, even after the way to a solution was found, that Theodorsen resorted to the use of a rheoelectrical analog to evaluate the circulation function, but unfortunately without big success [8]. Accurate tabulated values of a function related to the Goldstein function and covering a wide (but finite) range of parameters became available with an extensive mathematical and computational effort by Tibery & Wrench [10]. Expressions for the torque and thrust of a propeller operating at maximum efficiency are given by (3.28) and (3.29). Thus, to determine power and thrust as function of tip speed ratio, and the corresponding circulation, we need to derive an expression for the Goldstein circulation

function G. For this purpose we employ Okulov's representation of the velocity field induced by a single helical vortex filament with strength γ, radius r_0 and pitch $2\pi l$ (see Okulov [11]). In cylindrical coordinates (r,θ,z) the corresponding velocity components read

$$u_r \cong -\frac{\gamma}{2\pi r}\frac{\sqrt[4]{\left(l^2+r^2\right)\left(l^2+r_0^2\right)}}{l}\mathrm{Im}\left[\frac{e^{i\chi}}{e^{\mp\xi}-e^{i\chi}}\pm\frac{l}{24}\left(\frac{2l^2+9r_0^2}{\left(l^2+r_0^2\right)^{3/2}}-\frac{2l^2+9r^2}{\left(l^2+r^2\right)^{3/2}}\right)\ln\left(1-e^{\pm\xi+i\chi}\right)\right],$$

$$u_z \cong \frac{\gamma}{2\pi l}\begin{Bmatrix}1\\0\end{Bmatrix}+\frac{\gamma}{2\pi l}\frac{\sqrt[4]{l^2+r_0^2}}{\sqrt[4]{l^2+r^2}}\mathrm{Re}\left[\frac{\pm e^{i\chi}}{e^{\mp\xi}-e^{i\chi}}+\frac{l}{24}\left(\frac{3r^2-2l^2}{\left(l^2+r^2\right)^{3/2}}+\frac{9r_0^2+2l^2}{\left(l^2+r_0^2\right)^{3/2}}\right)\ln\left(1-e^{\xi+i\chi}\right)\right],$$

$$u_\theta=\left(u_0-u_z\right)l/r\text{, and }u_0=\gamma/2\pi l\,. \tag{3.30}$$

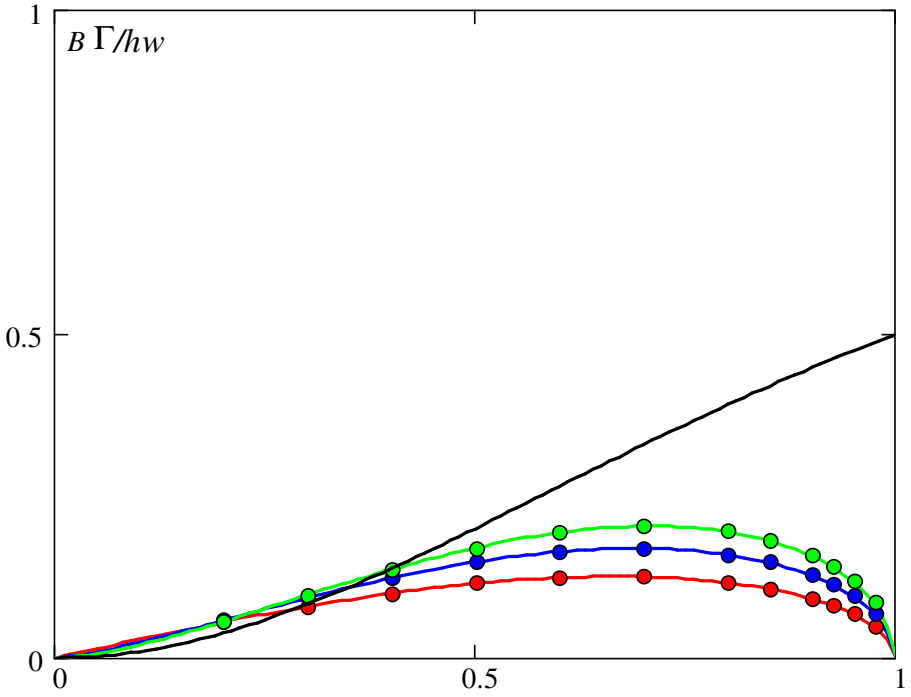

Figure 3-4 Goldstein circulation function for h = 1 and B = 2 (red); B = 3 (blue); B= 4 (green); Glauert function (black line); Points: Tibery & Wrench, Lines – : present.

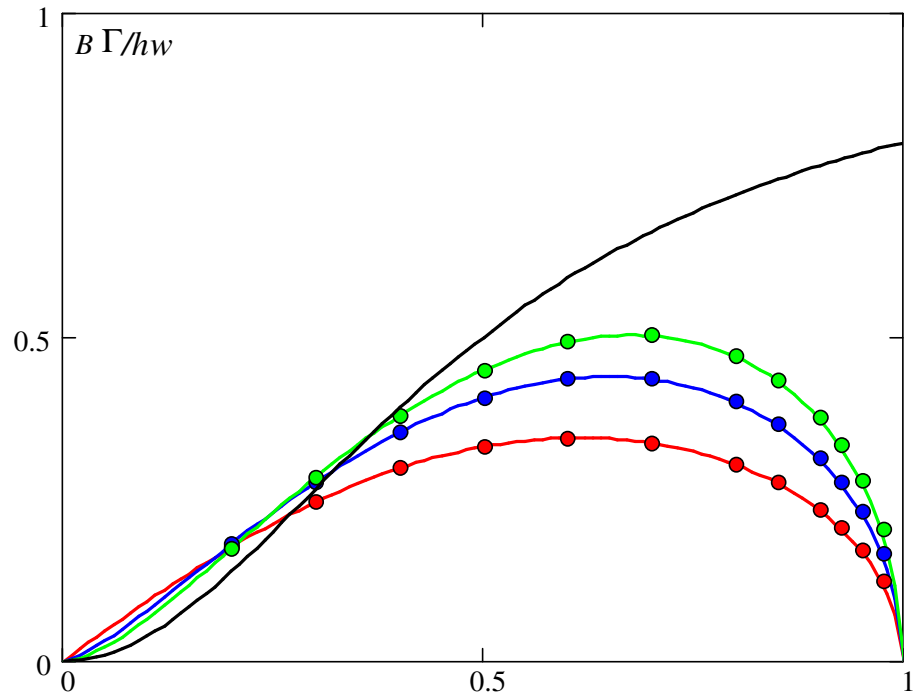

Figure 3-5 Goldstein circulation function for h = 1/2. Captions: see Figure 3-4.

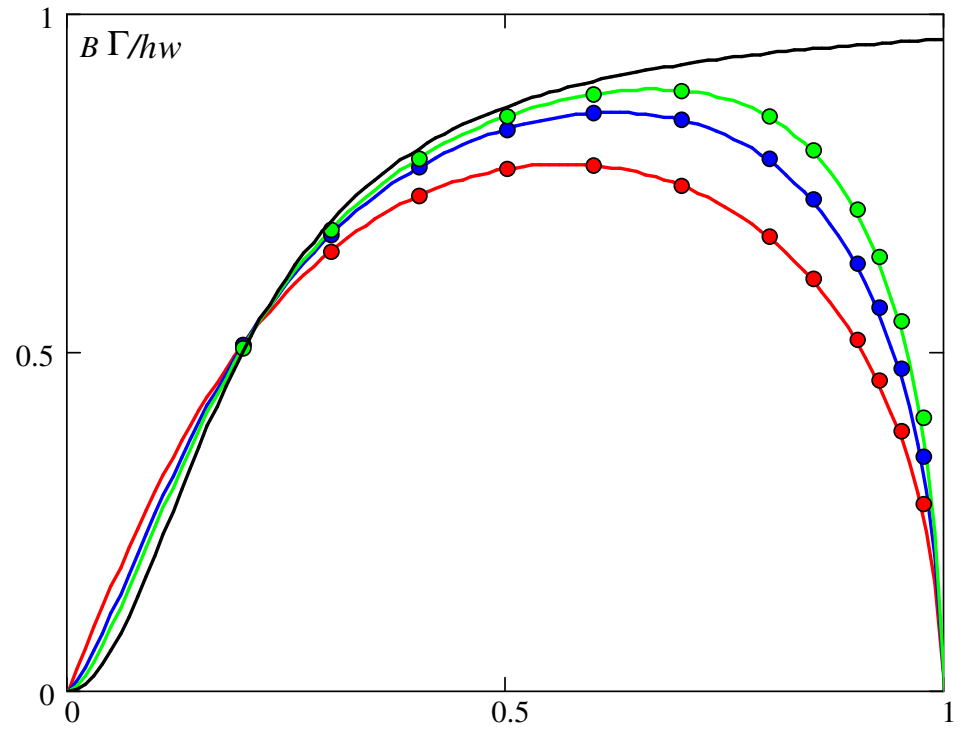

Figure 3-6 Goldstein circulation function for h = 1/5. Captions: see Figure 3-4.

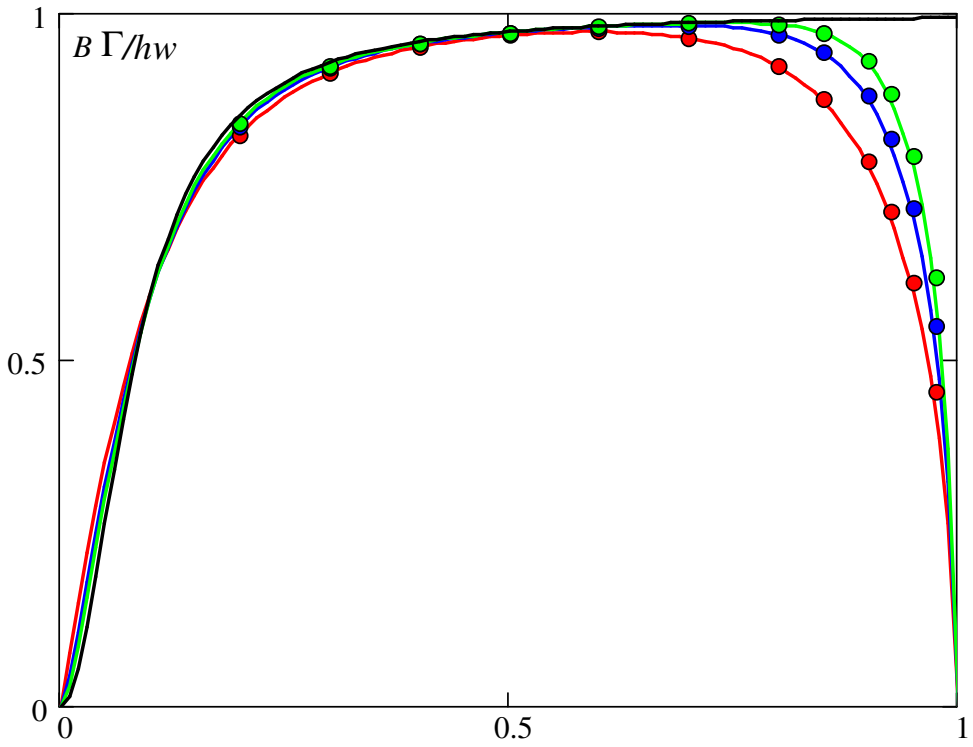

Figure 3-7 Goldstein circulation function for h = 1/12. Captions: see Figure 3-4.

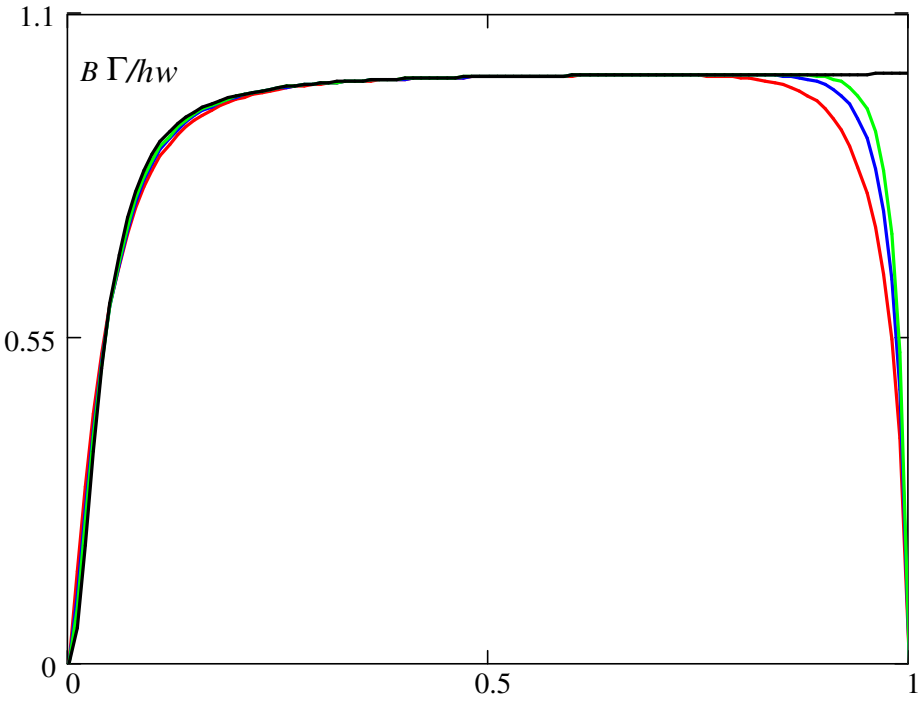

Figure 3-8 Goldstein circulation function for h = 1/25. Captions: see Figure 3-4.

The excellent correlations show that the problem can be successfully solved by using (3.30) and we now have the tools to evaluate the optimum rotor at all operating

conditions (see, for example, Figure 3-8), and not only for the parameter range computed by Tibery & Wrench. Thus, at any given value of the wake pitch, we can find the Goldstein circulation function $G(x)$ and calculate the integrals introduced in (3.28) and (3.29). Finally, to determine the optimum, it is needed to take into account the expansion of the wake. This we include in the expression for C_P by the expansion ratio σ. If we introduce the average value of the velocity deficit in the wake as $\langle u_z \rangle = 2\langle u_{z_0} \rangle = 2\langle a \rangle V_0$ the relationship between A_{wake} and A in rotor plane can be estimated from the conservation of mass as

$$\sigma = \left(1-\langle u_z \rangle\right)\Big/\left(1-\langle u_{z_0} \rangle\right) = \left(1-2\langle a \rangle\right)\Big/\left(1-\langle a \rangle\right). \tag{3.31}$$

The velocity interference factor $\langle a \rangle$ in (3.31) can be found as the total contribution from the induction of all the helix filaments in the wake (see, e.g. [11])

$$\langle a \rangle = \frac{\langle \Gamma \rangle}{hV_0} = \bar{w}\langle G \rangle \tag{3.32}$$

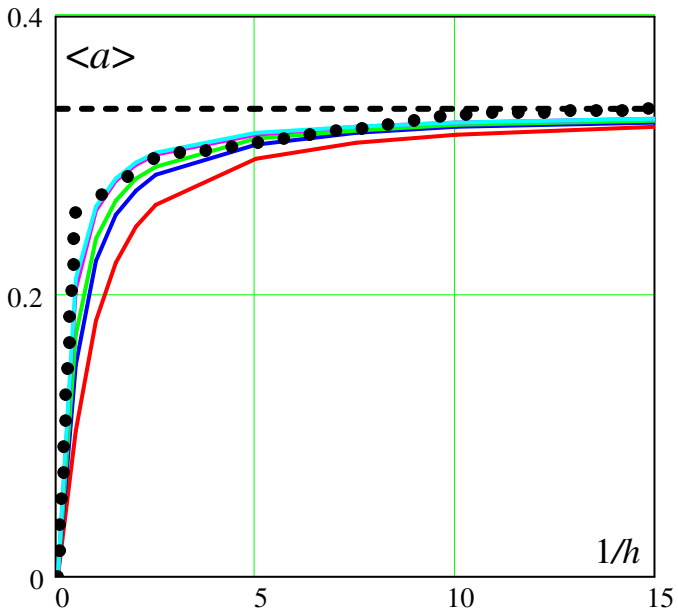

Figure 3-9 Dependence of the velocity interference factor $\langle a \rangle$ as functions of $1/h$ for different numbers of blades: B = 1(red); 2(blue); 3 (green); 10(pink); and 20(cyan); dashed black line shows the Betz value $a = 1/3$ and points indicates the data of Table 2.

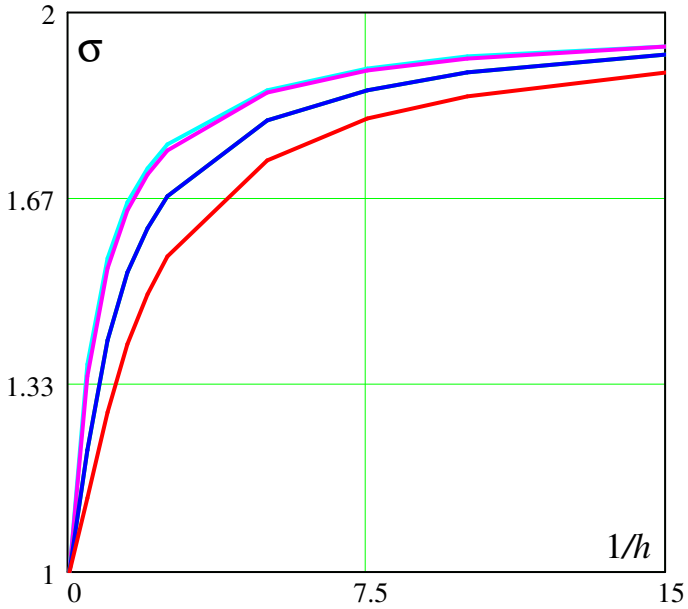

Figure 3-10 Dependence of the expansion ratio σ as function of $1/h$ for different numbers of blades.Lines description see on Figure 3-9.

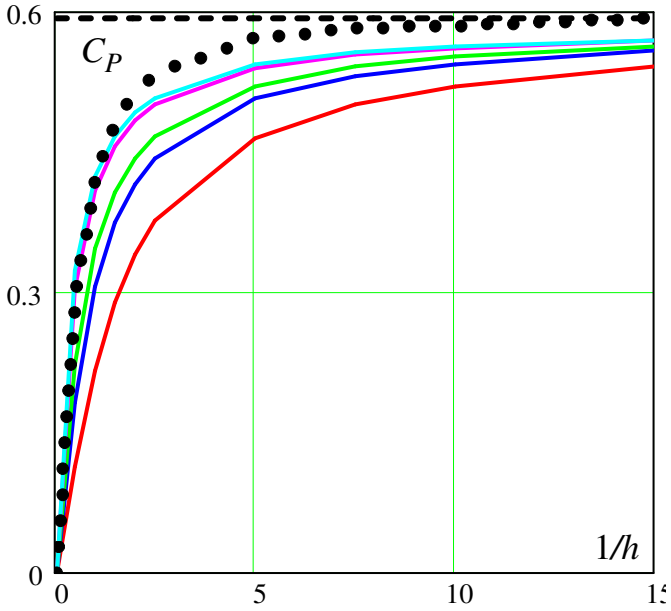

Figure 3-11 Comparison of the optimum power coefficient, Cp, between the Betz limit (dashed lines), momentum theory (points) and present theory as functions of $1/h$ for different numbers of blades: Lines description see on Figure 3-9.

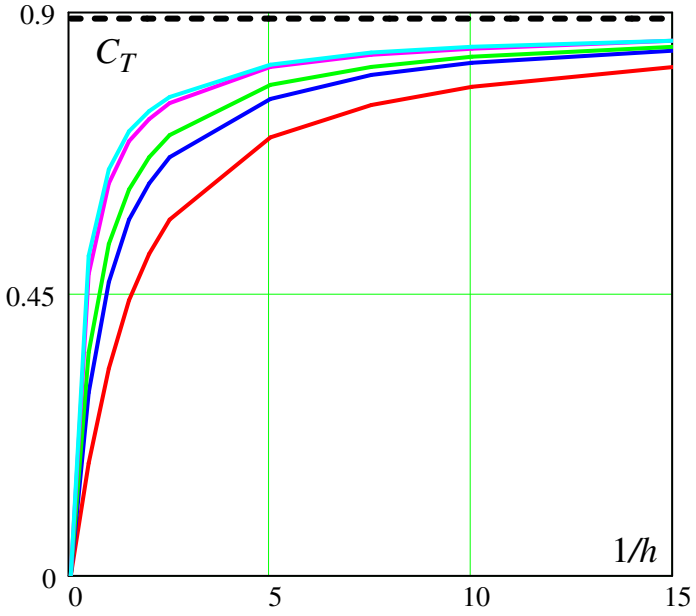

Figure 3-12 Comparison of the thrust coefficient, C_T, between the Betz limit (dashed lines), momentum theory (points) and present theory as functions of $1/h$ for different numbers of blades: Lines description see on Figure 3-9.

In Figure 3-9 and Figure 3-10 the dependence of the deficit velocity interference factor and ratio of the area between the wake and the rotor plane are shown graphically as functions of $1/h$ for different numbers of blades.

Figure 3-11 and Figure 3-12 shows the power and thrust coefficients for different numbers of blades, given by (3.29), using of (3.31) and (3.32), for different operating regimes of a wind turbine with ideal load distribution.

3.2 Conclusion

A new analytical method to determine the loading on an optimum wind turbine rotor has been developed. The method enables to determine the optimum circulation distribution from Goldstein's function at all operating conditions. The proposed procedure for calculation of Goldstein's function and corresponding torque and thrust coefficients completes the traditional theory as it was formulated by Theodorsen [8]. The optimum characteristics are given as a function of the pitch of the wake. In a continuation of the work this will be related to the actual tip speed ratio of the rotor and to practical guide lines for how to design an optimum rotor.

A new analytical method to determine optimal loading was developed

3.3 References

[1] Rankine, W.J. (1865);Transactions, Institute of Naval Architects, vol. 6, p. 13.

[2] Froude, W. (1878); Transactions, Institute of Naval Architects, vol. 19, p. 47.

[3] Froude, R.E. (1889); Transactions, Institute of Naval Architects, vol. 30, p. 390.

[4] Glauert, H. (1935); 'Aerodynamic Theory' (W.F. Durand, Editor-in-chief), vol. 6, Division L, p. 324, Julius Springer, Berlin.

[5] Wilson, R.E. and Lissaman, P.B.S. (1974); 'Applied Aerodynamics of Wind Power Machines', Oregon State University.
[6] Betz, A. (1919); 'Schraubenpropeller mit Geringstem Energieverlust', Dissertation, Gottingen.
[7] Goldstein, S. (1929); *Proc R Soc London A*; Vol. 123, 440–465.
[8] Theodorsen, T. (1948); Theory of propellers; New York: McGraw-Hill Book Company.
[9] Wald (2006); *Progress in Aerospace Sciences*; Vol. 42, 85–128
[10] Tibery and Wrench (1964); Report 1534, Applied Mathematics Laboratory, Washington, DC.
[11] Okulov, V.L. (2004); *J. Fluid Mech.*; Vol. 521, 319 - 342.

4 Key parameters in aerodynamic rotor design

Christian Bak

This chapter describes an analysis of the influence of key parameters in aerodynamic wind turbine rotor design on power performance and energy production. The key parameters investigated are the tip-speed-ratio, the Reynolds number, the assumption of clean airfoils versus contaminated airfoils and large versus small blade root chords. The investigation shows that an optimal tip-speed-ratio exists, but that this value depends on the key parameters.

The influence of key parameters on power performance is investigated

4.1 Nomenclature

a	Axial velocity induction [-], $a = 1/(\frac{4\sin^2\phi F}{\sigma c_y}+1)$
a'	Tangential velocity induction [-], $a' = 1/(\frac{4\sin\phi\cos\phi F}{\sigma c_x}-1)$
A	Rotor area [m^2], $dA = 2\pi r dr$
B	Number of blades [-]
c	Chord length [m]
c_d	Drag coefficient [-]
c_l	Lift coefficient [-]
$c_{l,design}$	Design lift coefficient (c_l at maximum lift-drag ratio) [-]
c_l/c_d	Lift-drag ratio (measure of the airfoil efficiency) [-]
c_x	Driving force coefficient [-], $c_x = c_l \sin\phi - c_d \cos\phi$
c_y	Axial force coefficient [-], $c_y = c_l \cos\phi + c_d \sin\phi$
C_P	Power coefficient [-]
D	Rotor diameter [m]
F	Tip loss correction [-]
F_{drive}	Driving force [N]
r	Actual radius [m]
R	Rotor radius [m]
V_0	Wind speed [m/s]
W	Relative velocity [m/s], $W^2 = (V_0(1-a))^2 + (\omega r(1+a'))^2$
x	Local speed ratio [-], $x = \frac{\omega r}{V_0}$
X	Tip speed ratio [-], $X = \frac{\omega R}{V_0}$
X_{design}	Tip speed ratio at which C_P is maximum [-]
ϕ	Local inflow angle to rotor plane [°], $\phi = \arctan(\frac{1-a}{x(1+a')})$
ρ	Air density [kg/m^3]
σ	Rotor solidity [-], $\sigma = \frac{cB}{2\pi r}$
ω	Rotor angular speed [rad/s]

4.2 Introduction

With the increasing size of wind turbines and the increasing volume of wind turbines the importance of the exact prediction of power and load performance has become even more crucial. Several attempts of improving the performance have been made using different airfoil designs, different philosophies in the rotor design and the control. The

different rotor design philosophies are, e.g. high design lift versus low design lift, large versus small root chord, winglets versus no winglets and (active) stall regulation with constant rotor speed versus pitch regulation with variable rotor speed.

Several researchers have contributed to the insight into rotor design. Snel [1,2] describes wind turbine aerodynamics in general and gives an overview of the available methods to compute the aerodynamic rotor performance. Fuglsang [3] describes the methods needed in the rotor design process in terms of a guideline and Tangler [4] gives a short historical overview of the rotor design investigations. Also, aerodynamic optimization of rotors are described by Fuglsang and Madsen [5], Giguere and Selig [6] and Nygaard [7]. Details in rotor design to increase the power efficiency have been investigated by several researchers, e.g. Johansen et al. [8] and Madsen et al. [9] investigated especially the root part of rotors and found that a new root design of the rotors did not increase the power performance significantly. However, the interaction between different parameters in the rotor design, such as Tip-Speed-Ratio, Reynolds number etc. still needs to be investigated simultaneously when addressing design of rotors with maximum power performance.

This chapter describes the parameters influencing the aerodynamic rotor efficiency for rotor sizes between 1kW to 5MW

This chapter describes an analysis carried out on wind turbine rotors ranging from 1kW of the size 1.75m in diameter to 5MW of the size 126m in diameter, where the Reynolds number, tip-speed-ratio, the assumption of clean airfoils versus contaminated airfoils and large versus small blade root chords are investigated. Thus, the performance on the small scales, which is in the order of the airfoil chord scale, and the performance on the large scales, which is in the order of the rotor diameter, are all included. The analysis is divided into an investigation of different airfoils and their performance in two dimensions (2D) and an investigation of rotors in three dimensions (3D) based on different design parameters and using the blade element momentum (BEM) method.

4.3 Analysis of 2D airfoils

Blade element momentum (BEM) method applied on a 2D airfoil

The local power efficiency correspond-ding to 2D airfoils was investigated.

Maximum power performance is desired in aerodynamic rotor design. The power performance is commonly expressed in terms of the power coefficient, C_P, and can for an annular element of the rotor disc be written as:

$$C_P = \frac{dF_{driving} r\omega}{½\rho V_0^3 dA} \ . \tag{4.1}$$

Eqn. (4.1) can be written as:

$$C_P = \left[(1-a)^2 + x^2(1+a')^2\right] x c_x \sigma \ . \tag{4.2}$$

In the relations above, the axial and tangential induction, respectively, are computed with the tip loss correction F=1 in the 2D analysis. Analyzing the momentum theory, which is the basis of the BEM method, shows that the power coefficient C_P is maximized if the axial induction a=1/3. In this investigation of rotor performance this is assumed to be valid even though advanced computational techniques show that the axial induction should be slightly higher to obtain maximum power efficiency. With a=1/3, equation (4.2) turns into:

$$C_P = \left[\frac{4}{9} + x^2(1+a')^2\right] x c_x \sigma, \tag{4.3}$$

where x is chosen and a' and c_x is computed and σ is computed through the axial induction, a. Assuming that a=1/3:

$$\sigma = \frac{2\sin^2\phi F}{c_y}. \tag{4.4}$$

These equations are solved iteratively because of the dependency between a', c_x, c_y, σ and ϕ. In the 2D airfoil analysis the aerodynamic performance of airfoils is expressed in terms of the lift-drag ratio, c_l/c_d and the corresponding c_l:

$$\begin{aligned} c_x &= c_l(\sin\phi - \frac{1}{c_l/c_d}\cos\phi) \\ c_y &= c_l(\cos\phi + \frac{1}{c_l/c_d}\sin\phi) \end{aligned} \tag{4.5}$$

Investigating the 2D airfoil characteristics for an airfoil, eqn. (4.5), shows that maximum C_P is found where c_l/c_d is maximum. Comparisons of 2D airfoils with different c_l/c_d ratios are shown in Figure 4-1. The plot shows five different airfoils with c_l/c_d=50, 100, 150, 200 and ∞ (inviscid flow). The different c_l/c_d values range from rather poor airfoil efficiency (c_l/c_d=50) to very good airfoil efficiency (c_l/c_d=200). The upper limit for the efficiency is shown by the curve corresponding to inviscid flow i.e. no viscous effects in the flow, c_d=0. It is seen that C_P approaches the Betz limit for high x when inviscid flow is assumed. However, for realistic ratios of c_l/c_d there are maxima for C_P at different x depending on the value of c_l/c_d. Thus, maximum C_P is found around x=2.4 for c_l/c_d=50 and around x=3.8 for c_l/c_d=200. Below the plot, three airfoil sections are seen reflecting the solidity and the twist of the airfoil corresponding to x=2, 4 and 6, respectively. These changes in solidity and twist can be seen on wind turbine blades because x changes from the tip speed ratio at the tip to zero at the root. Thus, at the inner part of a blade the chord and twist are large and at the tip they are small.

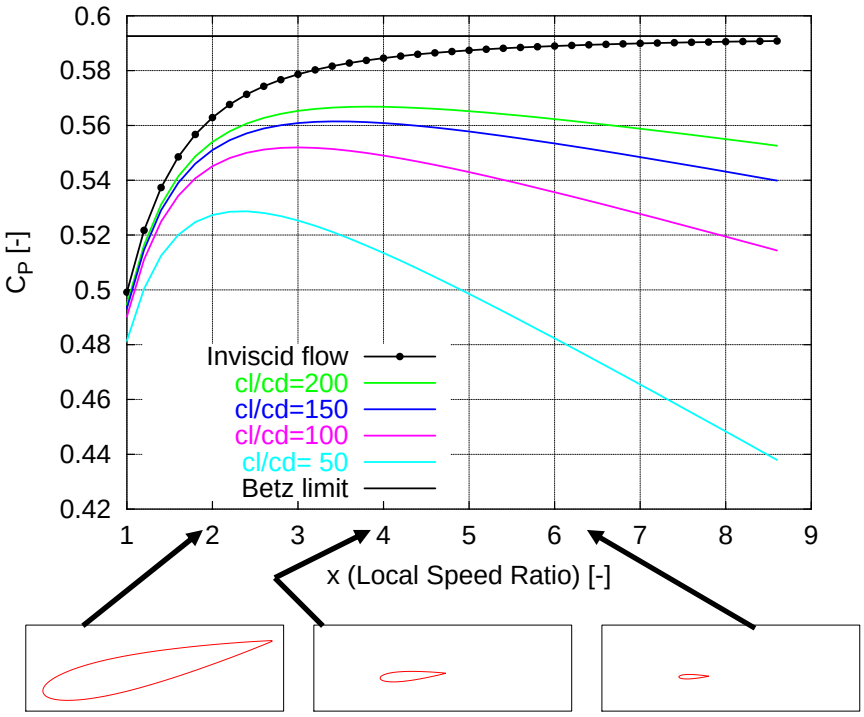

Maximum local power efficiency varies from around 0.52 to around 0.55 corresponding to airfoil efficiencies c_l/c_d=50 and c_l/c_d=200, respectively.

Figure 4-1 C_P *versus local speed ratio,* x, *for different* c_l/c_d*-ratios. Below the plot the size in terms of solidity,* σ*, and the twist of airfoils corresponding to* x*=2, 4 and 6 are seen.*

In Figure 4-2 the different terms in the calculation of C_P, eqn. (4.3), are seen for c_l/c_d=150.

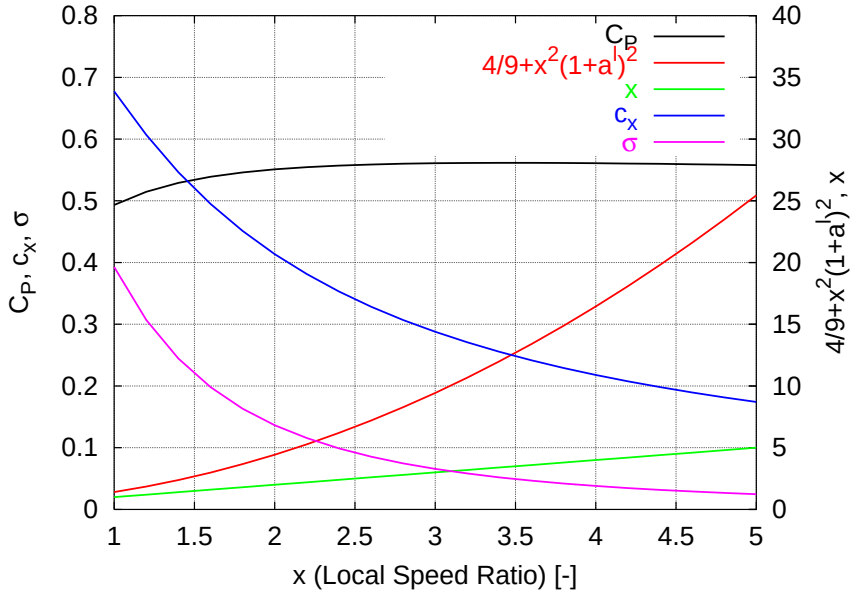

Figure 4-2 Plot of the different terms in the calculation of C_P*, eqn. (4.3) for* c_l/c_d*=150.*

It is seen that the driving force coefficient (c_x) and the solidity (σ) decrease as the local speed ratio (x) increases, whereas the normalized relative velocity $(4/9+x^2(1+a')^2)$ and the local speed ratio (x) increases as the local speed ratio (x) increases. The product of the four curves is C_P, which is also seen on the plot and has a maximum at around x=3.4 for this c_l/c_d value.

Reynolds number dependency and roughness sensitivity

The Reynolds number dependency on the local power efficiency was investigated

Wind turbines of today are manufactured from around 1kW (around 2m rotor diameter) to 5MW (around 125m rotor diameter). Because the size of the rotors and thereby the chord length of each blade section varies with the turbine size, also the Reynolds number (Re) and thereby the airfoil performance varies with wind turbine size. For small wind turbines Re is 200,000 or below whereas it is 6,000,000 or more for the largest wind turbines.

The aerodynamic performances for several airfoil families have been investigated using the panel code XFOIL by Drela [10]. In Figure 4-3 the maximum c_l/c_d as function of Re are seen for the Risø-B1 airfoil family designed for wind turbine rotors. This family is used as an example. Other airfoil families show the same trend where maximum c_l/c_d increases a lot until around Re=2,000,000. For Re between 2,000,000 and 9,000,000 maximum c_l/c_d still increases, but at a slower rate. Above Re=9,000,000 the increase in maximum c_l/c_d is small.

The assumption of fully turbulent flow probably under-predicts the performance because the predicted c_d is too high. This assumption commonly simulates roughness at the leading edge caused e.g. by bugs or dust. However, in the case of contamination of the airfoils there is a risk that $c_{l,max}$ will be reduced more than predicted by this assumption. On the other hand, the assumption of free transition probably over-predicts the performance because c_d is somewhat too low and c_l including $c_{l,max}$, is somewhat too high. However, if the flow has a low turbulence intensity at small scales, i.e. at the size

of an airfoil chord, and the airfoils are clean with no roughness at the leading edge, the performance will probably be close to the one predicted with free transition. The two assumptions as shown in the plots express the uncertainty in the airfoil performance concerning the sensitivity to leading edge roughness.

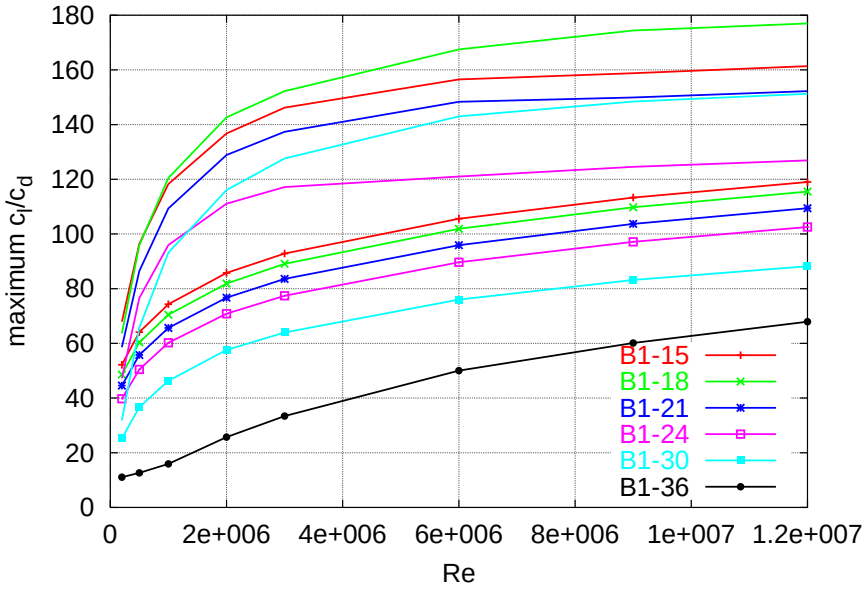

Big Reynolds number dependency on the 2D airfoil efficiency was seen for low Reynolds numbers below 2 million – but the efficiency increases for increasing Reynolds number

Figure 4-3 Maximum c_l/c_d *ratio versus Re for the Risø-B1 family. Lines with dots show XFOIL computations assuming turbulence from the very leading edge. Lines without dots show XFOIL computations assuming free transition with the* e^n *model with* n=*9.*

Comparing maximum c_l/c_d variations with the relative thickness at constant *Re* shows that maximum c_l/c_d scales more or less with the relative thickness. For fully turbulent flow at *Re*=6,000,000 the maximum c_l/c_d is reduced from 106 for the Risø-B1-15 (t/c=15%) to c_l/c_d=50 for the Risø-B1-36 (t/c=36%). This corresponds to a reduction in local C_P for the airfoil from around 0.55 to 0.53, see Figure 4-1. If the airfoils can obtain the performance according to the assumption of free transition, maximum c_l/c_d for the thin airfoils will be around 160, so that C_P can be increased from 0.55 to 0.56.

4.4 Rotor analysis using the blade element momentum (BEM) method

The power efficiency for the complete rotor was investigated using different degrees of simplifications

The investigation of the rotor performance is made in three steps:

1. Rotors with blades having constant maximum lift-drag ratio, c_l/c_d, are investigated.
2. Four different existing rotors of different sizes are designed to many different tip speed ratios, *X*, equipped with airfoils and having the same absolute thickness distribution as the existing blades to maintain the required stiffness.
3. The energy production including the regulation of the largest rotor, 5MW, is investigated.

Rotors with constant maximum lift-drag ratio

Extending the investigation to rotors instead of 2D airfoils requires only minor changes in the setup because the rotor performance is the sum of the performance of the 2D sections along the rotor blade. This is true as long as the BEM method is used because this method assumes that the rotor performance can be treated in 2D in annular elements

One simplification was to assume constant airfoil efficiency along the complete blade length

of the rotor disc. Thus, eqns. (4.3) to (4.5) are used, but now with the Prandtl tip correction F defined according to Glauert [11] as:

$$F = 2\arccos(\exp(-f))/\pi \tag{4.6}$$

with $f = \frac{B(R-r)}{2r\sin(\phi)}$. In Figure 4-4 C_P as function of the tip speed ratio, X, is seen for different values of the maximum lift-drag ratio, c_l/c_d, which is constant along the blade. Also, it is assumed that that the number of blades B=3. It is seen that C_P is around 0.46 for X_{design} around 6 if maximum c_l/c_d=50 and increases to C_P around 0.525 for X_{design} around 12 if maximum c_l/c_d=200. The upper limit for the efficiency is shown by the curve corresponding to inviscid flow. It is seen that C_P approaches the Betz limit for high X when inviscid flow is assumed. If only two blades were used the result would be different with the maximum C_P at higher tip speed ratio, X. From the 2D analysis the local tip speed, x, should be between 2.4 and 3.8 for maximum c_l/c_d between 50 and 200 to obtain maximum local C_P. This analysis for the rotor shows that the tip correction causes the maximum global C_P to appear at a value of the Tip Speed Ratio, X, that is greater than the Local Speed Ratio, x, corresponding to maximum local C_P. Thus, the optimum x should be between 2.4 and 3.8, whereas the optimum X should be between 6 and 12, for maximum c_l/c_d between 50 and 200.

Airfoil efficiencies between c_l/c_d=50 and c_l/c_d=200 result in rotor power efficiencies between 0.46 and 0.525, respectively

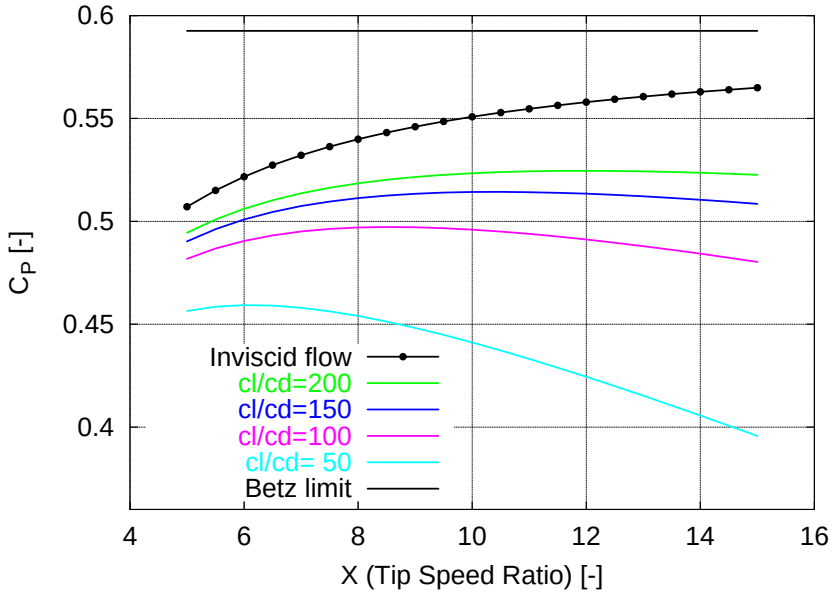

Figure 4-4 Rotor C_P as function of tip speed ratio for different lift-drag ratios constant along the blade.

Four rotors with constraints on the absolute thickness distribution

Another simplification was to assume constant absolute thickness distribution for different design tip speeds

To reveal the aerodynamic performance for real rotors, four different rotors where selected, so both the Reynolds number, *Re,* and the thickness distribution were taken into account. The blades were:

- Wind Dynamic 3WTR designed for 1kW wind turbines with diameter D=1.75m
- LM8.2 designed for 100kW wind turbines with diameter D=19.0m
- LM19.1 designed for 500kW wind turbines with diameter D=41.0m
- NREL Reference Wind Turbine blade (NREL-RWT) made for theoretical investigations for 5MW wind turbines with diameter D=126.0m

Based on these blades and their absolute thickness distributions, several blades were designed for different tip speed ratios, X. The designs were based on airfoils of different relative thicknesses and computed for different Re. Thus, the airfoil characteristics used in the design corresponds to both relative thicknesses and Re. Three different airfoil series were used:

- The Risø-B1 family with thicknesses 15% to 36%
- The DU family with thicknesses 18% to 35%
- The NACA636xx with thicknesses 15% to 21% and the FFA-w3-xxx with thicknesses 24% to 36%

In Figure 4-5 the thickness distribution of the blades are seen. The root thicknesses follow the blade size, but the outer 80% of the blades does not follow the blade size.

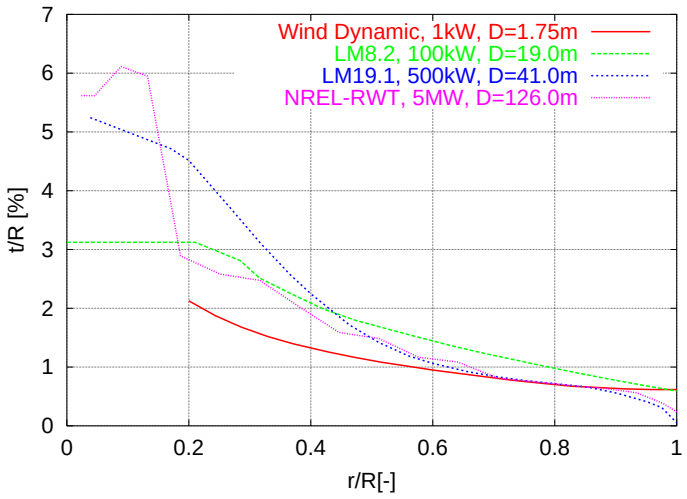

Figure 4-5 Distribution of absolute thickness for the four different blades.

The airfoil characteristics for the airfoil families were computed using XFOIL with its 2D assumption. For each airfoil and Re the maximum c_l/c_d and the corresponding c_l, the design lift, $c_{l,design}$, were determined. Based on the design lift the blade planforms were designed for different tip speed ratios using eqns. (4.3) to (4.5) for maximum aerodynamic efficiency at each radial station. This means that the chord length at the root part of the blade was not reduced, which is common on some modern wind turbine rotors. In the computations the airfoil characteristics along the blade are described by interpolation of $c_{l,design}$ and maximum c_l/c_d.

Figure 4-6 and Figure 4-7 show the chord and relative thickness distribution for the LM19.1 blade for different tip speed ratios, X, assuming fully turbulent airfoil flow. For increasing X the chord is decreasing and the relative thickness is increasing to maintain the absolute thickness. Since XFOIL computations only up to a relative thickness of t/c=36% were used, designs for X greater than around 8 are somewhat uncertain. At the inner part of the rotor the airfoil characteristics are described by interpolation of $c_{l,design}$ and maximum c_l/c_d between the 36% airfoil and a cylinder. Furthermore, XFOIL computations carried out for airfoils with relative thickness of t/c=30% or greater are as well uncertain. This means that rotors designed for X>6.5 is slightly uncertain, with higher uncertainty for X>8.

The he chord lengths are decreasing and the relative thicknesses are increasing for increasing design tip speed

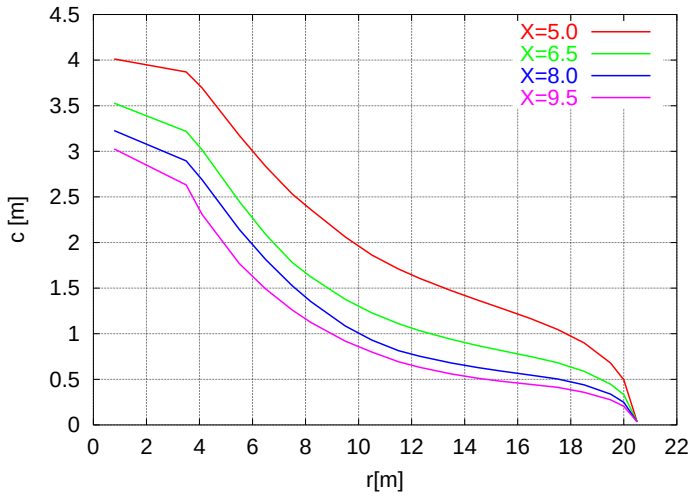

Figure 4-6 Chord distribution for the LM19.1 rotor for different tip speed ratios, X, using the Risø-B1 series.

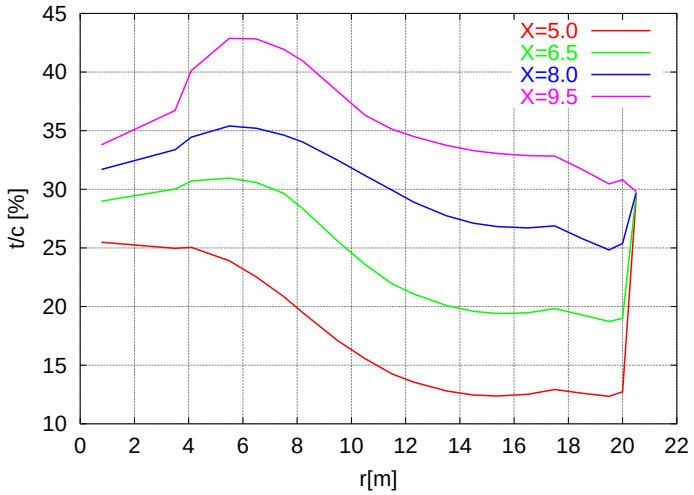

Figure 4-7 Relative thickness distribution for the LM19.1 rotor for different tip speed ratios, X, using the Risø-B1 series.

Figure 4-8 and Figure 4-9 show the power coefficient, C_P, versus the tip speed ratio, X, for the four different rotors assuming fully turbulent and free transition airfoil flow, respectively. The maximum C_P and the corresponding X_{design} for each rotor can be seen in Table 4-1. From the plots and the table it is seen that maximum C_P increases with increasing rotor diameter. Also, it can be seen that the tip speed ratio, X_{design}, corresponding to the maximum C_P moves towards higher values for bigger sizes of rotors. Based on the investigations in 2D it can be concluded that the increase in maximum C_P is caused by the increase in Re. Thus, the Reynolds numbers for the different rotors are approximately:

- Wind Dynamic: Re = 100,000,
- LM8.2: Re = 1.2mio,
- LM19.1: Re = 2.5mio and
- NREL RWT: Re = 7mio.

Comparing Figure 4-8 and Figure 4-9 show the difference in the assumption of fully turbulent and free transitional airfoil flow. As discussed in the section “Reynolds number dependency and roughness sensitivity” the assumption of fully turbulent flow probably is

somewhat conservative whereas the assumption of free transition probably is somewhat optimistic. Therefore, the rotor designs should be somewhere between these extremes.

Table 4-1 Maximum C_P and design X for the four different rotors using Risø-B1 airfoil family.

		Wind Dynamic	**LM8.2**	**LM19.1**	**NREL-RWT**
Diameter [m]		1.75	19.0	41.0	126.0
Fully turbulent airfoil flow	*Max.* C_P	0.450	0.465	0.473	0.480
	X_{design}	5.50	5.75	6.25	6.50
Free transition airfoil flow	*Max.* C_P	0.465	0.484	0.493	0.501
	X_{design}	5.75	6.25	7.50	8.25

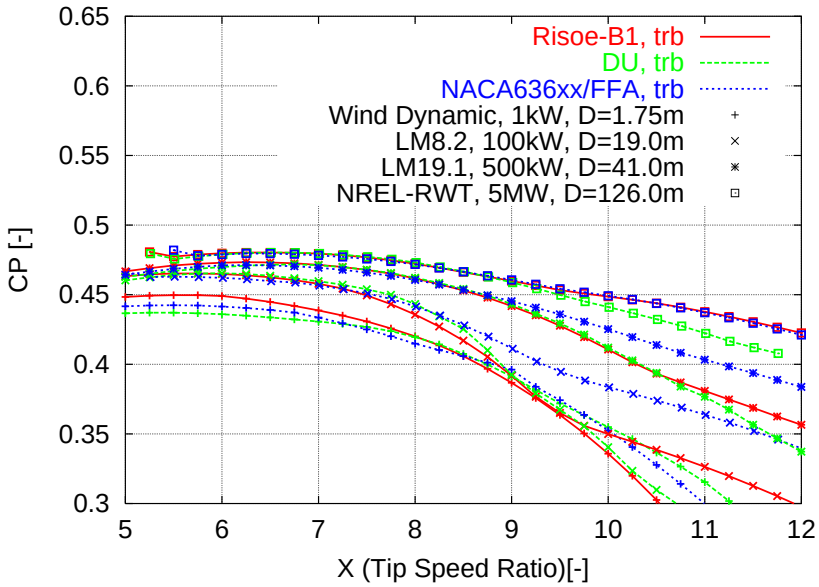

The power efficiency and the design tip speed increase with the rotor size assuming fully turbulent flow

Figure 4-8 C_P versus tip speed ratio, X, for four different sizes of rotors and three different kinds of airfoil families assuming fully turbulent flow on airfoils.

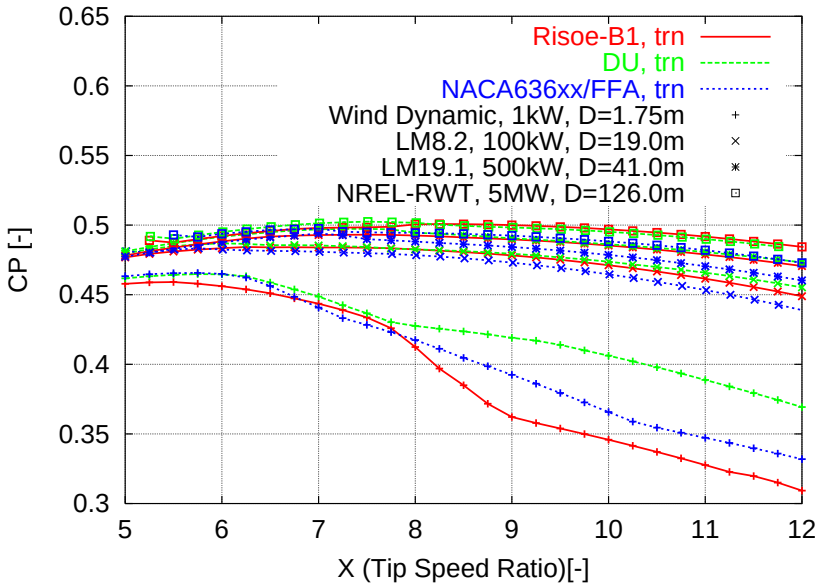

The power efficiency and design tip speed also increase with assuming free transitional flow instead of fully turbulent flow

Figure 4-9 C_P versus tip speed ratio, X, for four different sizes of rotors and three different kinds of airfoil families assuming free transition on airfoils.

Aerodynamic performance for the NREL RWT 5MW with different rotors

The influence of varying design tip speeds on the annual energy production was investigated for a 5MW rotor

In the previous sections only maximum C_P at different tip speed ratios, X, were shown. However, the focus in wind turbine design should be to minimize price pr. energy. This means that the annual energy production for a given design should be maximized considering also the corresponding loads. This requires the inclusion of the control, because the rotor should operate between e.g. 5 and 25m/s. Therefore, the NREL RWT rotor was investigated to find the tip speed ratio that was optimal in terms of energy production. Blades were designed at four different X and equipped with the Risø-B1 airfoil family with the assumption of free transitional airfoil flow. The variation in Re was included. HAWTOPT [12] was used for the design of the rotors and in the prediction of the performance. The objective in the design process was to maximize C_P maintaining the absolute thickness distribution to maintain the blade stiffness. Along the blade span each airfoil section did not necessarily operate at the design lift, unlike the designs in the former section. One type of design was to limit the maximum chord to 4.65m equivalent to the existing NREL RWT blade. The other type of design was to set no limits on the maximum chord. The annual energy production (AEP) was predicted using a Weibull distribution where the mean wind speed was V_{mean}=8m/s, the roughness parameter was z_0=0.01 (smooth onshore surface), the hub height was h_A=89.56 and the constant C=1.9.

Figure 4-10 shows C_P and AEP versus X with and without constraints on the maximum chord. For the blade with unconstrained maximum chord it is seen that the AEP follows C_P, i.e. AEP has its maximum at the same X as C_P. Also, it can be seen that 2% change in C_P (e.g. from C_P=0.50 to 0.49) results in around 1% change in AEP (e.g. from 19.4GWh to 19.2GWh). Furthermore, constraining the chord to maximum 4.65m reduced C_P with between 2% and 3%, which is between 1% and 1.5% on AEP. The plot indicates that if the blade has a limited maximum chord, the design tip speed ratio, X_{design}, should be decreased to obtain maximum C_P. Finally, this investigation indicates that optimizing blades for C_P is a simple way to optimize AEP. It should be noted that X_{design} is found to be lower in the investigation using HAWTOPT compared to the results shown in Figure 4-9. This is due to the uncertainty of the performance of the thickest airfoil sections as described in section “Four rotors with constraints on the absolute thickness distribution”. Thus, more knowledge of the performance of thick airfoils could change the obtained results. Finally, consideration of the loads should be taken into account and this could change the conclusion concerning the optimal tip speed ratio.

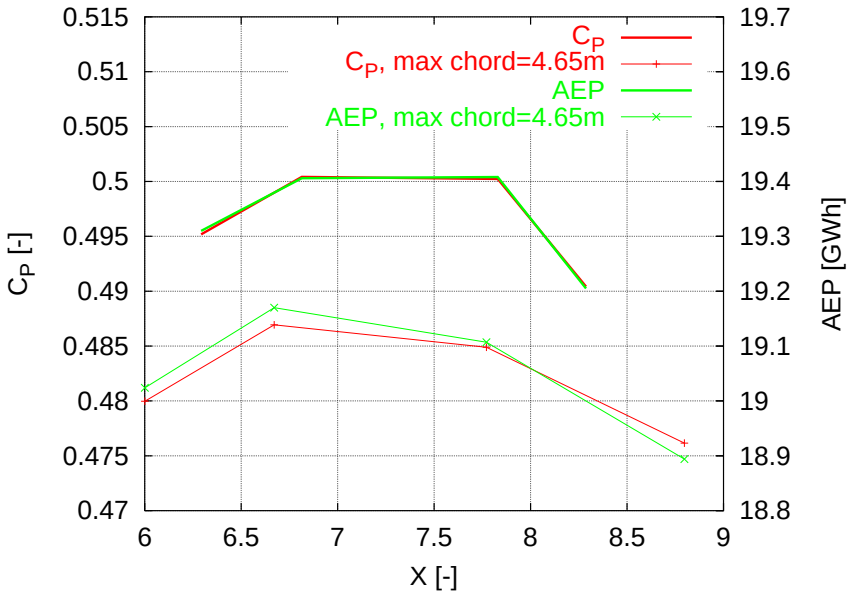

The maximum power efficiency and the maximum annual energy production correlates well with design tip speed

Figure 4-10 C_P and AEP versus X for rotors with and without constraints on the maximum chord.

4.5 Conclusion

In this work the influence of different key parameters on the power efficiency, C_P, and loads was investigated. The work was divided into an analysis of 2D airfoils/blade sections and of entire rotors.

In the analysis of the 2D airfoils it was seen that there was a maximum of the local C_P for airfoils with finite c_l/c_d values. The local speed ratio should be between 2.4 and 3.8 for airfoils with c_l/c_d between 50 and 200, respectively, to obtain maximum local C_P. Investigation of the Reynolds number (Re) dependency of the Risø-B1 airfoil family showed that at low Re=200,000 the maximum c_l/c_d was around 50 corresponding to a local C_P of around 0.53 and at high Re=9mio c_l/c_d could be up to 180 corresponding to a local C_P of over 0.56. Thus, Re has a significant impact on C_P and especially for Re<2mio corresponding to rotors below approximately 400kW this impact is pronounced.

The investigation of C_P for rotors was made with three blades and showed that with the assumption of constant maximum c_l/c_d along the entire blade, the design tip speed ratio changed from X_{design}=6 to X_{design}=12 for c_l/c_d=50 and c_l/c_d=200, respectively, with corresponding values of C_P=0.46 and C_P=0.525. Thus, the design tip speed ratio and C_P are very dependent on the airfoil efficiency.

An analysis of existing rotors re-designed with new airfoils but maintaining the absolute thickness distribution to maintain the stiffness showed that big rotors are more aerodynamically more efficient than small rotors. It also showed that the design tip speed ratio was dependent on the rotor size and on the assumptions of the airfoil flow being fully turbulent (contaminated airfoil) or free transitional (clean airfoil). The investigations showed that rotors with diameter D=1.75m, should be designed for X_{design} around 5.5, whereas rotors with diameter D=126m, should be designed for X_{design} between 6.5 and 8.5, depending on the airfoil performance.

To investigate the annual energy production, *AEP*, four blades were designed for a rotor with D=126m corresponding to 5MW. With no constraints on the maximum chord, it was seen that *AEP* had its maximum at the same tip speed ratio as C_P had its maximum. If the maximum chord was constrained to 4.65m according to the existing 126m rotor, it was seen that *AEP* and C_P had its maximum at a slightly lower tip speed ratio compared to the blades with no constraints on the maximum chord. Also, it was observed that an increase of 2% in C_P corresponded to an increase in *AEP* of around 1%. Finally, to find the optimal tip speed ratio, also the loads computed using aeroelastic simulations including rotor control should be considered to find the minimum cost pr. kWh.

4.6 References

[1] Snel, H. Review of the present status of rotor aerodynamics, Wind Energy. 1 (1998) 46-69

[2] Snel, H., Review of Aerodynamics for Wind Turbines, Wind Energy. 6 (2003) 203-211

[3] Fuglsang, P., Aerodynamic design guidelines for wind turbine rotors. In: CD-Rom proceedings. 4. GRACM congress on computational mechanics, Patras (GR), 27-29 Jun 2002. Tsahalis, D.T. (ed.)

[4] Tangler, J., 'The Evolution of Rotor and Blade Design', NREL/CP-500-28410, July 2000, Presented at the American Wind Energy Association WindPower 2000, Palm Springs, California, April 30.May 4, 2000

[5] Fuglsang, P. L. and Madsen, H. A., 'Optimization Method for Wind Turbine Rotors', Journal of Wind Engineering and Industrial Aerodynamics, Vol. 80, pp. 191-206, 1999.

[6] Giguere, P, and Selig, M. S., 'Blade Geometry Optimization for the Design of Wind Turbine Rotors', 2000 ASME Wind Energy Symposium, Reno NV, Jan. 2000.

[7] Nygaard, T. A., 'Optimization of Wind Turbine Rotors', doctoral thesis, Norwegian University of Science and Technology, ISBN 82-471-0472-5, Nov. 1999.

[8] Johansen, J., Madsen, H.A., Gaunaa, M., Bak, C., '3D Navier-Stokes Simulations of a rotor designed for Maximum Aerodynamic Efficiency',45. AIAA Aerospace Sciences Meeting and Exhibit, Reno, NV, 8-11 Jan 07

[9] Madsen, H.A..;Mikkelsen,R.; Johansen, J.; Bak, C.; Øye, S.; Sørensen, N.N., Inboard rotor/blade aerodynamics and its influence on blade design. In: Bak, C. (ed.), Research in Aeroelasticity EFP-2005. Risø-R-1559(EN)

[10] Drela, M. "XFOIL, An Analysis and Design system for Low Reynolds Number Airfoils", Low Reynolds Number Aerodynamics, vol. 54 (1989) In Springer-Verlag Lec. Notes in Eng

[11] Glauert, H., "Airplane propellers". Aerodynamic Theory (ed. Durand, W.F.), Dover Publication Inc., New York, (1963), Chapter VII, Div. L, 251-268.

[12] Fuglsang P. and Thomsen, K., Site Specific Design Optimization Of Wind Turbines. ASME J. Solar Engineering, Vol. 123, pp 296-303, 2001

5 Estimation of possible increase in Cp by use of Winglets

Mac Gaunaa, Jeppe Johansen

The present work contains theoretical considerations and computational results on the nature of using winglets on wind turbines. The theoretical results to be presented sheds light on the physical understanding of what winglets do on wind turbine rotors, and whether we can expect to break the Betz limit using winglets or not. The numerical work includes optimization of the power coefficient for a given tip speed ratio and geometry of the span using a newly developed Free Wake Lifting Line (FWLL) code, which takes into account also viscous effects and self induced forces. The results will also show which is most efficient; upwind or downwind winglets. Lastly, the results from the code will be used to design a rotor with a 2% downwind winglet, which is computed using the Navier-Stokes solver EllipSys3D. The results from these computations will be compared to the results from the free wake lifting line code.

5.1 Introduction

Many wind turbine sites have restrictions on rotor diameter in one form or another. In those cases, the only way the power production can be optimized at any specific wind velocity is through maximizing the power coefficient, *Cp*, of the wind turbine. To that end, winglets can be used, since these can improve the power production without increasing the projected rotor area.

Winglets can improve power production without increasing the projected rotor area.

Winglets have been studied extensively for non-rotating applications such as airplanes and sailplanes. The total drag on a three-dimensional wing basically consists of two parts: a viscous (2D) part, and an induced (3D) part. The induced drag stems from the lift because the trailing vortex system behind the wing induces velocities perpendicular to the free stream direction. The local inviscid lift forces act perpendicular to the relative velocity, so the induced velocities give rise to forces in the direction of the free stream. This is what is called induced drag. Since the downwash is proportional to the lift, the induced drag scales with the square of the lift (see for instance the excellent review paper by Kroo[1]). Essential works within the field of winglets on non-rotating wings include Munk's[2] pioneering lifting line work, which showed that the optimal normal-wash distribution for a non-planar wing is proportional to cosine of the dihedral angle. The same work showed that the condition for a minimum drag does not depend on the longitudinal coordinates, which includes the effects of sweep. It can be shown that a vertical surface (with no viscous drag) starting at the tip of the wing is worth approximately 45% of its height as additional span[1]. Other works within non-rotating winglet literature include references by Witcomb[3] Jones[4], Eppler[5] and Maughmer[6]. These works all include considerations on viscous effects. Whitcomb[3] outlines a design approach for the design of winglets on airplanes. Jones[4] uses the variational approach to find the optimum load distribution for wing-winglet combinations with restrictions on bending moments, which is related to a considerable portion of the weight of the wing. Eppler's work[5] uses an ingenious method to investigate the effect of the assumption of a rigid wake, as it was in the early works dealing with winglets. This investigation results in a determination of what Eppler dubs induced lift forces. Maughmer's work[6] deals with how to use winglets to improve the

The physics behind winglets are well-understood for airplane applications.

performance of sail planes, which work under a wide range of operating conditions and restrictions (multi point optimization). As explained very nicely in Maughmer's works, the main purpose of adding a winglet to an airplane wing is to decrease the total drag for a given lift. Reduction of total drag is obtained if the additional drag from the winglet is less than the reduction in induced drag on the remaining blade. The art is then to design a winglet which optimizes drag reduction for a given lift. The working principle behind the winglet in the non-rotating case is that the winglet diffuses and moves the tip vortex away from the main wing/wake plane, which reduces the downwash and thereby the induced drag on the wing.

Compared to the number of references on winglets on non-rotating wings, the work done so far for application of winglets on rotors is fairly limited.

A tip attachment that has been investigated by Delft university (Van Holten[7]) and Mie university (Shimizu et al.[8]), is the Tip-vane, or Mie-vane, which is basically a T-wing at the tip of the main wing. At first sight, this device looks somewhat like a winglet for wind turbines. The main role of this device, however, is to act as a concentrator system, increasing mass flow through the main rotor disc due to the formation of a ring-vortex-like vortical structure emanating from the upwind tips of the Mie-vanes. Since the topic to be investigated in the present work is the use of standard one-sided winglets, which does not act as a concentrator system, the similarity between Mie vanes and winglets for wind turbines is not very great. According to the wind tunnel measurements [8], the maximum power coefficient, *Cp*, obtained with a Mie-vane was *Cp*=0.45 at a tip speed ratio of 4. This corresponded to a 27% increase compared to the case without tip attachments. Furthermore, according to the measurements, the Mie-vane has not proven to increase *Cp* for a turbine for tip speed ratios above 8.

Compared to the work done on winglets on airplanes, there has not been much work focusing on winglets on rotors.

For the application of winglets on horizontal-axis wind turbines, previous works has been done by Van Bussel [9], Imamura *et al.*[10] and Johansen[11-12]. Van Bussel[9] developed a momentum theory for winglets on horizontal-axis wind turbines, explaining the positive effect of a winglet on a rotor by the downwind shift of the wake vorticity, which the authors of the present work believe is erroneous, as shall be shown in the section on simple modeling later on. The works by Imamura *et al.*[10] and Johansen[11-12] are numerical in nature, as the former work is based on a free-wake vortex-lattice method. Johansen's work is based on Navier-Stokes simulations with the CFD code EllipSys3D, and predicts an increase in *Cp* of 1.74% on a modern MW sized turbine.

Along the same lines as for the non-rotating case, the main purpose of adding a winglet to a wind turbine rotor is to decrease the total drag from the blade and thereby increase the aerodynamic efficiency of the turbine. Reduction of total drag is obtained if the additional drag from the winglet is less than the reduction in induced drag on the remaining blade. The art is then to design a winglet which maximizes power production for the whole rotor.

The use of winglets on rotors other than wind energy applications was performed by Müller & Staufenbiel[13] and Müller[14], and deals with using winglets on helicopters.

The current work aims at describing the mechanisms of winglets on turbine rotors, and furthermore to determine the maximum achievable aerodynamic efficiency, defined as the mechanical power coefficient, *Cp*, for wind turbine rotors with winglets, using both a newly developed Free Wake Lifting Line (FWLL) method and the CFD code EllipSys3D. This is of interest to both the wind turbine industry as well as the research community.

5.2 The Problem in a Nut-Shell

By considering a lifting-line type model for a wind turbine rotor with winglets, an interesting insight into what winglets do may be obtained. Consider the model outlined in Figure 5-1.

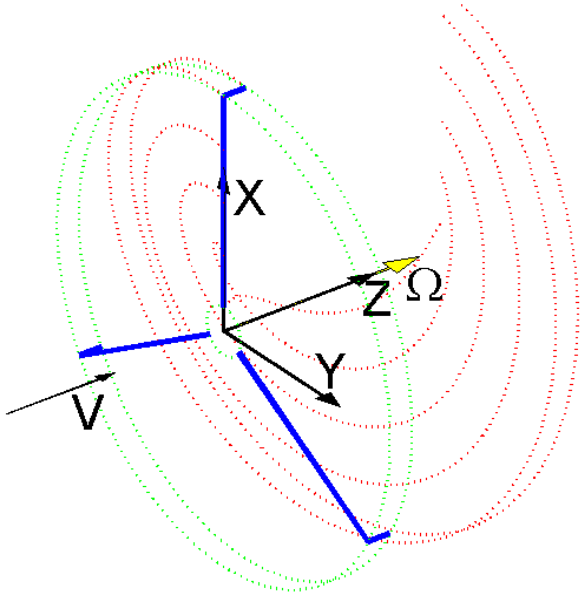

Figure 5-1 Coordinate systems used in lifting line analysis.

The force per unit length vortex element was given by Joukowski as $\underline{F}=\rho\cdot\underline{V}_{rel}\times\underline{\Gamma}$, where $\underline{\Gamma}$ is the circulation vector, $\underline{V}_{rel}$ is the velocity vector relative to the vortex element, and ρ is the density of the fluid. Whenever circulations and velocities are used without vector notation, it is referred to scalars, such as for instance the magnitude of the circulation, Γ. Using the notation from Figure 5-1, we get for the forces on the main wing that lies on the X-axis:

$$\vec{F}_{main}=\rho\vec{V}_{rel}\times\vec{\Gamma}=\rho\Gamma\begin{bmatrix}0 & \leftarrow & \textit{Radial forces}\\ V+V_{iZ} & \leftarrow & \textit{Tangential forces ("Power")}\\ \Omega X-V_{iY} & \leftarrow & \textit{Axial forces ("Thrust")}\end{bmatrix} \tag{5.1}$$

And for the forces on the winglet:

$$\vec{F}_{winglet}=\rho\vec{V}_{rel}\times\vec{\Gamma}=\rho\Gamma\begin{bmatrix}-\Omega X+V_{iY} & \leftarrow & \textit{Radial forces}\\ -V_{iX} & \leftarrow & \textit{"Power" contribution from winglet}\\ 0 & \leftarrow & \textit{No thrust generation!}\end{bmatrix} \tag{5.2}$$

Note, that subscript *i* refer to all induced velocities on a specific point on the rotor, which includes both the classical induced velocities, as known from blade element theory, plus tip effects and self-induced velocities. The expression for the force on the winglet is derived for a downwind winglet, corresponding to what is shown in Figure 5-1. If an upwind winglet is used, the forces change sign.

As seen from the result, the component of the forces that contribute to the power production from the main wing is a product of circulation and the effective axial velocity. Due to the "vortex laws" any change in circulation along the wing is trailed into the wake, a higher circulation generally results in lower effective axial velocities. The problem of finding the optimal circulation distribution for a non-wingletted rotor was

treated by Goldstein[15]. However, when a winglet is present, the loading can be extended onto this, which makes possible for the outer radial positions to run with higher bound circulation, and thus, increased production. Furthermore, the trailed vorticity emanating from the winglet is brought downstream, and out of the main rotor-plane. Both of these effects have a positive effect on power production on the main wing; the latter being analogue to the benefit from winglets in the non-rotating case. The power contributing forces from the winglet itself includes a product between bound circulation and negative axial velocity. Due to the decrease of the axial velocity in the axial direction, it is evident from mass conservation that the radial flow is positive, and therefore, that, for the downwind winglet, the power production is negative. The benefits that the main part of the wing enjoys come at this cost. We will go into this in more detail later. Considering this argument, an upwind winglet might seem like a better choice, since in this case the power production on the winglet itself would be positive. In the upwind case, however, the vorticity from the winglets are trailed at an upstream position (axial direction), which reduces the axial velocities, and thereby, the power production, on the main rotor.

The power production from the simple winglet itself may be positive or negative, depending on the radial flow component, but thrust is always zero.

As seen from the equations, the thrust is mainly affected due to the increased loading near the tip of the main rotor; the winglet itself produces no thrust.

5.3 Simple Modelling: Actuator Cap/Vortex Tube Theory

In order to shed some light on the physics behind using winglets on wind turbine blades, we consider a simple model analogous to a non-wingletted model by Øye[16]. In this model we consider a wind turbine with winglets, as shown in Figure 5-2, with infinitely many uniformly loaded blades.

Figure 5-2 Geometry used in the actuator cap/vortex tube model. Black: actuator cap. Blue: distinct root vortex and tip vortex tube.

Due to the uniformly loaded blades, vorticity is shed at the root and tip only. The root vortices combine to one single vortex along the rotor axis, and the vorticity shed from the tips form a vortex tube, as shown in Figure 5-2. The results from this model do not include tip effects, since the number of blades is infinite, so the results can be compared to basic actuator disc computations. A more suitable term for the present geometry is actuator cap, which is adopted in the following.

For a model like the present, it can be shown [16] that all axial and radial induction in the actuator cap case comes from the outer vortex wake tube only. This means that the axial component of the flow passing through the plane through the winglet tips, where the tip vorticity is shed, is independent of the axial position of the main rotor. From application of mass conservation through the actuator cap only, it follows that

$$\int_0^R (V + V_{iZ}(x,0))2\pi x dx = \int_o^{Lwl} 2\pi R V_{iX}(R,z)dz + \int_0^R (V + V_{iZ}(x,Lwl))2\pi x dx \cdot \qquad (5.3)$$

Note, that *Lwl* is the length of the winglet. From Equations (5.1) and (5.2) we can integrate the power production for the actuator cap

$$P_{AC} = \rho\Gamma\Omega\left(\int_0^R \left(V + V_{iZ}(x,0)\right)xdx - \int_0^{Lwl} V_{iX}(R,z)Rdz\right), \tag{5.4}$$

which after insertion of the result from Equation (5.3) yields

$$P_{AC} = \rho\Gamma\Omega\left(\int_0^R \left(V + V_{iZ}(x,Lwl)\right)xdx\right) \tag{5.5}$$

However, since axial and radial induction stems from the outer wake tube only, this is seen to be identical to the power production for the ordinary actuator disc without winglets

$$P_{AC} = P_{AD}\,. \tag{5.6}$$

In absence of tip effects there is no effect of winglets on power production. Therefore, the role of winglets is to help reduce tip-loss.

The arguments leading to the above result are equally valid for downstream as well as upstream winglets. The increase or decrease of power production on the main wing is exactly balanced out by the power consumption or production on the winglet. This means, that in the absence of tip effects, adding winglets does in fact not increase power production. This tells us that what winglets can help us do on wind turbine wings is to reduce tip effects, known in the Blade Element Momentum frame of reference as tip loss. So in real life, the positive effect of a winglet has to come from a higher reduction of tip-effects than the increase in viscous drag from the winglet. So, according to the present work, the (global) Betz limit should still be the absolute upper limit for *Cp*.

In fact, taking a Trefftz-plane approach [17] with the mass conservation and energy equations, the result is that the power production of anything inside the cylindrical control volume extending from far upstream to far downstream is given by the velocity profile of what flows out of the control volume. Since the only axial and radial induction comes from the wake itself, any uniformly loaded actuator cap shape ending at the same radial position will lead to the same velocity profile in the far wake, and will thus have identical productions.

So how does this result compare with classic non-rotating theory? In the actuator cap analysis, we have an infinite number of blades, which cancels out tip effects. An infinite number of blades in the rotating case corresponds to an infinite aspect ratio, for which induced drag is zero. Induced drag in the non-rotating case is the equivalent to tip-loss in the rotating case, so it would seem that there are more similarities between the rotating and non-rotating cases than was apparent at first sight.

Comparison with previous works

The explanation of what winglets do is in direct disagreement with an earlier work on the matter

As mentioned in the introduction, the result that in absence of tip effects, there is no effect on power production by use of winglets, is in direct contradiction to the findings of Van Bussel [9], which to the authors' knowledge is the only previous work to be offering an insight into the physical understanding of winglets on wind turbine rotors. Van Bussel, based on his momentum theory analysis of the problem, concluded that the power augmentation by use of downwind winglets is due to the downwind shift of the wake vorticity. This had the implications that the maximum obtainable power coefficient for a complete transfer of the load on the main wing to the winglet was found to be an increasing function of the downwind extension of the winglet, $Cpmax=16/27*f(Lwl/R)$, where $f(-\infty)=0.5$, $f(0)=1.0$, $f(0.1)=1.1$, $f(1)=3.4$, and $f(\infty)=\infty$, the upper (un)limiting value clearly being unphysical, and the result, that upwind winglets decrease production being in disagreement with the latter CFD investigations by Johansen[11-12].

In order to investigate where the mismatch between the results of the present work and the work of Van Bussel comes from, a different approach was taken. Consider the integration of the power production part from only the main rotor of the actuator cap in Equation (5.4)

$$P_{AC,Main} = \rho\Gamma\Omega\int_0^R \left(V + V_{iZ}(x,0)\right)xdx \tag{5.7}$$

If the axial velocity at the main rotor is approximated by the center-line value from the semi-infinite tangential vorticity cylinder from Wilson [18] used in Van Bussel's work, we arrive at the following result

$$P_{AC,Main} = 0.5\rho\Gamma\Omega R^2 V\left(1-(1-\frac{Lwl/R}{\sqrt{1+(Lwl/R)^2}})a\right), \tag{5.8}$$

where a signifies the axial induction factor at the plane through the winglet tips. If the relation between the thrust coefficient and the circulation derived in Øye's work (neglecting tangential induction)

$$\Gamma\Omega \cong C_T \pi V^2, \tag{5.9}$$

is used with the expression for the thrust coefficient in Van Bussel's work (referred to as the axial drag coefficient of the rotor in that work)

$$C_T = 4\left(1-\left(1-\frac{Lwl/R}{\sqrt{1+(Lwl/R)^2}}\right)a\right)a, \tag{5.10}$$

in Equation (5.8), and the definition of the power coefficient is employed, we arrive at the power coefficient from the main rotor

$$C_{P,AC,Main} = 4a\left(1-(1-\frac{Lwl/R}{\sqrt{1+(Lwl/R)^2}})a\right)^2, \tag{5.11}$$

It is shown that the power production part of the winglet itself was not included in the previous work.

which is exactly the result predicted by Van Bussel's work, indicating that the power production part of the winglets themselves were not included in that work.

Based on these considerations, we find the results of that model to be erroneous, as likewise the explanation of the power augmentation by use of downwind winglets is due to the downwind shift of the wake vorticity.

The result just mentioned in the present section is supported by the actuator disc results of Aagaard *et al.* [19], who concluded, that for uniformly loaded rotors, the induced velocities in the plane through the rotor tips are independent of the shape of the rotor in absence of tip effects.

5.4 Free-Wake Lifting Line (FWLL) algorithm

The newly developed Free Wake Lifting Line code is described here.

Now that the analysis using the simpler models have indicated that the effect of winglets is to reduce tip effects, we need to employ a model capable of modeling such effects if we are to estimate the maximum power production obtainable with winglets.

For this task a Free-Wake Lifting Line (FWLL) method was developed. The reason for this is that such a method is better suited to find the optimal loading for a given rotor geometry (winglet) using numerical optimization than a vortex lattice panel code or CFD, since for these codes, the load can be changed both by changing chord distribution and changing the twist distribution.

In the new Free-Wake Lifting Line method, the wings are represented by concentrated line vortices, from which shed vorticity emanates into the wake. The method does not take into consideration the actual local geometry of the wing cross-section (airfoil shape), but models only the effect of the circulations that the airfoils generate. This makes this method well suited for investigation of mechanisms and optimization of aerodynamic loads. The inviscid lift forces from the fluid on the wings are evaluated from the Kutta-Joukowski Theorem, $\underline{L}=(\Delta x\ \rho)\underline{V}_{rel}\times\underline{\Gamma}$, using the relative velocity of the flow with respect to the wings, including also the contributions from the free wakes of the wings. Since viscous effects are not naturally a part of a lifting line algorithm, they are taken into account separately. The local drag forces act in the direction of the relative flow direction, and the magnitudes are obtained from the lift forces using 2D lift-to-drag ratios of the airfoils.

A new algorithm for evaluating the "induced forces" from the velocities that the non-planar bound vorticity induces on itself was formulated. In order to avoid the lifting line singularity on itself, this "extra" induced velocity is computed using a vortex-lattice type grid. The self induced velocities are obtained using an iterative scheme using a weighted difference between 3D and 2D self-induced velocities. From the converged self-induced velocity, the induced forces are computed using the lifting line. The self-induced forces in the case of winglets straight up- or down-wind produces negligible changes in power production. A non-negligible effect on power production from this term is only seen in cases where the winglets have sweep, i.e. where the winglets are tilted 'forward' or 'backward' (a *Y* component of the winglet on the vertical wing in Figure 5-1). Since the winglets considered in the present work have no sweep, the self-induced effect will not be discussed further.

In order to determine the shape of the free wake, a steady-state free wake method was adopted. Due to the inherent unstable nature of free wake methods for wind turbine applications, some care must be taken to obtain converging solutions. Since the free-stream velocity is constant, and the turbine is assumed not to be operating in yawed conditions, only the vortices from one wing need be updated; the other ones are obtained from symmetry conditions. In order to ensure adequate resolution of the wake, the position of the wake is determined in specific planes parallel to the rotor plane, with narrow spacing near the rotor plane and increased spacing further down the wake (ΔZ=0.005R at the rotor disc and ΔZ=0.018R at Z=3R using 224 cross-sections). In the first part of the wake (up to 3R), the wake is updated freely, and the wake velocities are evaluated at the intersection between the linear vortex elements. In the second part of the wake, the vortex strings keep constant radial distance to the rotational axis, and the azimuthal positions are obtained from extrapolation of the values at the end of the free wake zone. The last zone is a semi-infinite vortex tube to model the effect of the far wake. The positions of the free wake are updated for one cross-section at the time, and the differences in radial and azimuthal positions are convected to all downstream coordinates of the wake after updating all positions at that specific axial position. In order to avoid stability problems with the free wake method, the cross-sections are not updated in the typically parabolic marching fashion, but according to a scheme that ensures that the update cross-section position varies as much as possible in space while still covering all cross-sections in the free wake domain during a single global iteration. This scheme is an adoption of the integer sequence A049773 in the on-line encyclopedia of integer sequences [20]. Furthermore, relaxation is employed to facilitate a more stable numerical behavior. The relaxation coefficient used for the present computations was set

to 0.6. The wake vorticity is modeled by rectilinear vortices with a viscous Rankine vortex core: 0.01R at rotor disc going toward 0.05R exponentially with a half-distance of 2R. The results shown in this work were all obtained with the bound vorticity along the wings discretized in 40 elements, with finer resolution towards root and tip where gradients are steeper. Investigations of the discretization have shown that the present setup produces results that change only marginally by further increasing resolution.

The integral forces and dimensionless numbers are obtained from integration of the total distributed forces.

In order to maximize *Cp* values, Nelder-Mead simplex optimization was used in combination with a 3rd order cubic spline representation of the bound circulation to reduce the number of optimization variables.

A validation of the main part of the code is found in Johansen[21], where comparison of a priori results obtained with the current code and an actuator disc code is made with results from the full 3D CFD code EllipSys3D[22, 23, 24] on an aerodynamically most efficient rotor (*R*=63m, *TSR*=8, *Cl/Cd*=110 (corresponding to the Risø B1-15 airfoil at α=8°, which operates at Cl=1.4)). As is evident from Table 5-1 and Figure 5-3, the agreement between the 3D CFD results (black lines) and the present method (red lines) is excellent in the non-winglet case.

Results from the new code compares very well with CFD results for a case without winglets.

Table 5-1 Comparison of integral FWLL and 3D CFD results on the aerodynamically most efficient wind turbine without winglets. TSR=8, Cl/Cd=110.

	Cp	*Ct*
EllipSys3D	0.515	0.872
FWLL	0.514 (-0.2%)	0.868 (-0.5%)

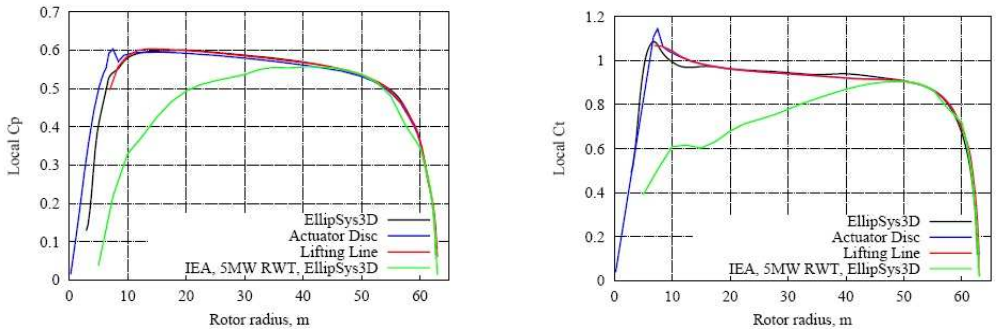

Figure 5-3 Comparison of local power and thrust coefficients obtained with the FWLL (red) and 3D CFD (black) codes on the aerodynamically maximum efficient wind turbine without winglets, from [21]. TSR=8, Cl/Cd=110.Left: Local Cp. Right: Local Ct.

5.5 Results from the FWLL algorithm

The results from the FWLL algorithm shown in this work are all based on turbulent 2D data from a Risø-B1-15 airfoil, for which the design point is at α=8°, resulting in Cl/Cd=110 and Cl=1.4. Furthermore a tip-speed ratio of *TSR*=8 is used throughout. The initial guess for the bound circulation is the circulation of the baseline non-wingletted optimal rotor investigated in [21]. It was found that the final converged solution for the optimal circulation was rather close to this value for the relatively small winglets investigated in this work.

Since the standard local *Cp* value is given by

$$C_p = \frac{\Delta P}{0.5\rho V_\infty^3 \Delta A} = \frac{\frac{\Delta F_Y}{\Delta r}\Omega N_B}{\pi\rho V_\infty^3}, \tag{5.12}$$

where $\Delta F_Y/\Delta r$ is the torque-generating component of the force per unit radial direction of one wing, the local *Cp* value at the end of a wingletted wing would be plus or minus infinity, since Δr is zero at the winglet. To circumvent this, a local pseudo *Cp* is obtained by replacing $\Delta F_Y/\Delta r$ with $\Delta F_Y/\Delta s$, where *s* denotes the direction along the span:

$$C_{p,pseudo} = \frac{\frac{\Delta F_Y}{\Delta s}\Omega N_B}{\pi\rho V_\infty^3}. \tag{5.13}$$

This way, the integral *Cp* is not obtained by a simple integration of the local value over radius, as is the case for the standard local *Cp*

$$C_P = \int C_p \cdot \left(\frac{r}{R}\right) d\left(\frac{r}{R}\right), \tag{5.14}$$

but slightly modified as

$$C_P = \int C_{p,pseudo} \cdot \left(\frac{r}{R}\right) d\left(\frac{s}{R}\right). \tag{5.15}$$

A local pseudo *Ct* value can be defined analogously. Figure 5-4 shows the local pseudo *Cp* and pseudo *Ct* values for an optimal rotor with a 2% downwind winglet.

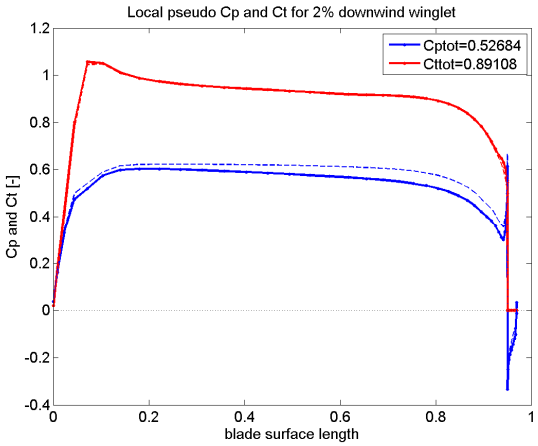

Figure 5-4 Local pseudo power coefficient (blue) and pseudo thrust coefficient (red) for the optimally loaded 2% downwind winglet rotor case. TSR=8, Cl/Cd=110.

The negative effect of viscous drag on Cp increases with radius.

Local pseudo *Ct* values are shown in red, where it is seen, that these increase from the tip region towards the root, with a maximum just above 1 close to surface length 0.1. This is in agreement with earlier works on root aerodynamics [25]. At the tip, it is noticed that the thrust from the winglet is practically zero, in agreement with the theoretical considerations in earlier sections. The dashed blue line shows the inviscid part of the local pseudo *Cp* contribution, where a comparison with the total local pseudo *Cp* (full blue line) reveals, as expected, that the effect of the viscous drag increases with radius. It is also noted, that power production on the winglet itself is in fact negative, in agreement with the earlier theoretical considerations.

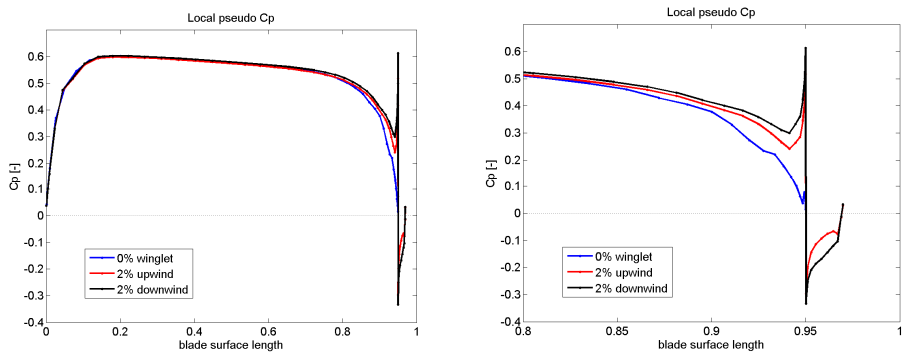

Figure 5-5:Left: Local pseudo Cp as function of non-dimensional wing surface length for 2% winglet cases upwind and downwind and without winglet. Right: Zoom-in on the tip-region. TSR=8, Cl/Cd=110

The trends seen in the optimal solutions corresponds well with the earlier theoretical considerations.

Figure 5-5 shows a comparison of local pseudo *Cp* values for optimal wings without winglet and with 2% up- and downwind winglets. It is seen, that power production is increased on the main part of the rotor for both winglet cases compared to the case without winglet. In agreement with the earlier considerations, the power production on the main wing is lower for the upwind winglet case than for the downwind one. Furthermore, it is noted, that power production on the winglet itself is higher for the upwind case, also in agreement with the theoretical considerations.

The computational results with winglets show that the obtainable increase in power by use of winglets is somewhat higher for a downwind winglet than for the corresponding upwind winglet length, Figure 5-6. The reason for this is not evident from the earlier theoretical considerations, but the trend is clear.

Downwind winglets increase Cp more than upwind winglets.

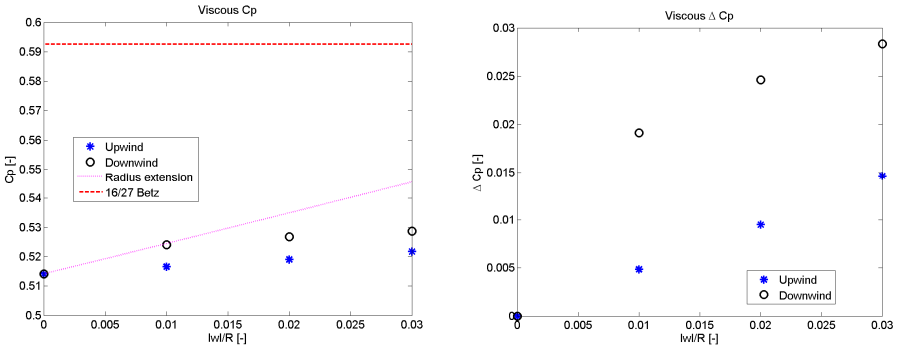

Figure 5-6:Left: Maximum Cp as function of winglet length. Right: fractional increase in Cp compared to the non-wingletted case. Downwind: Circles, Upwind: Stars, Magenta curve: Radius extension, Dashed red line: Betz limit. TSR=8, Cl/Cd=110

The power increase for the investigated cases is smaller than what is obtainable by a radial extension of the blades. However, small downwind winglets come close to this limit.

Furthermore, the computations show that increasing the length of the winglets decreases the fraction of power available with the winglet compared to the same increase in tip radius. An interesting result from the computations is that for relatively small winglets compared to the tip radius (~0.01), the increase in power corresponds to what could be obtained by increasing the length of the plane wing with the length of the winglet. Figure 5-7 shows the corresponding increases in thrust coefficient for the simulated cases.

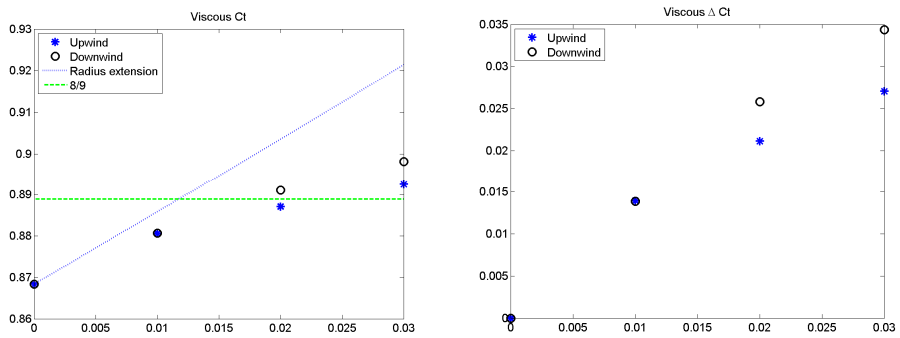

Figure 5-7: Left: Ct as function of winglet length for the cases shown in Figure 5-6. Right: fractional increase in Ct compared to the non-wingletted case. Downwind: Circles, Upwind: Stars, Gray curve: Radius extension, Dashed green line: 8/9. TSR=8, Cl/Cd=110

As seen, the increase in *Ct* is of the same order as the increase in *Cp*. The difference between upwind and downwind configurations is greater for *Cp* than for *Ct*, so based on these results, a downwind winglet is preferable over the upwind one.

Computations with changes in the geometry of the junction between the main wing and the winglet were performed. Computations with 0% (a kink), a 25% and a 50% bend radius/Lwl were performed for the 2% downwind winglet case. No significant difference between the 0% and the 25% cases were found, and only a slightly lower *Cp* was found for the 50% bend case.

5.6 Comparison with CFD results

A rotor was designed from the FWLL code results, and CFD computations were made using EllipSys3D

In order to finally assess the performance of the FWLL code results, a rotor was designed from the found optimal case. This can be done because both the bound circulation and the velocity field are known from the computations. The wing was laid out using 2D data from the Risø-B1-15 airfoil, as described previously.

The Navier-Stokes (NS) solver, EllipSys3D is used for the full 3D CFD computations. The code is developed by Michelsen[22-23], and Sørensen[24] and is a multiblock finite volume discretization of the incompressible Reynolds-averaged Navier-Stokes equations in general curvilinear coordinates. The code uses a collocated variable arrangement, and Rhie/Chow interpolation is used to avoid odd/even pressure decoupling. As the code solves the incompressible flow equations, no equation of state exists for the pressure and the SIMPLE algorithm is used to enforce the pressure/velocity coupling. The EllipSys3D code is parallelized with MPI for executions on distributed memory machines, using a non-overlapping domain decomposition technique. Solution of the momentum equations is obtained using a third order quadratic upwind interpolation scheme (QUICK) for the convective terms. All computations are performed assuming steady state conditions with a moving mesh technique based on analytical prescribed rotation[26]. The turbulent eddy viscosity is modeled using the k-ω SST[27]. The surface mesh is generated using Gridgen; a commercial mesh generator developed by Pointwise, Inc. and consists of 108 blocks of 32^2 cells for the entire rotor. The volume mesh is generated using Risøs in-house grid generator HypGrid[28] and away from the surface 128 cells are used resulting in $14.2 \cdot 10^6$ cells in total. The grid density used is based on more than 10 years of experience in rotor computations. The outer boundary of the computational domain is placed approximately six rotor diameters away. On the entire surface of the rotor

geometry no-slip boundary conditions are used. On the outer boundary of the computational domain inflow velocity is assumed constant with zero shear and a low turbulence intensity, while zero axial gradient is enforced at the outlet.

Figure 5-8 shows streamlines, surface pressures and iso-vorticity contours of the CFD computations.

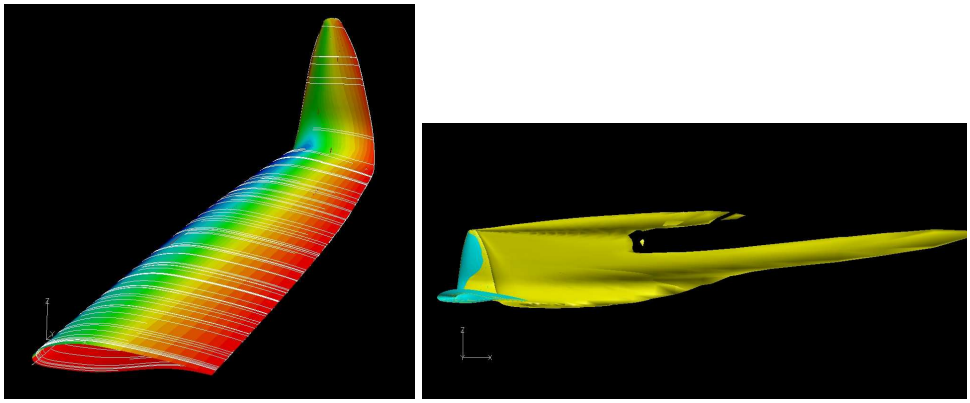

Figure 5-8: Left: Streamlines and surface pressure plot on the outer part of the wing. Right: iso-vorticity contours.

From Figure 5-8 it is seen that there is no separation of spanwise flow patterns, indicating 2D flow over the wing at all positions. The coloured surface in the left hand side figure signifies surface pressure. The blue color is low pressure, and red is high. The wing was designed to operate at "2D" angles of attack at α=8° on the whole rotor, which is the design point of the airfoil used in the computations. The surface pressure plot reveals that there is a lower pressure at the suction peak of the outer part of the main wing than on the winglet. This is surprising, since the relative velocity in the region near the tip is fairly constant, and should therefore translate itself into constant suction peak values. This is because the values of the pressure coefficient should only depend on the angle of attack for a given airfoil.

$$C_P = \frac{p - p_\infty}{\frac{1}{2}\rho V_{rel}^2} \approx \frac{p - p_\infty}{\frac{1}{2}\rho (V_\infty TSR)^2} = \frac{p - p_\infty}{K} \tag{5.16}$$

The loading in the CFD computation was not as expected from the FWLL code.

This indicates that the tip is too lightly loaded. This is also seen on the iso-vorticity contour, where it is evident that more vorticity is shed from the intersection between main wing and winglet than any other place on the outer part of the wing. This does not agree with the bound circulation distribution used to design the wing. It is not clear to the authors whether this is due to effects of the chord near the tip, or if the radial flow is predicted differently in the FWLL and CFD codes. That investigation is an ongoing work. It is noted, however, that apart from the apparent change in pressure contours at the bend, the pressure contours and the length of the iso-vorticity surface are continuous. Computations will be run with different offset in "winglet pitch" to attempt to obtain a smooth loading along the entire wing.

Table 5-2 Comparison of integral FWLL and 3D CFD results on the aerodynamically maximum efficient wind turbine with 2% winglets. TSR=8, Cl/Cd=110.

	$\Delta Cp/Cpref$	$\Delta Ct/Ctref$
FWLL	2.47%	2.61%
EllipSys3D	1.74%	2.80%

Due to the issues brought up earlier, the predicted results differ somewhat between the CFD and the FWLL results.

Table 5-2 shows the increase in *Cp* and *Ct* predicted with the CFD and FWLL codes. Note however, that due to the unresolved issues brought up previously, the bound circulation distributions are not identical in the two cases. It is suspected that a better agreement of the loading of the blade with the one predicted with the FWLL code will increase the $\Delta Cp/Cpref$ of the EllipSys3D computation closer to what is predicted by the FWLL code.

5.7 Conclusions and outlook

A summary of the main findings of this work is given below

- Yes, winglets can be used successfully to increase *Cp*
- The positive effect of winglets on power production is due to a reduction of tip losses, and is not connected with a downwind shift of wake vorticity.
- A new free wake lifting line code was developed, and comparisons with CFD computations on an optimal non-wingletted blade showed remarkable agreement between results.
- Results from the new code indicate, that:
    - Downwind winglets are more effective than upwind ones of the same length
    - The increase in power using winglets is smaller than what may be obtained by extending the wing radially with the same length
    - However, for small winglets (<2%), we get close to the same increase as for a corresponding increase in radius using downwind winglets
    - The results are not very dependent on the radius of the bend between the main wing and the winglet, but increases slightly for bend radii above 25% of the winglet height for the 2% downwind winglet case investigated
- A blade with 2% downwind winglet was constructed to obtain the same bound circulation as in the FWLL case. The blade was analyzed using the CFD code EllipSys3D:
    - The bound circulation in the CFD results is not in agreement with what was expected.
        - The reason for this is presently unknown to the authors.
        - Due to this, the predicted increase in *Cp* is lower for the CFD results than predicted with the FWLL code.
- Future work is needed to:
    - Explain what causes the difference in the CFD and FWLL predictions

- Obtain a better estimate of the maximum power increase by use of winglets using CFD for a wing geometry that produces the predicted bound circulation distribution
- Be able to run the FWLL code using 2D profile input data

5.8 References

[1] Kroo I. "Drag due to lift: Concepts for prediction and reduction", Annu. Rev. Fluid Mech. 2001. 33:587–617

[2] Munk M. "The Minimum Induced Drag of Aerofoils" NACA Report 121, 1923

[3] Whitcomb RT. "A design approach and selected wind tunnel results at high subsonic speeds for wing-tip mounted winglets". NASA TN D-8260. Natl. Aeronaut. Space Admin., Washington, DC. 1976.

[4] Jones RT. Jones RT, Lasinski TA. 1980. "Effect of winglets on the induced drag of ideal wing shapes". NASA TM 81230, Natl. Aeronaut. Space Admin. Ames Res. Cent., Moffett Field, Calif.

[5] Eppler R. "Induced Drag and Winglets" Aerospace Science and Technology, 1, p.3-15, 1997

[6] Maughmer M.D. "The Design of Winglets for High-Performance Sailplanes" AIAA paper 2001-2406

[7] Van Holten Th. "Concentrator systems for Wind Energy, with emphasis on Tip-vanes", Wind Engineering Vol.5, No.1, 1981

[8] Shimizu, Y et al. "Studies on horizontal axis wind turbines with tip attachments". EWEC '90 Conference proceedings, Madrid, Spain, September 10-14 1990, pp. 279-283, Ass, Bedford, U.K., 1990

[9] Van Bussel, G.J.W. "A momentum theory for winglets on horizontal axis wind turbine rotors and some comparison with experiments" Fourth IEA Symposium on the Aerodynamics of Wind Turbines, November 1990, Rome, Italy, Proc. edt. K.McAnulty, ETSU-N-118, Harwell, Didcot, U.K., January 1991

[10] Imamura, H. et al Numerical Analysis of the Horizontal Axis Wind Turbine with Winglets, JSME International Journal, Series B vol. 41 nr. 1, Feb 1998 JSME Tokyo Japan pp 170-176

[11] Johansen, J.; Sørensen, N.N.; Aagaard Madsen, H.; Wen Zhong Shen; Okulov, V. "Advanced rotor aerodynamics - including tip and root aerodynamics". In: Bak, C. (ed.), Risø National Laboratory (DK). Wind Energy Department. Research in aeroelasticity EFP-2005. Risø-R-1559(EN) p. 11-17

[12] Johansen, J. and Sørensen, N.N. "Numerical Analysis of Winglets on Wind Turbine Blades using CFD", EWEC 2007 Conference proceedings, Madrid, Spain

[13] Müller R.H.G & Staufenbiel R "The Influence of Winglets on Rotor Aerodynamics" Vertica Vol. 11, No. 4, p.601-618. 1987

[14] Müller R.H.G "Winglets on Rotor Blades in Forward Flight – a Theoretical and Experimental Investigation" Vertica Vol. 14, No. 1, p.31-46, 1990

[15] Goldstein, S., "On the Vortex Theory of Screw Propellers", Proc. of the Royal Society (A) 123, 440, 1929

[16] Øye S.,"A simple Vortex Model – using vortex rings to calculate the relation between thrust and induced velocity at the rotor disc of a wind turbine", In Proc. of the third IEA Symposium on the Aerodynamics of Wind Turbines, ETSU, Harwell, 1990, p.4.1-5.15

[17] Katz, J and Plotkin, A. "Low-Speed Aerodynamics: From Wing Theory to Panel Methods", McGraw-Hill.

[18] Wilson R.E., "Wind turbine flow field model"; Trans. ASME, Vol. 108, Nov. 1986, pp. 344-345

[19] Aagaard Madsen, H.; Rasmussen, F., The influence on energy conversion and induction from large blade deflections. In: Wind energy for the next millennium. Proceedings. 1999 European wind energy conference (EWEC '99), Nice (FR), 1-5 Mar 1999. Petersen, E.L.; Hjuler Jensen, P.; Rave, K.; Helm, P.; Ehmann, H. (eds.), (James and James Science Publishers, London, 1999) p. 138-141

[20] The On-Line Encyclopedia of Integer Sequences. http://www.research.att.com/~njas/sequences/A049773

[21] Johansen, J.; Madsen, H.Aa.M; Gaunaa, M; Bak, C & Sørensen N.N. "3D Navier-Stokes Simulations of a rotor designed for Maximum Aerodynamic Efficiency". AIAA-2007-217, presented Jan 2007 at Reno

[22] Michelsen J.A. "Basis3D - a Platform for Development of Multiblock PDE Solvers." Technical Report AFM 92-05, Technical University of Denmark, 1992

[23] Michelsen J.A. "Block structured Multigrid solution of 2D and 3D elliptic PDE's." Technical Report AFM 94-06, Technical University of Denmark, 1994

[24] Sørensen N.N. "General Purpose Flow Solver Applied to Flow over Hills." Risø-R-827-(EN), Risø National Laboratory, Roskilde, Denmark, June 1995

[25] Aagaard Madsen, H.; Mikkelsen R.; Johansen, J.; Bak, C.; Øye, S.; Sørensen, N.N. "Inboard rotor/blade aerodynamics and its influence on blade design". In: Bak, C. (ed.), Risø National Laboratory (DK). Wind Energy Department. Research in aeroelasticity EFP-2005. Risø-R-1559(EN) p. 19-39

[26] Sørensen, N.N., "Rotor computations using a 'Steady State' moving mesh", IEA Joint Action Committee on aerodynamics, Annex XI and 20. Aero experts meeting, Pamplona (ES), 25-26 May 2005

[27] Menter F.R. "Zonal Two Equation k-ω Turbulence Models for Aerodynamic Flows". AIAA-93-2906, 1993

[28] Sørensen N.N. "HypGrid2D a 2-D mesh generator", Risø-R-1035(EN), Risø National Laboratory, Roskilde, Denmark, 1998

6 Edgewise vibrations in stand still

Thomas Buhl

The subject of vibrations in stand still situations has been investigated earlier in the EFP2002 project [1]. There are many encounters of edgewise vibrations in stand still in numerical calculations; however, no records of vibrations on real life turbines have been reported. It is not possible to investigate how far the real turbines are from these instabilities before measurements can clarify how large the effects of the crude assumptions in the numerical calculations are. Whether the problem is purely numerical due to poor modeling, or a real life problem, we will not discuss here. We will merely state the fact that in some numerical calculations, herein some certification calculations, unstable edgewise vibrations in standstill occur. These edgewise vibrations will be investigated in this chapter.

The calculations in this chapter are all done in HAWC2, the multibody aeroservoelastic code with BEM aerodynamics developed at Risø. The code includes all standard BEM model corrections and models like tip loss, Betz correction, induction (BEM), dynamic stall etc. The Betz correction is a model that changes the lift force when skewed inflow along the span is present. Due to the crude assumptions made in this model, it has its limitations and cannot correct cases where for example the inflow is extremely skew, where three-dimensional effects due to for instance twist and taper are present.

This chapter investigates only the phenomenological aspects of the edgewise vibrations under stand still conditions. Therefore, no shear is present in the following calculation and the induction from the BEM model is set to zero. This chapter is divided up into subsections covering: a short discussion of the airfoil data; the damping of a blade and the full rotor; the influence of dynamic stall; comparison to 2D quasi-stationary calculations; and finally a few suggestions as to how to eliminate the vibrations.

In the EFP2002 project the focus was mainly focused on mapping the azimuth and yaw angles for which negative damping was present for a stiff turbine with one soft blade. Here, we expand the investigations to cover more degrees of freedom and different model dependencies.

6.1 Airfoil data

The numerical calculations in the following chapter are based on the airfoil data presented in the following subsection. Most airfoil data are valid for a small range of angles of attack (AOA). The airfoil data in the deep stall regions (fully separated flow) are estimated. Furthermore, the aeroelastic code HAWC2 (as well as all know aeroelastic codes) does not include a deep stall model yet. As illustrated in the EFP2002 project [1] the damping of a blade or a rotor is highly dependent on small changes in the profile data in the regions of negative damping. The result in the mentioned work showed that the negatively damped vibration could be completely removed by changing the airfoil data slightly in certain AOA regions. We are not going to perform this exercise here, however, we will emphasize that the damping characteristics in the computations could be completely changed by changing the airfoil data slightly. In the following, we assume that the airfoil data shown in Figure 6-1 are correct in all regions of AOA.

The airfoil data used in the analysis

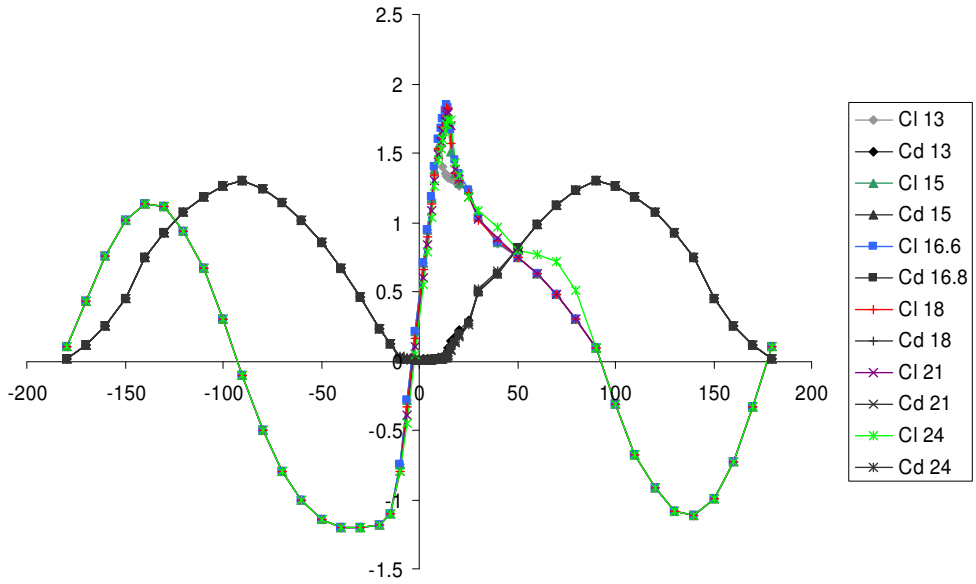

Figure 6-1 Airfoil data. C_L and C_D for profile thickness from 13 to 24%.

6.2 Damping of the blade and rotor

In this section the damping of the blade and the full rotor is calculated. The first and simplest case is where the turbine is stiff where only blade 1 is soft and pointing upwards as seen in Figure 6-2. The calculations are performed at 50 m/s resulting in time series with increasing wind from 0 to 50 m/s during the first 20 seconds. Hereafter, a force in the edgewise direction excites the edgewise vibrations for 10 seconds with a frequency of 1 Hz, which is close to the natural frequency of the 1st edgewise mode for this turbine. After the 10 seconds excitation, the edgewise vibrations are examined and the damping is calculated for the given AOA, which is found at 75% radius. In Figure 6-3, a time series is shown for the displacement in the edgewise direction. This is shown simply to illustrate the time series with the initialization from 0s to 20 s, excitation from 20s to 30s, and the free simulation from 30s to 100 s.

In the following results, the dynamic stall model is enabled if nothing else is mentioned.

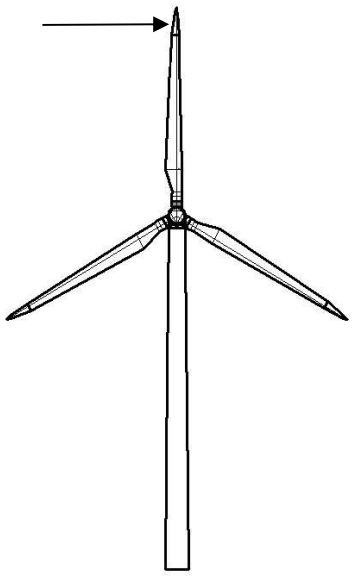

Figure 6-2 Schematic layout of the test cases with exciter force.

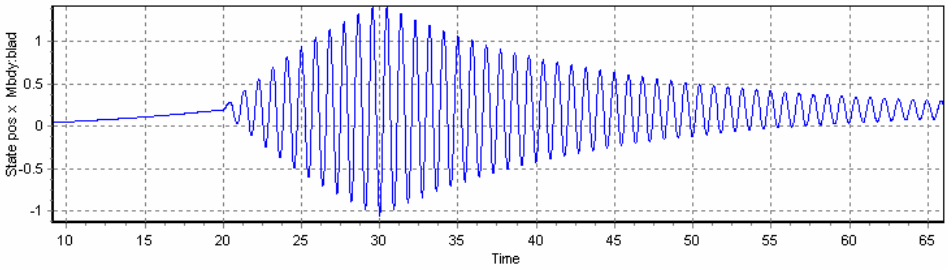

Standard time series; increasing wind, excitation, free turbine

Figure 6-3 A time series of the edgewise vibrations where the excitation can be seen from 20 to 30 seconds and the damping can be calculated from the time series after t=30 seconds.

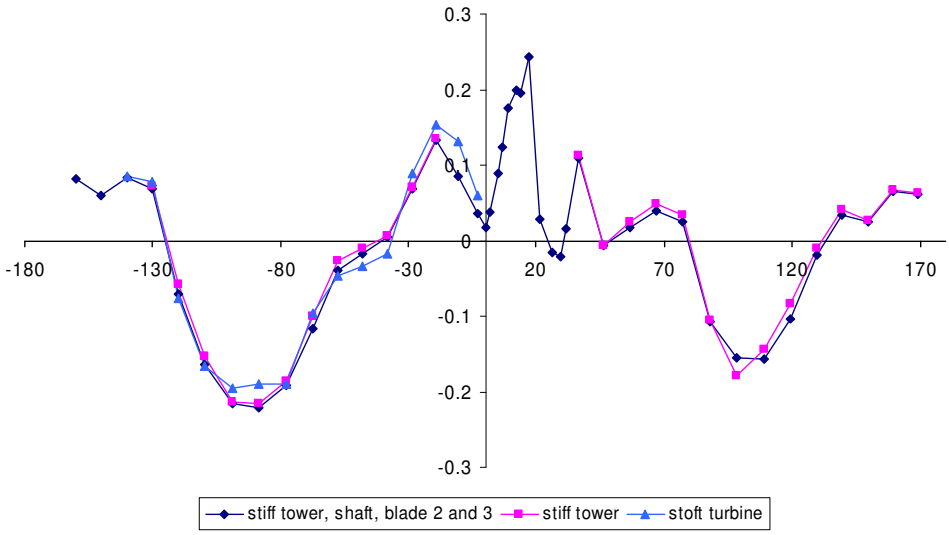

Figure 6-4 The damping given in logarithmic decrement as a function of the AOA for the simplest case where only blade 1 is soft (in dark blue), for the soft rotor and stiff tower (in purple) and for the soft turbine (in light blue). It can be seen that there are two major critical areas from +80 to 130 degrees and from -40 to -120 degrees. Furthermore, it can be seen that there are no major differences between the three cases.

In Figure 6-4 the damping (given in logarithmic decrement) of the edgewise vibrations is shown as a function of AOA for three different turbine configurations. The dark blue line shows the turbine with soft blade 1 and the rest stiff, the purple line shows the result for the soft rotor and shaft and stiff tower while the light blue line shows the soft turbine. In these calculations the change in AOA has been done by collectively pitching the blades resulting in the same AOA on all three blades. Hence, the results in Figure 6-4 are very similar and the small difference is possibly due to the precision of the numerical calculations. These results can provide us with a good indication of where the critical regions in AOA are for the isolated blade. However, in real life when a turbine is parked, the blades are pitched to e.g. 90 degrees and here the wind direction might change to critical AOA. In these situations the three blades will experience three different AOA and one blade might be in a critical region while the two others are not etc.

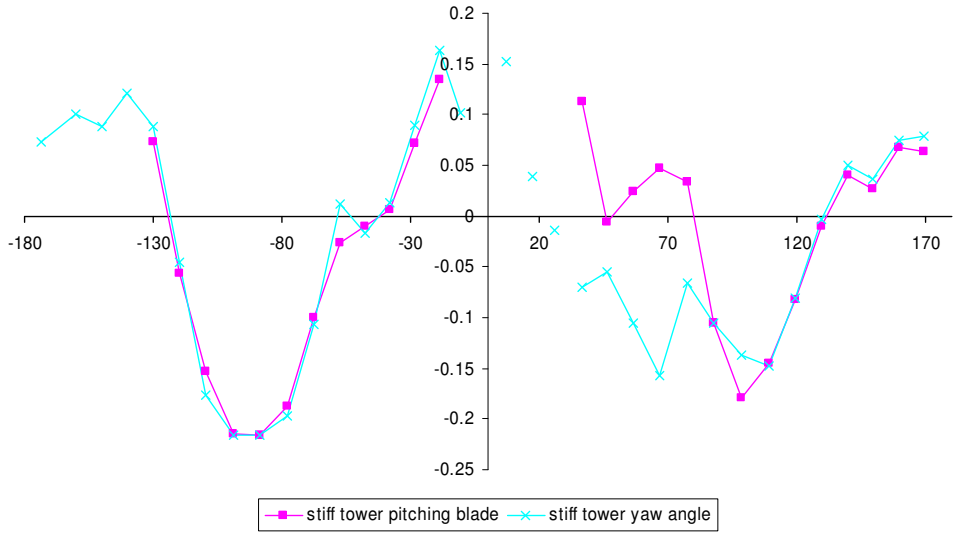

Figure 6-5 The purple line shows the damping as a function of AOA for blade 1 for the turbine where the blades are pitching to change the AOA (same AOA for all blades). The light blue line show the case where the blades are pitched to 90 degrees and the AOA changes come from changing the yaw angle (different AOA for the blades).

Two cases are investigated: Blade pitching and change in yaw inflow angle

In Figure 6-5 the damping is shown as a function of AOA for blade 1 for the case where the blades are pitched to change the AOA (purple line), and for the case where the rotor is parked with 90 degrees pitched blades and the yaw angle is varied to change the AOA (light blue line). In this case it is seen that one of the unstable regions has expanded. This is due to the coupling of the blades through the shaft. For the one case the rotor is positively damped at +70 degrees AOA because all the blades are in the positively damped region. However, in the other case only blade 1 is at +70 degree AOA while the two other blades are in a negatively damped region hence making the rotor negatively damped.

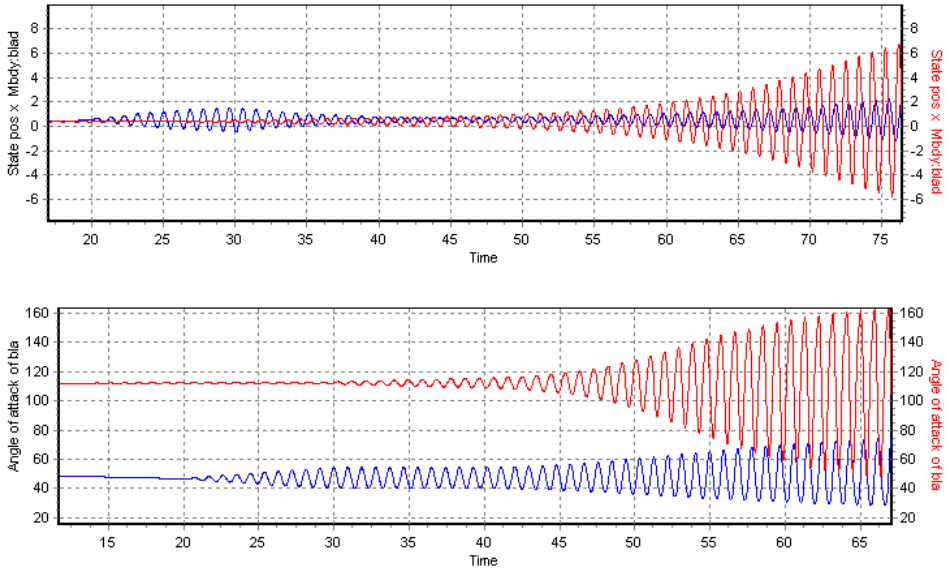

Figure 6-6 Upper plot: A time series is shown for the edgewise displacement for blade 1 (blue line) and blade 2 (red line). Lower plot: A time series of the AOA for blade 1 (blue line) and blade 2 (red line).

In Figure 6-6 two time series are shown where AOA is changed by yawing. The upper plot shows the edgewise tip displacement for blade 1 (blue line) and blade 2 (red line) while the lower plot shows the AOA of blade 1 (blue line) and blade 2 (red line). Concentrating on the upper plot the excitation from 20s to 30 seconds can be seen in blade 1 and this excites blade 2 (and of course blade 3) through the shaft. The vibration in blade 1 dies out after the excitation since the blade is in an AOA region with a positively damped edgewise vibration (the AOA is about 50 degrees). However, blade 2 has an AOA of about 110^{o} which is negatively damped for the isolated blade. Hence, the coupling though the shaft makes the complete rotor negatively damped for this yaw angle.

6.3 Damping with and without dynamic stall

As mentioned in the introduction to this chapter there is no dynamic model in HAWC2 for the deep stall region, which is the region where the flow is fully separated from the airfoil. Here the aerodynamic forces are found from static lift, drag and moment curves i.e. quasi-steady aerodynamics. In this subsection we look at how the damping level is influenced by dynamic stall in the computations. In Figure 6-7, the damping is shown for the isolated blade 1 as a function of AOA on blade 1 in 75% radius. The dark blue line shows the calculations with dynamic stall while the purple line shows the calculations without dynamic stall. The light blue line shows the difference between the two calculations and shows that the entire blade is fully separated from about +50 degrees AOA and upwards and from about -40 degrees AOA and downwards. The implemented dynamic stall model in HAWC2 has no effect on the calculation in deep stall because the separation point is used for modeling the dynamics of stall. It can be seen that the dynamic stall has a great influence on the damping level in the regions where it is active (from -40 to 50 degrees AOA). In general it can be concluded that dynamic stall mostly increases the damping level of the edgewise vibration except for a few points just before stall. This conclusion might lead us to think that a stall model for deep stall could give added damping of the edgewise vibrations.

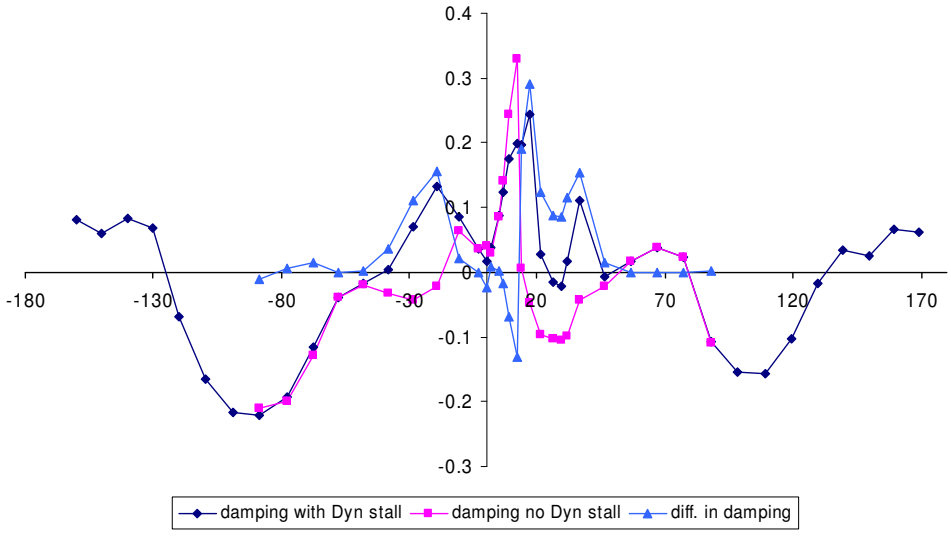

Figure 6-7 Damping shown as a function of AOA. The dark blue line shows the calculations with dynamic stall while the purple line is the calculation without dynamic stall. There is full separation on the entire blade is from about -40 and down and from 50 degrees and up.

Turbulence influence on damping

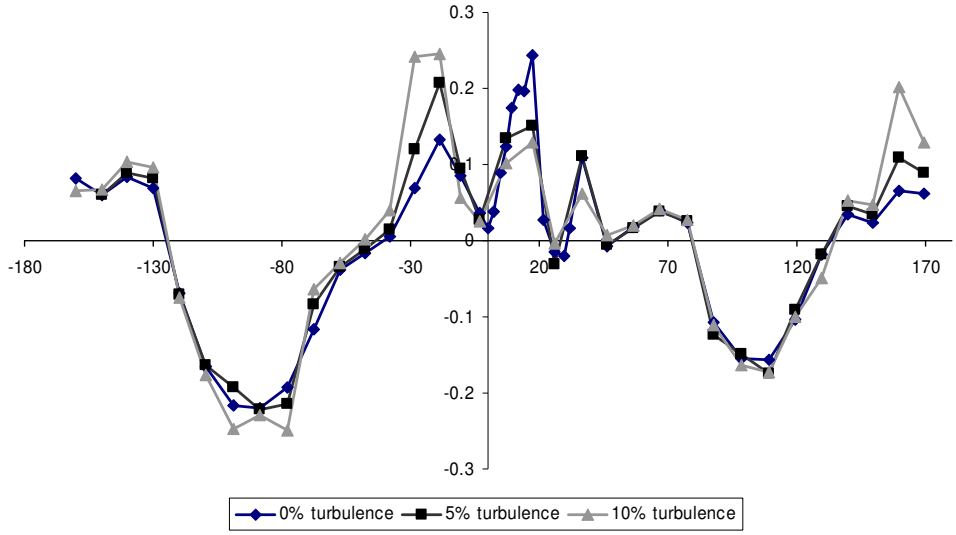

Figure 6-8 The influence of turbulence on damping. The turbine in all three cases has a stiff tower, shaft, blade 2 and blade 3. Blade 1 is pointing upwards and the blade is pitched from -180 to 180 degrees. The damping is showed as function of the AOA. The three cases are; dark blue line 0% turbulence, black line 5% turbulence and grey line 10% turbulence intensity factor.

To estimate the stochastic behavior of the forces in deep stall, a number of runs with turbulence were carried out. In Figure 6-8 the damping is shown as a function of the AOA for 0, 5 and 10% turbulence intensity. Only very small changes are seen and most of them are within the limit of the precision of the determination of the damping.

6.4 Comparison to 2D Quasi-stationary analysis

As in the EFP2002 report [1] we here make a comparison between the HAWC2 calculated damping values and 2D quasi-stationary calculations. It is actually comparing a 3D result with a number of profiles with a single profile in 2D, hence, is merely a comparison of trends.

From Figure 6-9 it can be seen that the qualitative results are comparable. So now we can investigate from where the negative damping arises by looking at the specific contributions in the simple 2D analysis. In Figure 6-10, aerodynamic damping is divided into the components of which the 2D quasi-stationary damping is composed. It is seen that the largest negatively damped component is due to the component from $C_L'(=dC_L/dAOA)$ and the largest positively damped component is due to the component from C_D.

3D HAWC2 calculations compared to 2D quasi-stationary results

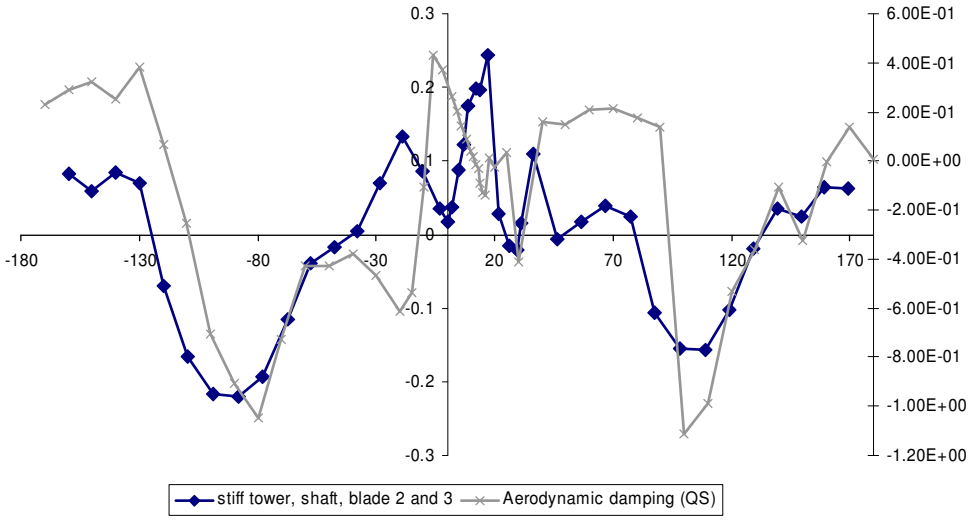

Figure 6-9 Comparison of a 3D HAWC2 calculation with 2D quasi-stationary (QS) result. There is an offset in y-axis due to structural damping in the HAWC2 calculations and since the QS results have been normalized with ½ρcV. The later is also the reason for the scale difference.

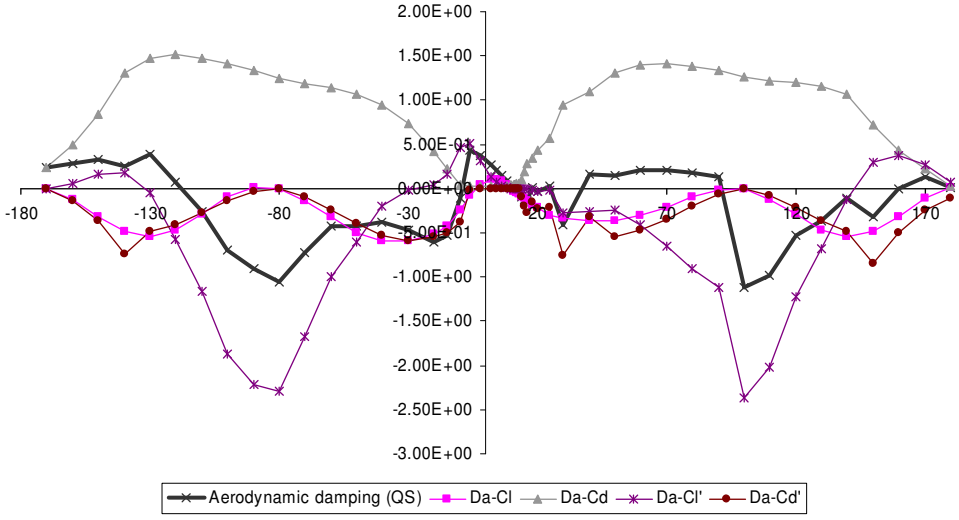

Figure 6-10 The contribution to the damping from the specific terms C_l, C_d, C_l' and C_d' in the 2D quasi-stationary analysis.

6.5 Alleviation of edgewise vibrations in stand still

There are a number of ways to circumvent edgewise vibrations depending on whether the problem is believed to be physical or of a purely numerical nature. If the problem is purely numerical, the models in the aeroelastic codes must be refined. This is continuously being done e.g. by implementing a dynamic deep stall model. The investigation in EFP2002 [1] were carried out using HAWC, which is based on a linear structural model, while the new code HAWC2 is based on a multibody formulation which inherently includes the nonlinear effects of large deflections. Additionally, a yaw slip bearing model and a gear box model are being implemented in HAWC2. Whether

these expansions of the code will alleviate the edgewise vibrations in the stand still situation can not be concluded yet.

If the problem is believed to have a real life counterpart, active control of e.g. pitch angle or yaw angle could be adopted. In Figure 6-11 and Figure 6-12 the yaw moment is shown as a function of AOA for the cases where the blades are pitched to obtain changes in AOA and where the turbine is yawed to obtain changes in AOA, respectively. It is seen that there is a large deviation from the mean yaw moment for the minimum and maximum moments in the regions where negatively damped edgewise vibrations are seen. This could be used in an active control of the turbine to avoid the critical AOA.

In Figure 6-13, the idling speed is showed as a function of the damping of blade 1 for an AOA of -110 degrees which is a critical AOA. This result is for the stiff turbine with only blade 1 soft. It is seen that idling speeds in the excess of 0.35 rad/s will result in a positively damped edgewise vibration for this specific AOA. However, idling in wind speeds of 50 m/s with 0.35 rad/s can cause other critical loads which need to be investigated.

The main concluding remark must be that measurements on a real blade or a real turbine are needed to further conclude this investigation.

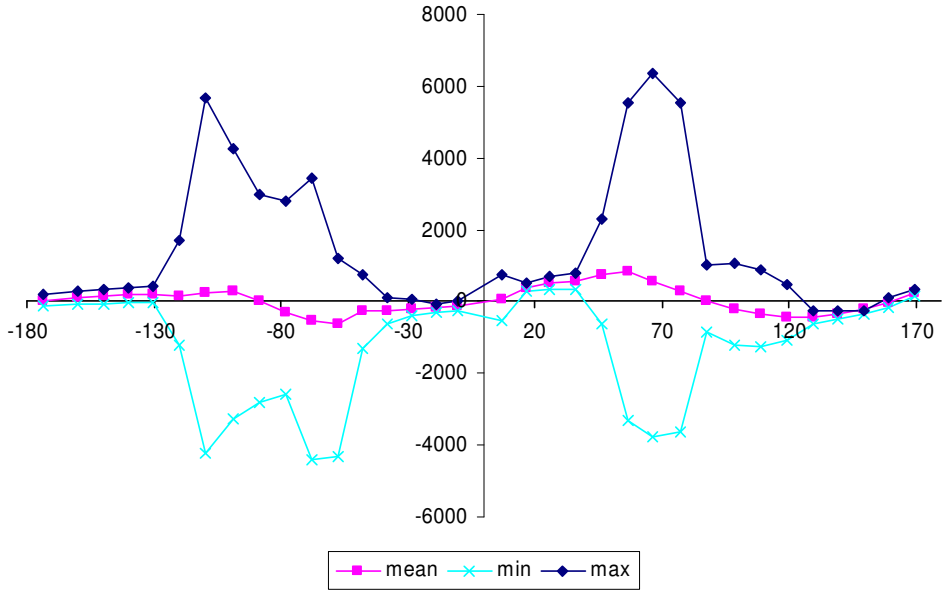

Figure 6-11 Yaw moment; mean, min and max moment for the case where the blade are pitched to change AOA.

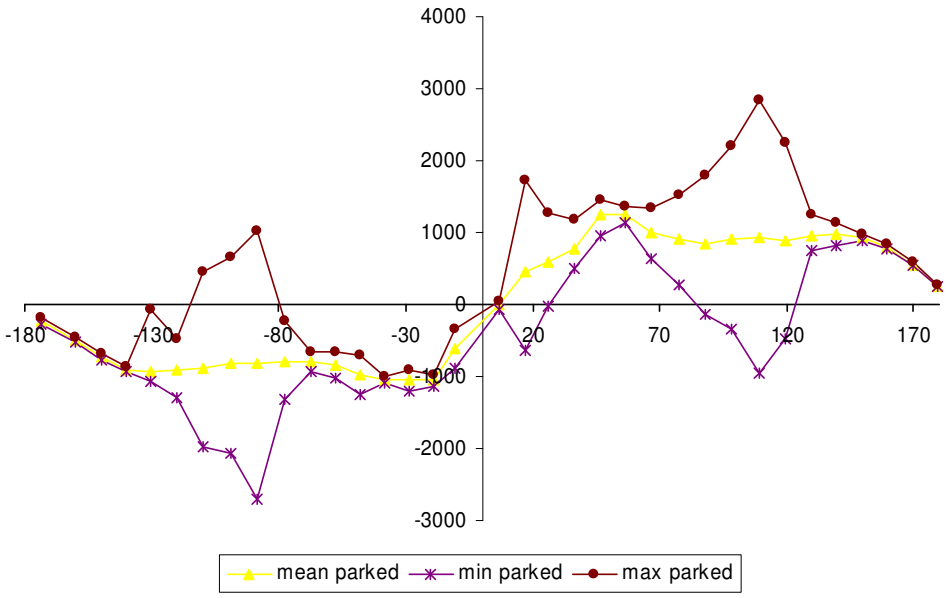

Figure 6-12 Yaw moment; mean, min and max moment for the parked rotor with blade pitch of 90 degrees and changing yaw angle to change AOA.

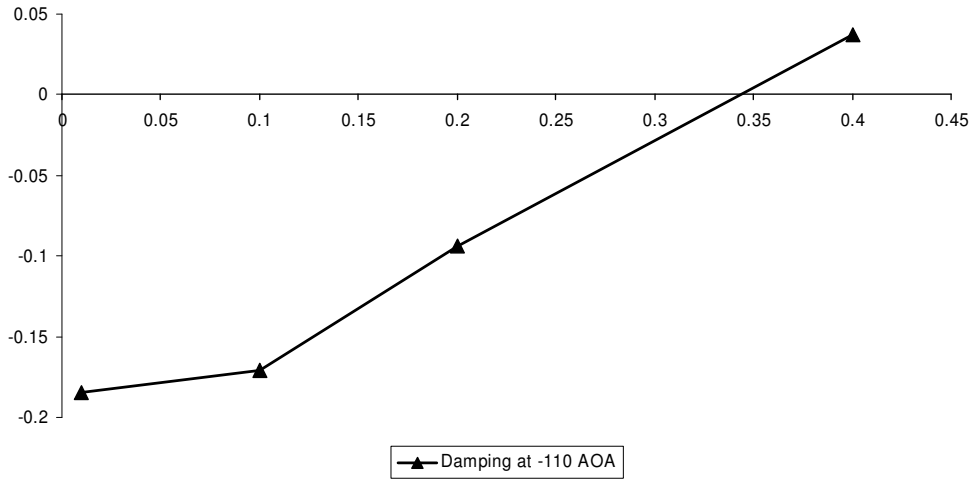

Figure 6-13 Idling speed in rad/s as a function of the damping for blade 1 at an AOA of -110 degrees is shown for a stiff turbine with blade 1 soft.

6.6 References

[1] Mac Gaunaa and Torben J. Larsen, 'Stilstandslaster', chapter in 'Forskning i Aeroelasticitet' 2002, ed. Christian Bak, Risø-R-1434(DA)

7 Dynamics of a hydraulic pitch system

Morten Hartvig Hansen and Bjarne Skovmose Kallesøe

This chapter deals with the modeling and analysis of the dynamics of a hydraulic pitch system for the 5 MW Reference Wind Turbine (RWT) by NREL [1]. It is shown that the compressibility of the hydraulic oil introduces a dynamic mode in the pitch bearing degree of freedom. This mode may obtain a negative damping if the proportional gain on the actuator position error is defined too large relative to the viscous forces in the hydraulic system and the total rotational inertia of the pitch bearing degree of freedom. A simple expression for the stability limit of this proportional gain is derived which can be directly used for tuning the gain based on the Ziegler-Nichols method.

A simple expression for gain tuning is derived

Computation of the transfer function from a harmonic pitch reference signal to the actual pitch response indicates that the hydraulic pitch system can be approximated as a low-pass filter with some appropriate limitations on pitching speed and acceleration. The structural model of the blade includes the geometrical coupling of edgewise bending and torsion for large flapwise deflections. This coupling is shown to introduce edgewise bending response of the blade for pitch reference oscillations around the natural frequency of the edgewise bending mode, in which frequency range the transfer function from reference to actual pitch angle cannot be modeled as a simple low-pass filter.

The actuator can be approximated by a 2nd order low-pass filter

The pitch bearing is assumed to be frictionless as a first crude approximation; modeling of pitch bearing friction is a current research topic of the authors.

Bearing friction is not included in this first study

7.1 Pitch actuator-blade model

This section deals with the hydraulic pitch actuator model and the structural blade model. In this first approach to analyze the dynamics of a pitch system, frictional and gravitational forces are neglected and only the static aerodynamic forces on the blade are included to obtain the correct static blade deflection and static aerodynamic pitch torque.

Hydraulic pitch actuator model

Figure 7-1 shows the geometry and hydraulic circuit of the modeled pitch system. The geometric parameters r_p, l_p, and L determine the relationships between pitch angle θ_p and the position of the piston in the cylinder $x_p = x_p(\theta_p)$ with $x_p = 0$ at the minimum pitch angle. The piston force F creates a pitch torque $T_p = F\, r_p\, g(\theta_p)$, where the function $g(\theta_p)$ is a force factor given by the derivative of $x_p(\theta_p)$ divided by the torque arm r_p.

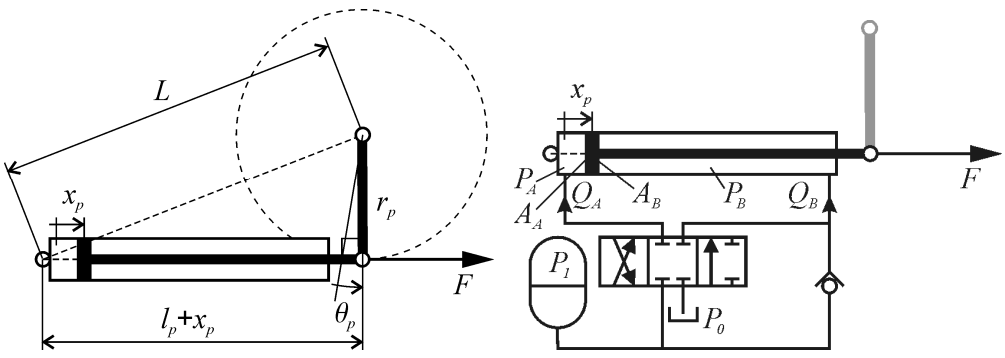

Figure 7-1: Geometry (left) and hydraulic circuit (right) of the modeled pitch system.

The piston rod length l_p and the torque arm r_p are chosen to be 2 m and 1 m, respectively, for the pitch actuator developed for the RWT. The minimum pitch angle is -5 degrees and the distance L = 2.3 m is chosen such that the maximum force factor g = 1 occurs at zero pitch angle θ_p = 0, where it is assumed that the maximum torque is required. Note that these geometric parameters are arbitrarily chosen, but are realistic values; in an actual design of the actuator they are part of the optimization process.

Figure 7-2 shows the cylinder position and force factor as function of the pitch angle in the range -5 to 90 degrees. In the normal operating range 0 – 23 degrees the force factor is not lower than 0.93 and the piston position depends almost linearily on the pitch angle.

The diagram of the hydraulic circuit in Figure 7-1 shows that the actuator is driven by an accumulator with an assumed constant pressure P_1. The cylinder pressures are denoted P_A on the left side (A-side) of the piston and P_B on the right side (B-side) of the piston, where the area A_B is smaller than the area A_A on the left side. The piston force therefore becomes $F = P_A A_A - P_B A_B - \eta\, dx_p/dt$, where the last term models the viscous damping force on the moving piston. The flows Q_A and Q_B to the two cylinder sides are governed by a proportional valve which is controlled by a piston position error feedback:

The actuator is controlled by a P-feedback of the piston position error

$$u = k_p\left(x_p(\theta_p) - x_p(\theta_{ref})\right)$$

where u is the control voltage to the valve, k_p is the proportional gain, and the position error is given as function of the actual and reference pitch θ_p and θ_{ref}, respectively.

A valve flow is assumed to be proportional to the square-root of the pressure differential $Q = K\sqrt{\Delta P}$, where K is a flow constant depending on the control voltage. Figure 7-3 shows in the top plot the flow constants as function of the control voltage u for the flows through the proportional valve. The maximum flow constants at $|u| > 10$ V for flows to and from the A-side of the cylinder are 200 l/min/bar^{½}, and 100 l/min/bar^{½} for a flow to the B-side of the cylinder. There is a deadzone for control voltages around zero $|u| < 1$ V, where the valve moves from one side to the other. This deadzone can be compensated by modulation of the control voltage, which in this first study is assumed to be ideal as shown in the bottom plot of Figure 7-3.

For positive control voltage $u > 1$, the valve is in its left position, where oil can flow from the accumulator into the B-side, and out of the A-side into the sump (from where it is pumped back into the accumulator). The pressure differences over the valve for the A- and B-sides are $P_A - P_0$ and $P_1 - P_B$, respectively.

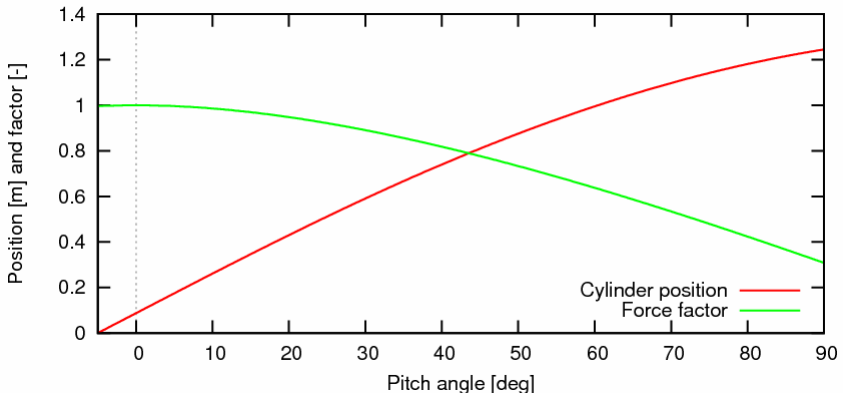

Figure 7-2: Plots of the geometrical relationships between pitch angle and the cylinder position and the geometrical force factor of piston force to actuator torque.

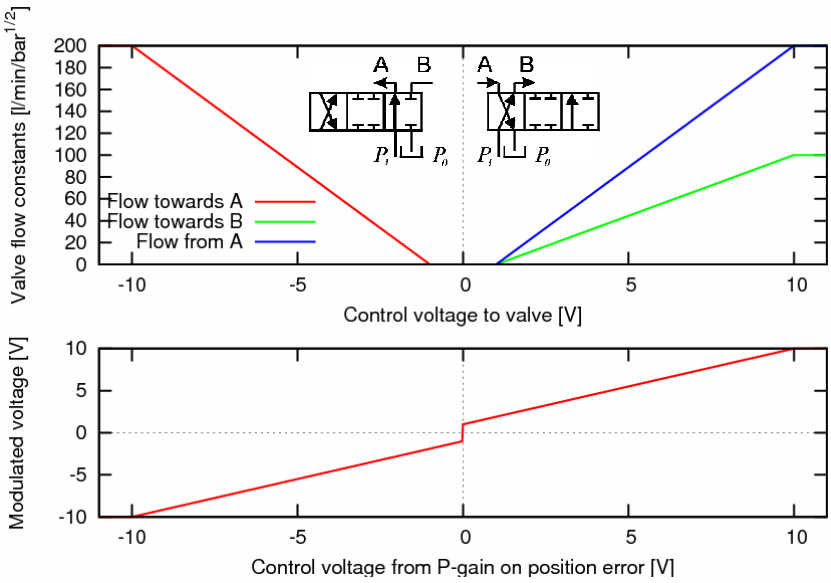

Figure 7-3: Flow constants as function of control voltage to the proportional valve including a deadzone around zero (top plot), which is assumed to be ideally compensated by the modulation of the control voltage as shown in the bottom plot.

For negative control voltage $u < -1$, the valve is in its right position, where oil can flow from the accumulator into the A-side and out of B-side back into the accumulator through the check valve if the pressure is (slightly) larger than the accumulator pressure $P_B > P_1$. The pressure difference over the proportional valve for the A-side is $P_1 - P_A$, and it is $P_B - P_1$ over the check valve for B-side. Note that in the case $P_A = P_B = P_1$, a considerable piston force acts to the right because the area difference $A_A > A_B$.

Flow limits are imposed for the proportional and check valves

The flow constant for the check valve is 50 l/min/bar^{½}, which is obtained for a pressure difference $P_B - P_1$ of more than 4 bars to model a spring-like behavior of the check valve opening. Finally, flow limits of 300 l/min and 50 l/min are imposed on the maximum obtainable flows in the proportional valve and the check valve, respectively. Note again that these valve parameters are arbitrarily chosen, but realistic values; in an actual actuator design, the choices of valves are also part of the optimization process.

The compressibility of the hydraulic oil and the flexibility of the hoses are modeled by an effective bulk modulus β of 7000 bars for the system of oil and hoses yielding:

$$\beta = \rho \frac{dp}{d\rho} \Rightarrow dp = \frac{\beta}{\rho} d\rho = \frac{\beta}{V}\left(\frac{dm}{\rho} - dV\right)$$

A pressure variation dp can arise from variation in mass dm and in volume dV. The flow Q to a volume V represents a variation in mass of $dm = \rho\, Q\, dt$. Using the effective bulk modulus and this relation, the time derivatives of the pressures in the cylinder become:

An effective bulk modulus models the oil compressibility and flexibility of the hoses

$$\frac{dP_A}{dt} = \frac{\beta}{V_A(x_p)}\left(Q_A(P_A,u) - \frac{dx_p}{dt}A_A\right) \quad \text{and} \quad \frac{dP_B}{dt} = \frac{\beta}{V_B(x_p)}\left(Q_B(P_B,u) + \frac{dx_p}{dt}A_B\right)$$

where $V_A(x_p)$ and $V_B(x_p)$ are the volumes on A- and B-sides of the piston as function of the piston position. These volume functions include the hose-volumes and "unusable" cylinder volumes, which are assumed to be $V_A(0) = V_B(l_p) = 5$ l.

Structural blade model

Blade model includes the inertia coupling between edgewise bending and torsion for a flapwise bend blade

The structural blade model is based on the model by Kallesøe [2] using second order Bernoulli-Euler beam theory. The model of the RWT blade is the same as the linear model used in Chapter 8, except that the linear partial differential equations for blade vibrations about an equilibrium (Eq. 8.2) are here discretized by three assumed blade modes in a modal expansion. As illustrated in Figure 7-4, these assumed modes are first flapwise and edgewise bending modes and a first torsional mode. The pitch bearing degree of freedom is included in the model with inertia coupling terms to all three assumed blade modes, which are strongest for the torsional mode and the edgewise bending mode when the blade is bent flapwise. The linear equations of blade motion are:

$$\mathbf{M}\ddot{\mathbf{q}} + (\mathbf{G} + \mathbf{C})\dot{\mathbf{q}} + \mathbf{K}\mathbf{q} = \mathbf{F}(T_p + T_0)$$

where the vector $\mathbf{q} = \{q_e, q_f, q_t, \theta_p\}^T$ contains the generalized coordinates for edgewise, flapwise, torsional and pitching motions of the blade, T_0 is the steady state aerodynamic torque, and $\mathbf{F}$ is the single column matrix $\mathbf{F}^T = [0\ 0\ 0\ 1]$. Matrices $\mathbf{M}$, $\mathbf{G}$, $\mathbf{C}$, and $\mathbf{K}$ are mass, gyroscopic, damping and stiffness matrices, which (except for the damping matrix) depend on the deformation state of the blade. Linear models for the undeformed (unloaded) and deformed blade (loaded as under operation at 12 m/s) are computed. The damping matrix $\mathbf{C}$ is computed as Spectral Damping [3], where the two bending modes and the torsional mode are given logarithmic decrements of 2 % and 4 %, respectively.

Note that the unsteady aerodynamic blade forces are neglected in the blade model; only the steady state aerodynamic pitch torque is used in the analysis to obtain the right mean hydraulic pressures. Frictional torque in the pitch bearing is also neglected in this first approach analysis of pitch bearing-blade-actuator dynamics.

7.2 Stability limit for the proportional gain

This section contains a stability analysis of the hydraulic pitch actuator assuming that the deformed blade is rigid with a moment of inertia about the pitch axis of I_p. The following assumptions are furthermore made to enable the linearization of the hydraulic system:

- Mean actual and reference pitch angles are zero $\theta_p = \theta_{ref} = 0 \Rightarrow dg/d\theta_p = 0$
- Variation of the actual pitch angle is small $\delta\theta_p << 1$
- Mean A-side pressure is the averaged of the accumulator and sump pressures $P_A = (P_0 + P_1)/2$
- Variation of the A-side pressure is small $\delta P_A << 1$
- B-side pressure is the accumulator pressure $P_B = P_1$ and constant $\delta P_B = 0$

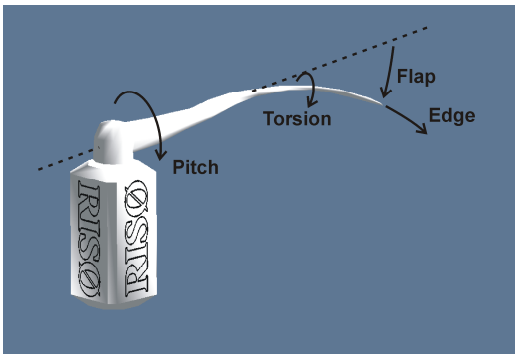

Figure 7-4: Illustration of the degrees of freedom in the blade model with three selected assumed modes: Flapwise and edgewise bending and torsional modes.

With these assumptions, the linear governing equations for the small variations of pitch angle and A-side pressure can be written as

$$\frac{d\mathbf{y}}{dt} = \mathbf{A}\mathbf{y}\text{, where } \mathbf{A} = \begin{bmatrix} 0 & 1 & 0 \\ 0 & -\eta r_p^2 / I_p & A_A r_p / I_p \\ -c_1 k_p & -c_2 & 0 \end{bmatrix}$$

where the state space vector is $\mathbf{y} = \{\theta_p, d\theta_p/dt, P_A\}^T$, and the constants c_1 and c_2 are given by the A-side valve flow constant (cf. Figure 7-3), the averaged pressure differential $(P_1 - P_0)/2$, the bulk modulus β, and the geometrical parameters r_p, l_p, and L.

Using the Routh-Hurwitz criteria for negative real parts of all eigenvalues of **A,** which ensures that any disturbance of the pitch angle away from its equilibrium is damped, the following expression for the stability limit on the gain can be derived:

$$k_{p,crit} = \frac{\eta r_p^2}{I_p} \frac{A_A}{K_{A,u}\sqrt{(P_1 - P_0)/2}}$$

where $K_{A,u}$ is the slope of the linear flow constant function of the control voltage u for the A-side of the proportional valve with ideal deadzone compensation.

This critical gain shows that the viscous damping in the pitch system given by the coefficient η has a stabilizing effect, whereas the normalized rotational pitch inertia I_p/r_p^2 has a destabilizing effect in the position error feedback loop of the actuator. The inverse of the term $A_A / \left(K_{A,u}\sqrt{(P_1 - P_0)/2}\right)$ is the area normalized gradient of the flow over the proportional valve with respect to the control voltage. This term shows destabilizing effects of the proportional valve size given by $K_{A,u}$ and the pressure differential over the valve given by $(P_1 - P_0)/2$, which can be compensated by a larger cylinder bore area A_A.

Ziegler-Nichols method is used for tuning the proportional gain

For sub-critical gains $k_p < k_{p,crit}$, the actual pitch angle will return to the reference pitch angle after a disturbance; however, too low a gain leads to a long return period, whereas a gain close to the critical gain leads to low damped oscillations of the pitch angle. Using the Ziegler-Nichols method, the gain is therefore set to half of the critical value $k_{p,crit}/2$.

Figure 7-5 shows the natural frequency and damping in terms of the real part of the eigenvalue of the feedback mode in the linearized pitch system. The natural frequency of this mode is around 7 Hz and the damping becomes negative (positive real part of the eigenvalue) around 90 V/m, which agrees with a derived critical gain. The gain is therefore set to 45 V/m in the following analysis that includes the blade flexibility.

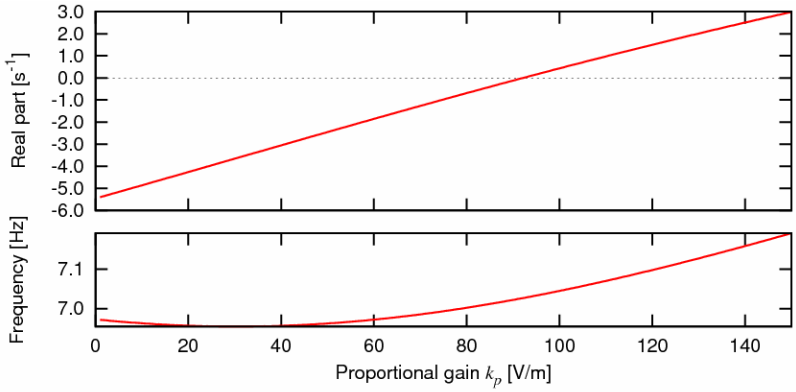

Figure 7-5: Natural frequency and real part of eigenvalue (damping) of feedback mode in the hydraulic pitch actuator as function of the gain k_p.

7.3 Transfer function from reference to actual pitch

This section contains computations of the transfer function from reference to actual pitch angle based on the model of the hydraulic actuator. These transfer functions are linear approximations to the dynamics of this highly nonlinear model.

A transfer function is a linear approximation to the nonlinear actuator dynamics

A transfer function $H(\omega)$ from reference to actual pitch angles describes the actual pitch angle response to excitation with a harmonic pitch reference variation $\theta_{ref} = a \sin(\omega t)$. For a given amplitude a and frequency ω, the actual pitch angle response is assumed to be given by $\theta_p = a\,|H(\omega)| \sin(\omega t + \arg(H(\omega)))$. This linear approximation assumes that actual pitch angle response contains only one harmonic with the frequency ω. The strong nonlinear dynamics of the actuator may lead to off-frequency contents in the response; however, in the present analysis significant off-frequency responses are only seen in the blade modal responses and not in the pitch response.

The computation of the linear transfer functions from the nonlinear model given by the structural model and hydraulic actuator model is based on the Finite-Difference Method for construction of periodic solutions in nonlinear dynamic systems [4]. The harmonic pitch reference variation $\theta_{ref} = a \sin(\omega t)$, inserted into the piston position error feedback, acts as a harmonic excitation of the nonlinear pitch bearing-blade-actuator system. One could try to obtain the steady state periodic response of this system by time-integration; however, it may require long simulation time before the transients are damped out. The above mentioned method is a direct approach, where the steady state periodic responses in pitch angle and blade motion to the harmonic excitation is constructed from the governing equations without time-integration. Once the steady state periodic pitch response is computed, a Fourier transform is performed to extract the amplitude and phase of the harmonic component with the frequency ω. This procedure is repeated for any desired number of frequencies ω to obtain the transfer function in a frequency band.

The edgewise blade mode influences the pitch angle response when the blade is bend flapwise

Figure 7-6 shows the transfer functions from reference to actual pitch below 10 Hz for the undeformed and deformed blade with a reference pitch amplitude of $a = 0.5$ deg. As shown later, both transfer functions seem to behave as a second order filter for this amplitude, except around three frequencies: Around 1 Hz, the transfer function for the deformed blade shows a resonant behavior, which is caused by excitation of the edgewise bending mode (with a natural frequency close to 1 Hz) due to the inertia coupling of edgewise bending and torsion when the blade is bend flapwise in this deformation state at 12 m/s. Around 7 Hz, both transfer functions have an increase in the transfer magnitude from reference to actual pitch, which is caused by excitation of the actuator mode with a natural frequency close to 7 Hz (cf. Figure 7-5). Around 8 Hz, both transfer functions show anti-resonant behaviors, which are caused by excitation of the torsional blade mode with a natural frequency close to 8 Hz.

Opening and closing of the check valve cause impulses in the actuator torque

More details on these behaviors can be obtained from the periodic solutions at different frequencies. Figure 7-7 shows the periodic solutions for the cylinder pressures (P_A and P_B), reference and actual pitch angles (θ_{ref} and θ_p), and blade tip motions (q_e, q_f, and q_t) of the deformed blade at the excitation frequencies 0.1 Hz and 1 Hz. At the low frequency of 0.1 Hz, the actual pitch angle follows the reference pitch angle closely. The blade responses are small. There are 1 Hz variations on top of the 0.1 Hz variations, especially in the edgewise motion. These variations are caused by excitation of the edgewise blade mode due to impulses in the actuator torque that arise when the check valve opens and closes, resulting in time-gradient discontinuities in the B-side pressure as it is limited to the accumulator pressure.

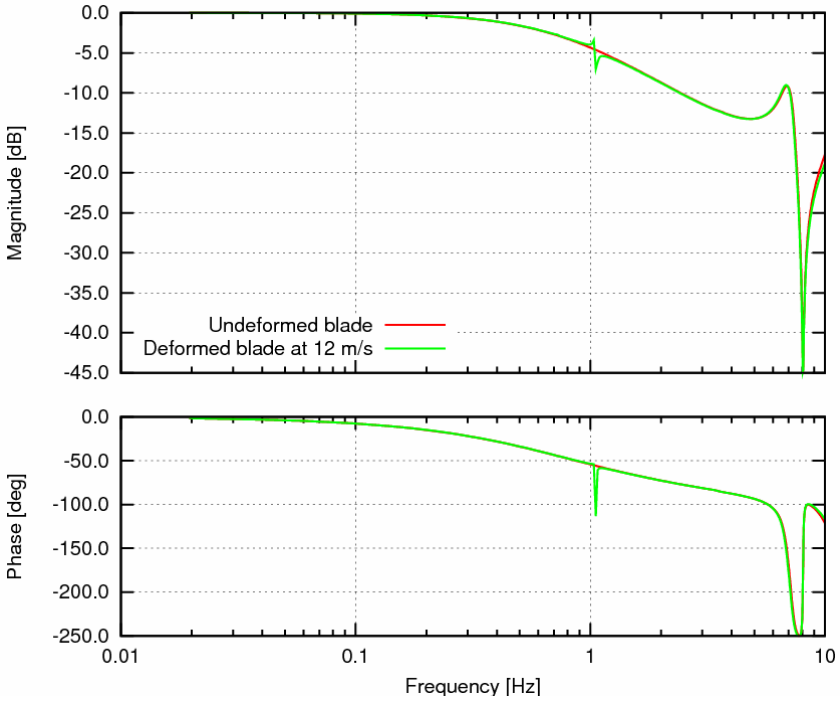

Figure 7-6: Magnitude and phase of computed transfer functions from reference to actual pitch angles for the undeformed and deformed blade with harmonic reference amplitude of 0.5 deg.

In the right plots of Figure 7-7 for the excitation frequency of 1 Hz close to the edgewise natural frequency, there is a significant edgewise component in the blade tip motion due to this near resonant excitation. The periodic solution for the pressures shows that opening and closing of the check valve during one period of oscillation are slightly softer; however, there is a small excitation of the torsional blade mode of 8 Hz due to the related impulses that also can be seen in the A-side pressure. The periodic solution for the actual pitch angle confirms the amplitude reduction and phase shift from Figure 7-6.

Figure 7-8 shows the periodic solutions for the deformed blade at higher excitation frequencies 7 Hz and 8 Hz. At the frequency of 7 Hz close to the natural frequency of actuator mode (cf. Figure 7-5), there are significant variations in the cylinder pressures due to the resonant excitation of this mode related to the compressibility of the hydraulic oil and hoses. This resonant excitation of the actuator mode increases the pitch torque variation at around this frequency. It explains the increased actual pitch angle response seen in Figure 7-6, but it also causes a large torsional blade response with a blade tip amplitude of 2 deg due to the proximity of the natural frequency of torsional blade mode at 8 Hz. It is noted that the torsional blade motion is in phase with the reference pitch angle and the pressure difference $P_A - P_B$, and thereby the pitch torque, whereas the actual pitch angle is in counter phase with the reference pitch angle.

Large variations in the cylinder pressures occurs if the actuator mode is excited

At the excitation frequency of 8 Hz, there is almost no response in the actual pitch angle, as also seen by the anti-resonance in Figure 7-6, all excitation energy goes into the torsional blade mode, resulting in a blade tip amplitude of 1 deg. At this high frequency further away from the actuator mode frequency, the B-side pressure is very close to the accumulator pressure, which shows that the check valve is almost continuously open. Note that there is a small offset in the actual pitch angle which is caused by the *biasing effect* of (relative) high-frequency excitation of strongly nonlinear systems [5].

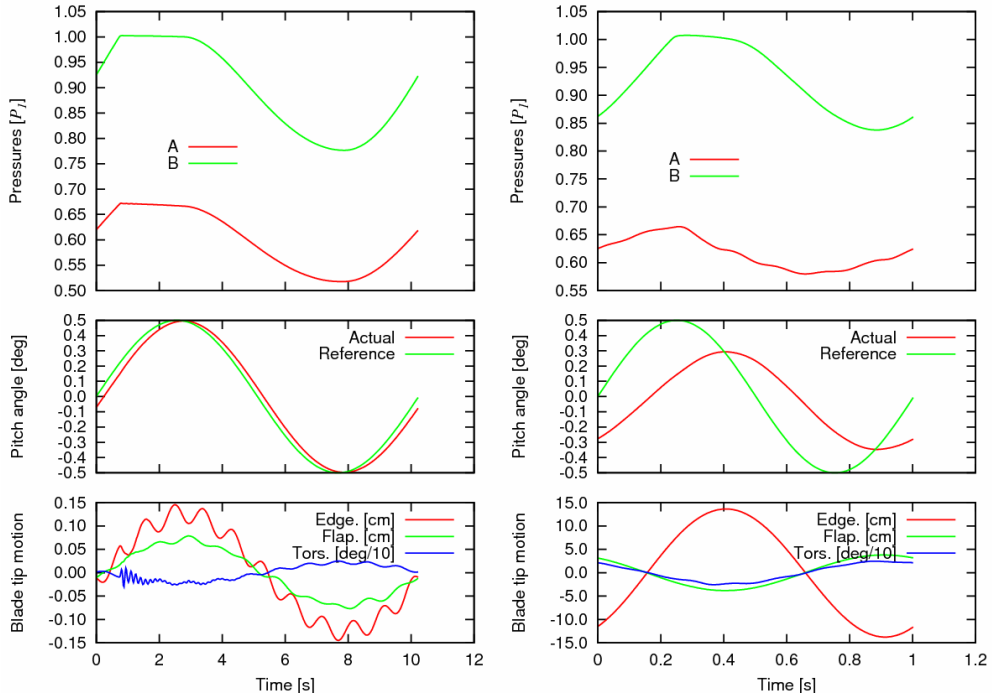

Figure 7-7: Cylinder pressures (top), reference and actual pitch angles (middle) and relative blade tip motion (bottom) for the deformed blade and excitation frequencies: Left around 0.1 Hz and right around 1 Hz.

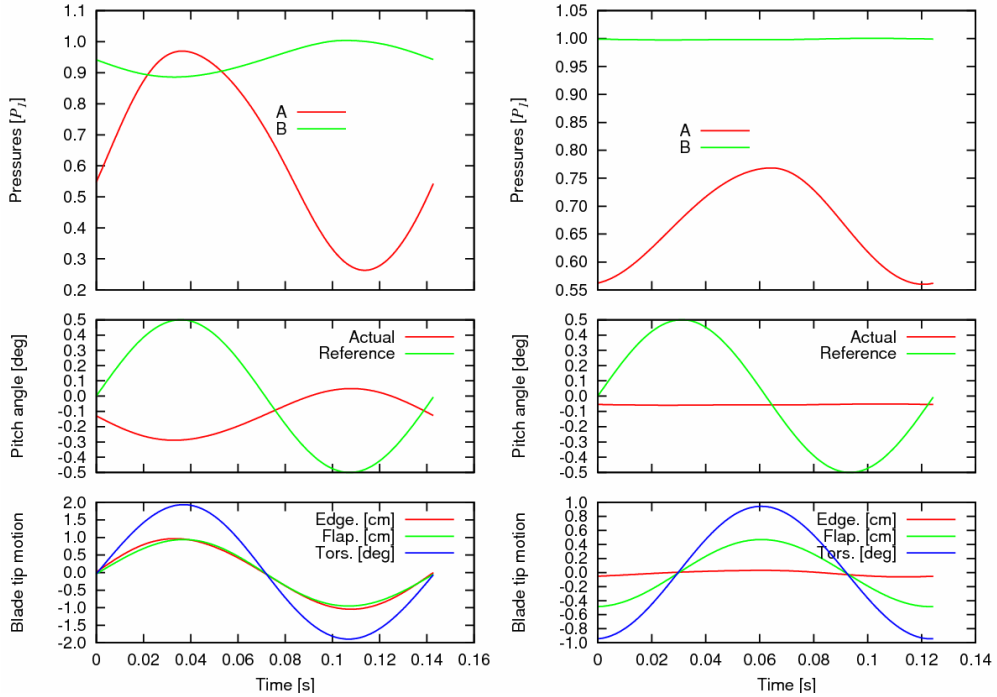

Figure 7-8: Cylinder pressures (top), reference and actual pitch angles (middle) and relative blade tip motion (bottom) for the deformed blade and excitation frequencies: Left around 7 Hz (actuator frequency) and right around 8 Hz (torsional frequency).

Figure 7-9 shows the transfer functions from reference to actual pitch angles for the deformed blade when the reference pitch amplitude is changed from 0.01 deg to 5 deg. These functions show the nonlinear effects of the limitations in valve flows, whereas limitation of the maximum torque, and thereby the pitch acceleration, has a minor effect.

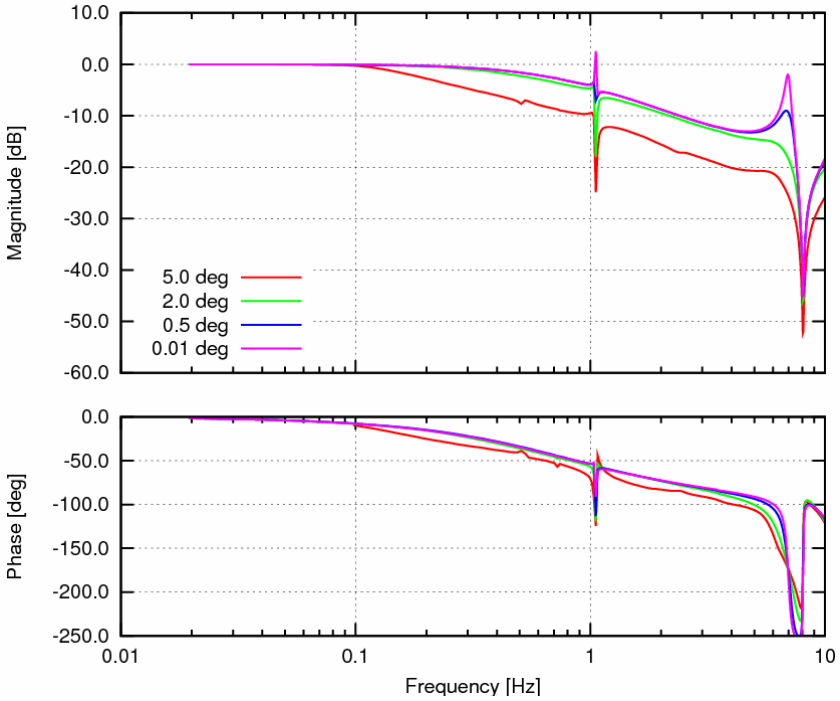

Figure 7-9: Magnitude and phase of computed transfer functions from reference to actual pitch angles for the deformed blade with different harmonic reference amplitudes: 0.01, 0.5, 2 and 5 deg.

The maximum actuator torque can be approximated by $r_p P_1(A_A - A_B)$ and $r_p(P_1 A_B - P_0 A_A)$ for pitching in the two directions, assuming that the viscous forces on the piston can be neglected. If these maximum torques are divided by the rotational pitch inertia I_p, it can be shown that the maximum pitch acceleration of the deformed blade is over 100 deg/s^2. Such a high limit indicates that the cylinder may be over-dimensioned. The maximum pitch velocity can be approximated by $Q_{c,max}/A_B/r_p \approx 2$ deg/s and $Q_{p,max}/A_A/r_p \approx 9$ deg/s for pitching in the two directions, where $Q_{c,max} = 50$ l/min and $Q_{p,max} = 300$ l/min are the imposed maximum obtainable flows through the check and proportional valves, respectively. These low maximum limits on the pitch velocity show that the two valves with the imposed flow limits are under-dimensioned (especially the check valve) relative to the over-dimensioned cylinder for the given torque arm r_p.

The transfer function in Figure 7-9 for the pitch reference amplitude of 5 deg is the only function to show significant limitations of the actuator. This limitation of the actual pitch angle starts around 0.1 Hz, which corresponds to a maximum pitch velocity of about 3 deg/s and a maximum acceleration of about 2 deg/s^2. From the theoretical predictions of the maximum pitch velocity and acceleration, it is concluded that the reduction of the transfer function at 5 deg reference pitch amplitude above 0.1 Hz is caused by the under-dimensioned valves (or the over-dimensioned cylinder).

The valves seem to be under-dimensioned in the present actuator design

The above results show that the analyzed hydraulic pitch actuator may not be well-designed for the 5 MW RWT. However, the analysis shows the method for redesigning the actuator with respect to its geometry and the sizes of the valves and the cylinder.

Second order filter approximation

In aeroelastic simulation of wind turbines, the pitch actuator is often modeled as a second order low-pass filter, i.e., the transfer function from reference and actual pitch angles is approximated by the complex function $H_f(\omega) = \omega_0^2/(\omega_0^2 - \omega^2 + i\, 2\, \beta\, \omega_0\, \omega)$.

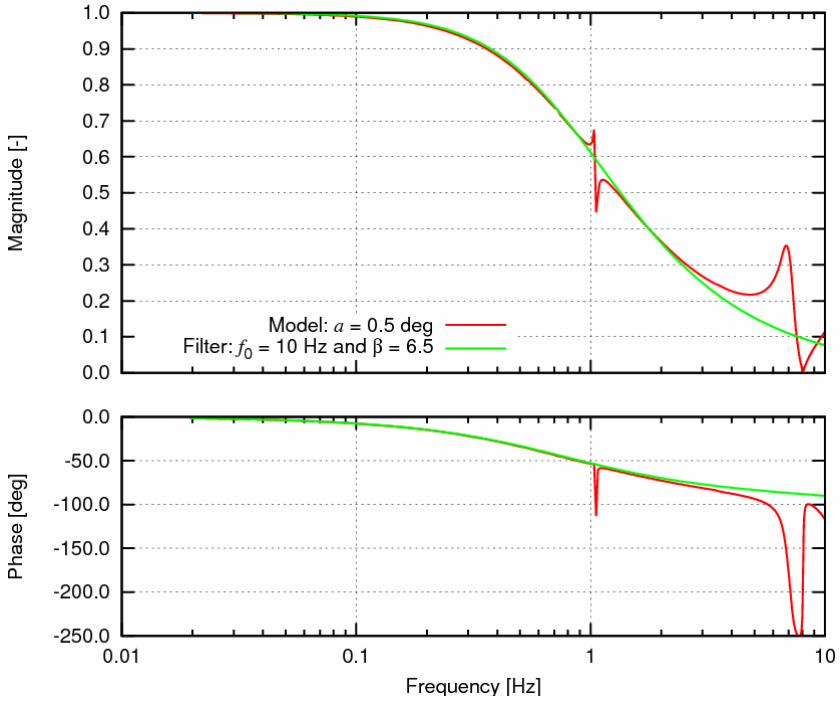

Figure 7-10: Magnitude and phase of computed and approximated transfer functions from reference to actual pitch angles for the deformed blade with harmonic reference amplitude of 0.5 deg. Second order filter parameters are center frequency of 10 Hz and damping ratio of 6.5.

A 2nd order low-pass filter is a good approximation to the hydraulic pitch actuator; noting that limits on the pitch velocity and acceleration may be needed

Figure 7-10 show a fit of this second order filter transfer function to the transfer function for the deformed blade obtained from the physical model with a pitch reference amplitude of 0.5 deg (cf. Figure 7-6). A good fit is obtained for a filter frequency ω_0 of 10 Hz and a damping ratio β of 6.5. The simple filter model of the actuator based on angles only does not capture the interaction with the blade modes around 1 Hz and 8 Hz, and of course not the hydraulic pitch actuator mode at 7 Hz. Furthermore, the transfer function $H_f(\omega)$ of this linear filter is independent of the pitch reference amplitude. However, it may be possible to model the limitations of the actuator by imposing limitations on the maximum pitch velocity and accelerations.

7.4 References

[1] J. Jonkman, *NREL 5 MW baseline wind turbine*, Technical report, NREL/NWTC, 1617 Cole Boulevard; Golden, CO 80401-3393, USA, 2005.

[2] B. S. Kallesøe, 'Equations of motion for a rotor blade, including gravity, pitch action and rotor speed variations', *Wind Energy* **10**, pp. 209-230, 2007.

[3] R. W. Clough and J. Penzien, *Dynamics of Structures*, McGraw-Hill, 1975.

[4] A. H. Nayfeh and B. Balachandran, *Applied Nonlinear Dynamics*, Wiley, 1995.

[5] J. J. Thomsen, *Vibrations and Stability*, 2nd Edition, Springer, 2003.

8 Large Blade Deformations Effect on Flutter Boundaries

Bjarne S. Kallesøe

This chapter concerns the question "how deformation of a turbine blade under normal operation affects the flutter boundaries". At some stages of normal operation of a turbine the blades have a large flapwise deflection, but also edgewise and torsional deflections can be considerable. These deflections affect the coupling between blade motions in the different directions, e.g. edgewise vibrations of a flapwise deflected blade couples directly to torsional motion of the blade.

Natural modes of an undeformed blade are compared to those of a pre-deformed blade

In this work natural modes of aeroelastic motions of an undeformed blade are compared to that of a pre-deformed blade. The blade pre-deformation is taken as the deformation at normal operation at 11 m/s. This pre-deformation is kept as rotation speed is increased and the natural frequencies and damping are computed.

The analysis shows that blade deformation does affect the flutter boundaries. On the one hand the flutter instability known from the undeformed blade is delayed to a higher rotational speed, on the other hand a new rout to flutter instability appears, which has a lower stability boundary then the original flutter boundary for the undeformed blade.

8.1 Method

The Model

The aeroelastic model is based on the blade model suggested in [1] combined with an aerodynamic model including the dynamic stall model, suggested in [2], as described in [3]. In state space form the nonlinear equations of aeroelastic motion take the form

$$\frac{\partial \mathbf{u}(r,t)}{\partial t} = \mathbf{f}\left(\mathbf{u}, \frac{\partial \mathbf{u}}{\partial r}, \frac{\partial^2 \mathbf{u}}{\partial r^2}, \frac{\partial^3 \mathbf{u}}{\partial r^3}, \frac{\partial^4 \mathbf{u}}{\partial r^4}, \Omega \right) \tag{8.1}$$

where the state vector $\mathbf{u}$ holds the deformations, velocities and aerodynamic states. The nonlinear state space equations of motion are linearized about both a straight blade position and about a pre-deformed blade position. The linear state space equations of aeroelastic motion take the form

$$\begin{aligned} \frac{\partial \mathbf{u}_1(r,t)}{\partial t} = & \frac{\partial^2}{\partial r^2}\left(\mathbf{K}_{ss}(r,\Omega,\mathbf{u}_0) \frac{\partial^2 \mathbf{u}_1(r,t)}{\partial r^2} \right) \\ & + \frac{\partial}{\partial r}\left(\mathbf{K}_{s}(r,\Omega,\mathbf{u}_0) \frac{\partial \mathbf{u}_1(r,t)}{\partial r} \right) + \mathbf{K}(r,\Omega,\mathbf{u}_0)\mathbf{u}_1 \end{aligned} \tag{8.2}$$

where the subscript 0 denote the steady state part of the state and the subscript 1 denotes the linear part of the state. By linearizing the equations of motion about the pre-deformed blade position the main effects of geometric nonlinearities are preserved. This can be illustrated by a bilinear term such as uv, where u and v are the edgewise and flapwise deflection, respectively. This term is equal to zero if linearized about the undeformed blade and equal to $u_0 v_1 + u_1 v_0$ if linearized about the deformed blade.

The spatial derivatives of the linearized aeroelastic equations of motion are discretized by a second order finite difference scheme leading to a differential eigenvalue problem

$$\frac{d\tilde{\mathbf{u}}_1(t)}{dt} = \mathbf{A}\left(\Omega, \tilde{\mathbf{u}}_0\right)\tilde{\mathbf{u}}_1(t) \tag{8.3}$$

where the new state vector $\tilde{\mathbf{u}}_1$ holds the linear state values at each of the discretization points and $\tilde{\mathbf{u}}_0$ holds the steady state part of the states at each discretization point. The solution to this differential eigenvalue problem gives the frequencies, damping and shapes of natural vibrations of the blade.

The Numerical Experiment

The two differential eigenvalue problems based on the undeformed and the pre-deformed blade, respectively, are solved for increasing rotation speed with no wind and zero pitch. There is no structural damping included in this test.

8.2 Results

A 61.5-m blade is investigated

The blade used in this work is the 61.5 m blade from the NREL large scale test turbine. To give a natural deformation pattern for the pre-deformed blade used in the analysis the pre-deformation is chosen as the deformation of the blade at normal operation at 11 m/s (zero pitch and a rotational speed of $\Omega = 1.27$ rad/s). Figure 8-1 shows the steady state deformation of the blade at this operational condition.

This deformation pattern is used at all rotational speeds to investigate the isolated effect of a known deformation.

Figure 8-2 and Figure 8-2 shows the frequencies and damping for the first seven eigenmodes of motion for the undeformed and deformed blade, respectively, for different rotational speeds. The modes a numbers after their eigenfrequency at 1 rad/s, such that first mode is the mode with lowest eigenfrequency.

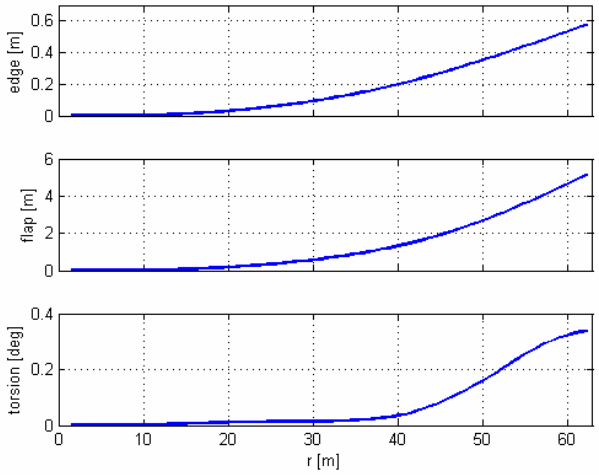

Figure 8-1 Blade deformation at normal operation at 11 m/s

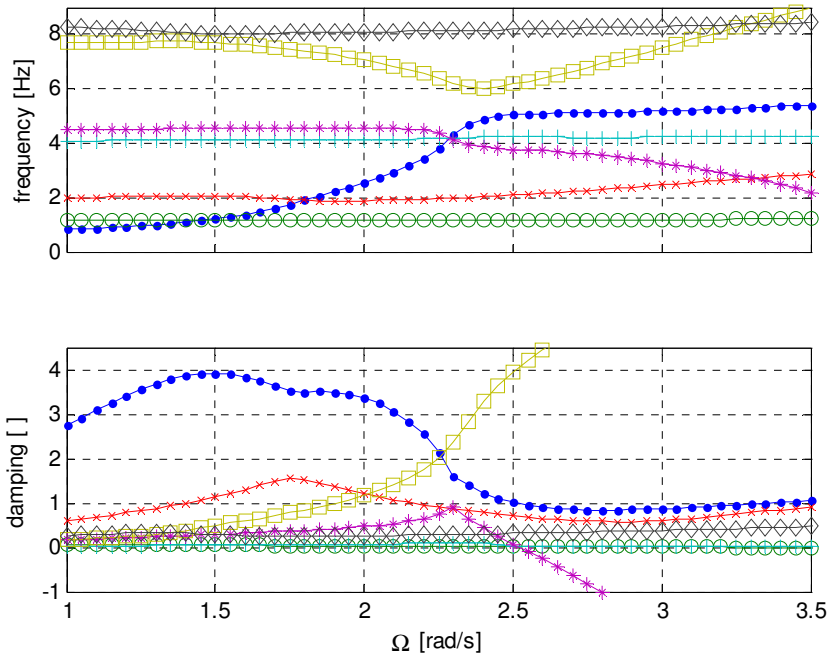

Frequencies and damping for an undeformed blade

Figure 8-2 Frequencies and damping for the undeformed blade.

For the undeformed cases (Figure 8-2) the fifth mode is seen to become negatively damped at 2.52 rad/s (which agrees well with a HAWCStab computation). Figure 8-4 shows the flapwise, edgewise and torsional contents in the fifth mode at different rotational speeds. It is seen that the fifth mode is the third flapwise dominated mode. At increasing rotational speeds it interacts with the torsional motion and becomes a combined second flapwise and torsional mode with negative damping, known as flutter.

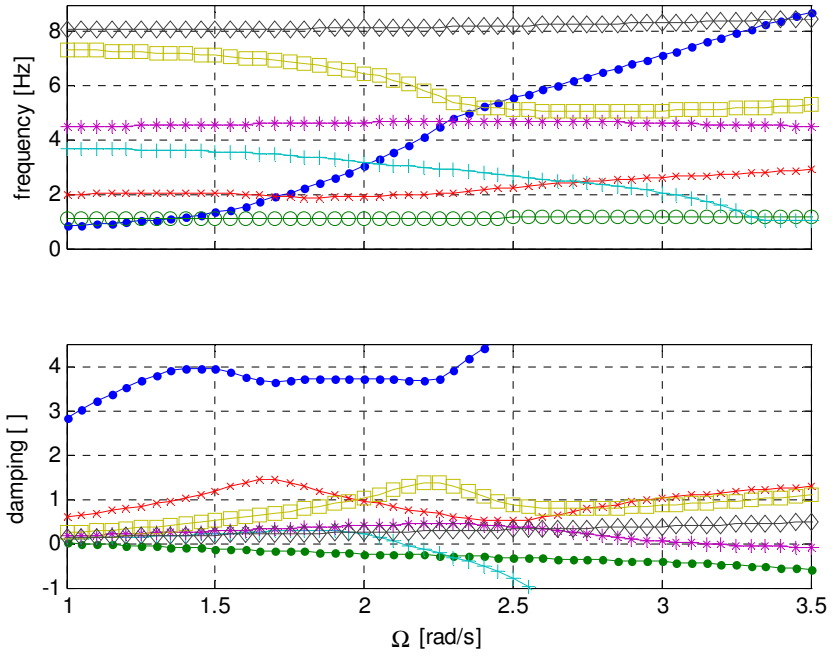

Frequencies and damping for a deformed blade

Figure 8-3 Frequencies and damping a blade deformed as for normal operation at 11 m/s.

For the deformed case (Figure 8-3), the fifth mode becomes negatively damped at 3.1 rad/s, that is at 23 % higher rotational speed than for the undeformed blade. Figure 8-4 shows that the relation between flapwise, edgewise and torsional contents for the pre-deformed blade at $\Omega = 3$ is almost the same as for the undeformed blade at $\Omega = 2.6$. That is, the pre-deformation delays the flutter instability of the fifth mode.

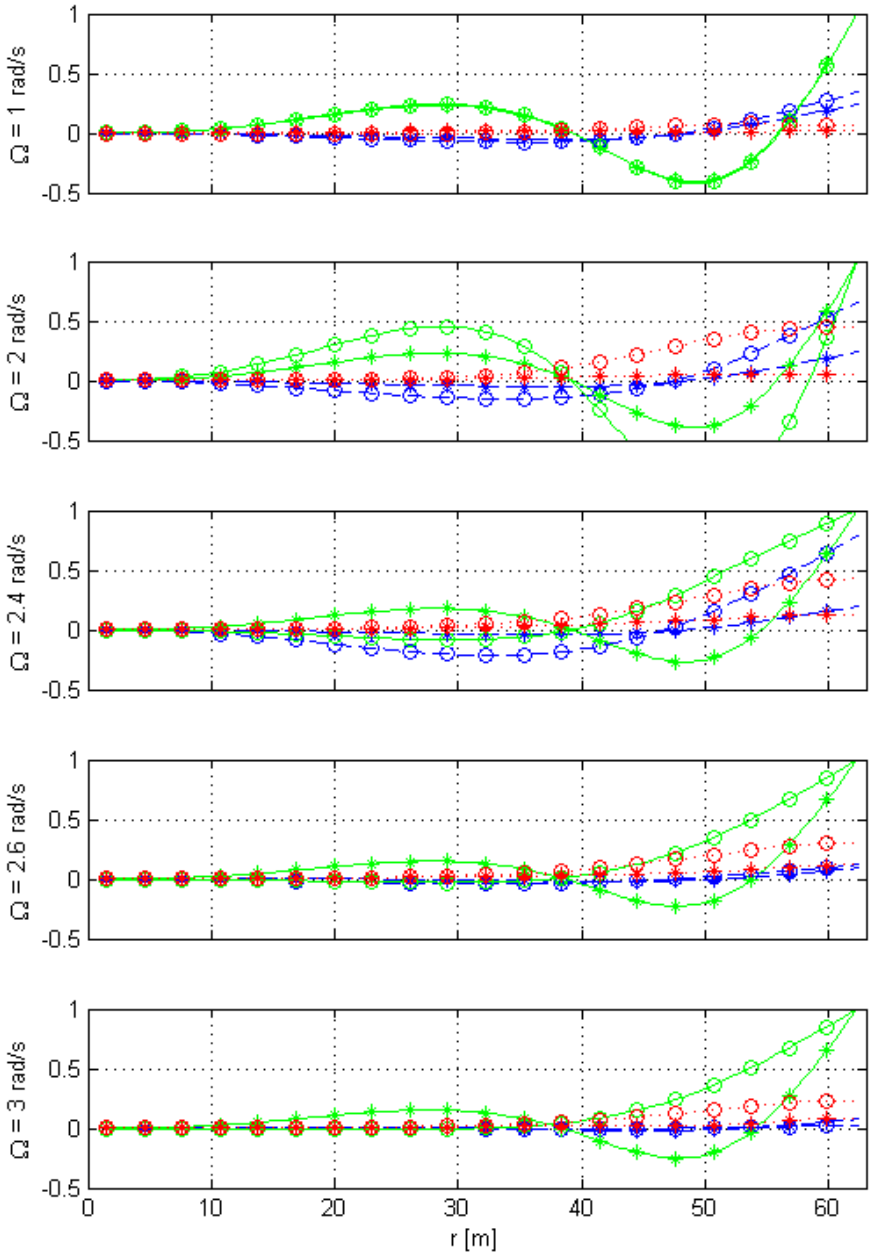

Figure 8-4 Fifth mode for different rotation speeds. 'o' marks undeformed blade, '' blade deformed as shown on* Figure 8-1. *Green line marks flapwise contents, blue line marks edgewise contents and red line marks torsional contents in the particular mode.*

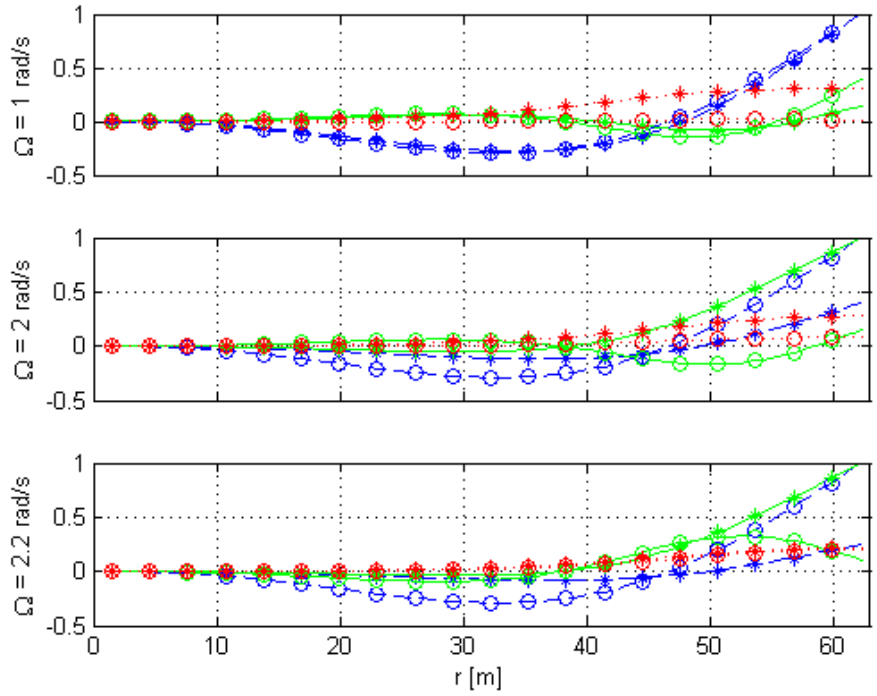

Figure 8-5 Fourth mode for different rotation speeds. 'o' marks undeformed blade, '' blade deformed as shown on* Figure 8-1. *Full line marks flapwise contents, dashed line marks edgewise contents and dotted line marks torsional contents in the particular mode.*

Figure 8-3 shows that the fourth mode of the deformed blade becomes negatively damped at $\Omega = 2.12$ where the fourth mode of the undeformed blade stay positive damped for all tested rotational speeds. Figure 8-5 shows the flapwise, edgewise and torsional contents of the fourth mode for the deformed and undeformed blade.

It is seen that for the undeformed blade the fourth mode is the second edgewise dominated mode for all rotational speeds. For the pre-deformed blade the coupling between the directions of motion are stronger and the second edgewise mode couples to the flapwise motion. When the rotational speed increases the fourth mode turns into a second flapwise dominated mode combined with torsional motion and become negatively damped. This flutter instability appears at 16 % lower rotational speed than the flutter instability for the undeformed blade.

The second mode of the pre-deformed blade (Figure 8-3) is seen to be increasingly negatively damped for increasing rotation speed. Figure 8-6 shows the flapwise, edgewise and torsional contents of the second mode for the undeformed and pre-deformed blade. For the undeformed blade the second mode is seen to be a first edgewise dominated mode. For the pre-deformed blade the edgewise motion couples to flapwise motion and, for increasing rotational speed, becomes a combined first flapwise and first edgewise mode.

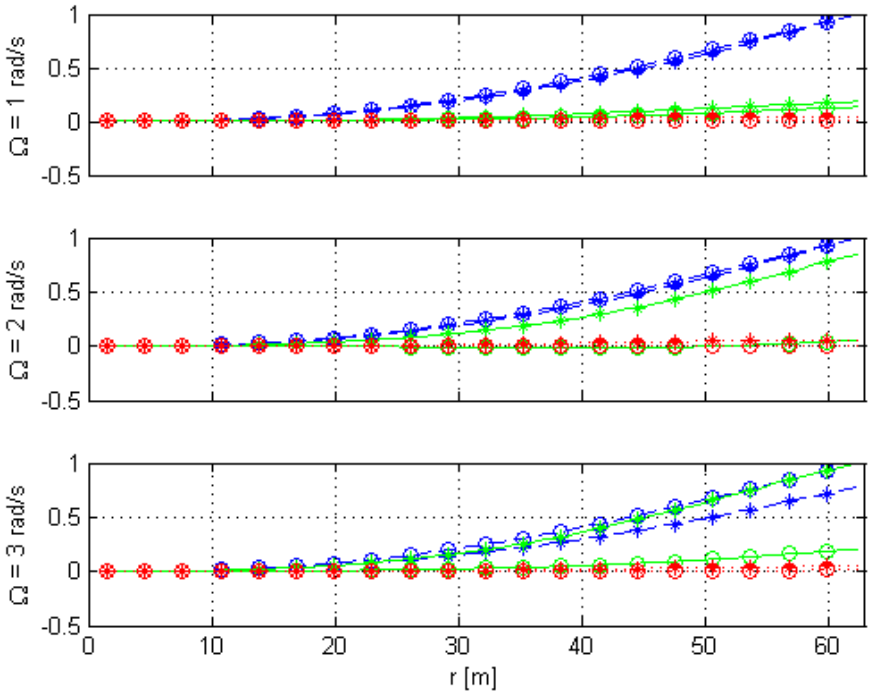

Figure 8-6 Second mode for different rotation speeds. 'o' marks undeformed blade, '' blade deformed as shown on Figure 8-1. Full line marks flapwise contents, dashed line marks edgewise contents and dotted line marks torsional contents in the particular mode.*

8.3 Conclusion

The analysis showed that blade deformation has a strong effect on the dynamics of the blade

This analysis shows that blade deformation which occurs at normal operation of a turbine has a strong effect on the dynamics of the blade.

- The undeformed blade has a flutter instability at rotation speeds above 2.52 rad/s. The same route to flutter for the pre-deformed blade is delayed such that it becomes unstable at 3.1 rad/s, that is a 23 % higher rotational speed.
- The deformation of the blade introduce a new route to flutter, which becomes unstable at 2.12 rad/s, that is a 16 % lower rotational speed compared to the flutter unstable for the undeformed blade.
- Furthermore, the first edgewise dominated mode couples to first flapwise motion and becomes increasingly negatively damped for increasing rotational speed.

It should be noted that this analysis is a theoretical analysis of large blade deformations effect on flutter boundaries. Since the blade deformation is prescribed and not the actual deformation at the given operation conditions the found instabilities are not descriptions of stability boundaries for operation of the turbine.

8.4 Reference

[1] B.S. Kallesøe, Equations of Motion for a Rotor Blade, Including Gravity, Pitch Action and Rotor Speed Variations, Wind Energy (in press)
[2] Hansen M.H., Gaunaa M., and Madsen H.A. A beddoes-leishman type dynamic stall model in state-space and indicial formulation. Technical report, Risø National Laboratory, August 2004.
[3] B.S. Kallesøe, Aeroservoelasticity of Wind Turbines, PhD thesis, the Technical University of Denmark, Department of Mechanical Engineering, January 2007.

9 Detailed Nacelle Dynamics

Anders Melchior Hansen

9.1 Introduction

The aim of the work is to investigate whether the presently simplified way of modeling the nacelle in aeroelastic simulations is sufficient to capture the essential dynamics of the nacelle components or if more emphasis shall be put into this part of the structure in the future. The investigation is made by use of the aeroelastic simulation program HAWC2.

It is investigated whether the presently simplified way of modeling the nacelle in aeroelastic computations is sufficient to capture essential dynamics

Presently in HAWC2, the structural aeroelastic modeling of the nacelle is modeled by a single rotating beam constrained to rotate relative to the tower top node at one end of the beam. At the opposite end of the beam the rotor is rigidly attached. The generator is modeled by a rotating mass attached to the shaft end and the gearbox ratio is accounted for by scaling the inertia of this rotating mass with the gear box ratio squared.

This simplified way of modeling the nacelle dates back to the old aeroelastic simulation code, HAWC, in which the topology was limited to that described above. However, HAWC2 does not limit the topology of the wind turbine model to meet such simplified constraints, and it is natural to investigate the difference in the dynamic response, based on a more detailed nacelle model which includes the drive train and the frame structure.

The transfer of loading from the rotor through the shaft and into the tower is in the normal modeling handled by the generator control algorithm. The control algorithm supplies a torque moment (referred to the low speed shaft) which is applied to the generator and the same moment is then applied to the tower top node in the opposite direction. This implies that the transferred loading to the tower becomes highly dependent on the control algorithm itself.

In a real turbine, however, only a few percent of the driving torque is transferred to the generator through the gearbox while the remainder is transferred directly to the tower via the gearbox ring wheel and the frame on which the gearbox is mounted. In the real turbine, the control algorithm therefore only controls a few percent of the total loading to the tower while the remainder is transferred more directly than what is presently modeled. The interaction between the gearbox and the rest of the wind turbine structure will be captured in the new detailed aeroelastic model.

This modeling difference might be important for the overall dynamic response, not only for the wind turbine response, but also for the gearbox response, and thus for the loading input which the gearbox manufacturer uses in the dimensioning of the gearbox itself.

9.2 Scope of work

The main effort in the project focuses on the expansion of HAWC2 to handle other dynamic systems than beam structures. This is done in a generalized way so that this capability can be exploited in the future use of HAWC2. A simplified dynamic model of a single planet stage of a gearbox is formulated and the gearbox model is included in a detailed nacelle model of an aeroelastic model. The detailed model is simulated by use of the new solver in HAWC2 and the dynamic response of this model is compared to the response of the normal model in order to identify the significance of the detailed

modeling. Finally, a study of the influence of the support structure dynamics is made based on the simplified model of the gearbox.

9.3 Implementation of External Dynamic Systems in HAWC2

New capabilities of modeling in HAWC2 are implemented

This section describes the new capabilities which were built into HAWC2 in order to model the gearbox dynamics in more detailed, but first a brief description of HAWC2 is given.

HAWC2 solves the equations of motion for spatial structures composed of beams. The equations of motion are formulated in a coordinate system which is free to translate and rotate in space. Several of these entities of beams and their corresponding coordinate system (referred to as “bodies”) can be defined and restricted in their movement relative to each other through algebraic equations (referred to as “constraints”). Typically, when modeling the structure of a wind turbine in HAWC2, 14 bodies containing a maximum of 10 beam elements per body and approximately 6 constraint equations for each body (i.e. approx. 84 equations) are used. The external forces (aerodynamic, hydrodynamic, etc.) are applied to the deformed structure. The resulting set of second order, non-linear differential equations are converted from continuous to discrete time by use of the Newmark scheme and subsequently solved by a modified Newton-Raphson method. The block structure of the body formulation is exploited in order to achieve an efficient solution scheme.

It is not possible to model the dynamics of a gear box by use of beam elements. Therefore, a new generalized module which makes it possible to solve the equations of motion for other types of dynamic systems than beam structures was developed. The new dynamic systems can then be coupled to the existing beam structures by formulating appropriate constraint equations. As stated, the new module is generalized in such a way that it allows to solve not only gearbox dynamic equations but to include other second order differential equations, e.g. generator models, foundation models, electrical grid models, etc. An example of the use of the new generalized solution module by including a simplified model of a planet gearbox in an aeroelastic simulation is given in the next section.

9.4 Influence of Gearbox Dynamics in Aeroelastic Simulations

Simplified Gearbox Model

In this section a simplified model of a gearbox is formulated. Even though the model is fairly simple, it still captures the transfer of loading from the rotor to the tower, as described in the introduction.

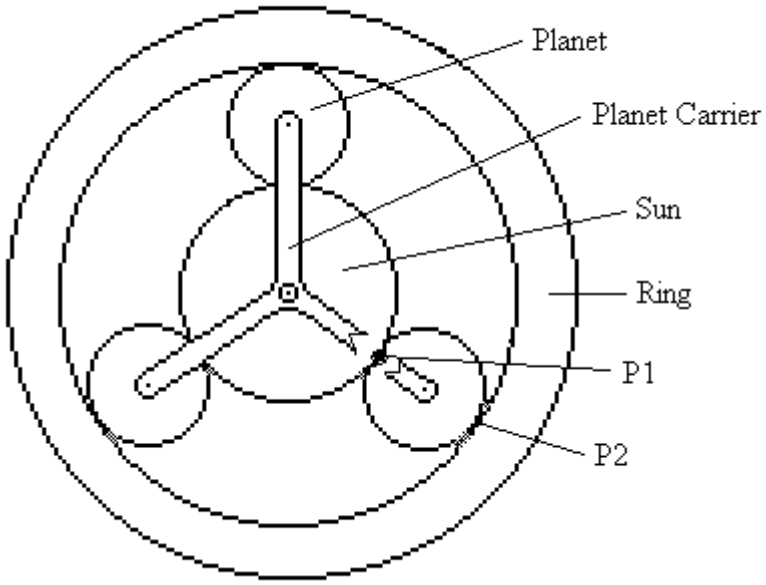

Figure 9-1: Sketch of simplified gearbox model.

The model is sketched in Figure 9-1 which shows a single gear stage of a planet gearbox. The model contains 4 states, namely the rotation angles of the sun, ϕ_s, the planet carrier, ϕ_p, the ring, ϕ_r, and the planet wheel, see Figure 9-1. The latter state is not given a symbol because this state will later be condensed. Two springs at each sun wheel are then introduced, one between the sun and the planet (at P1 in Figure 9-1) , and one between the opposite side of the planet and the ring (at P2 in Figure 9-1). The 4x4 dimensional stiffness matrix corresponding to this spring system is then derived by use of the Principle of Virtual Work. It is then assumed that the inertia of the planets can be ignored, and that no external loads act on the planets, which implies that the state related to the rotation of the planets can be condensed. The resulting 3x3 dimensional stiffness matrix which relates the external moments M_p, M_r, and M_s, acting on the planet carrier, ring, and sun, respectively, and the gear wheel rotation states, is given by the relation:

$$\begin{Bmatrix} M_p \\ M_r \\ M_s \end{Bmatrix} = K_s \begin{bmatrix} 1 & \left(\frac{1}{n}-1\right) & -\frac{1}{n} \\ \left(\frac{1}{n}-1\right) & \frac{(n-1)^2}{n^2} & \frac{(n-1)}{n^2} \\ -\frac{1}{n} & \frac{(n-1)}{n^2} & \frac{1}{n^2} \end{bmatrix} \begin{Bmatrix} \phi_p \\ \phi_r \\ \phi_s \end{Bmatrix}$$

The stiffness matrix only depends on two parameters, the gear ratio n and the gear box stiffness K_s. K_s is seen to be defined as the relation between the planet carrier moment, M_p, and angle, ϕ_p, for fixed ring and sun wheels. The stiffness matrix is seen qualitatively to possess sensible properties since the sum of each column is zero, meaning that in case of static external loading acting on the gearbox, these external forces are in equilibrium, independent on the state vector. Further, the null-space, which describes a certain relation between the state variables for which the gearbox is stress free, is spanned by a linear combination of these two vectors:

$$\mathbf{n_1} = \begin{Bmatrix} \frac{1}{n} \\ 0 \\ 1 \end{Bmatrix}, \quad \mathbf{n_2} = \begin{Bmatrix} 1 \\ 1 \\ 1 \end{Bmatrix}$$

The first null-vector corresponds to normal operation of the gearbox, where the ring wheel is fixed, and the ratio between the input and output of the gearbox, i.e. the planet carrier angle and the sun wheel angle, is equal to the gear ratio, n. The second null-vector corresponds to a mode with no relative movement between the individual gear wheels.

Besides from the three state variables used in the stiffness matrix, additional six states, which describe the rigid body motion of the whole gear box, are added to the total dynamic gear model. This gives a total of nine state variables for the gearbox model. The states related to the gear wheels are measured relative to the rigid body coordinate system and therefore no elastic energy is associated with these rigid body states. However, the kinetic energy of the gearbox is dependent on both the rigid body states and the original rotational states, which is reflected in the resulting mass matrix below.

$$\mathbf{M} = \begin{bmatrix} \sum_i m_i & 0 & 0 & 0 & 0 & 0 & 0 & 0 & 0 \\ 0 & \sum_i m_i & 0 & 0 & 0 & 0 & 0 & 0 & 0 \\ 0 & 0 & \sum_i m_i & 0 & 0 & 0 & 0 & 0 & 0 \\ 0 & 0 & 0 & \frac{1}{2}\sum_i m_i r_i^2 & 0 & 0 & 0 & 0 & 0 \\ 0 & 0 & 0 & 0 & \sum_i m_i r_i^2 & 0 & m_1 r_1^2 & m_2 r_2^2 & m_3 r_3^2 \\ 0 & 0 & 0 & 0 & 0 & \frac{1}{2}\sum_i m_i r_i^2 & 0 & 0 & 0 \\ 0 & 0 & 0 & 0 & m_1 r_1^2 & 0 & m_1 r_1^2 & 0 & 0 \\ 0 & 0 & 0 & 0 & m_2 r_2^2 & 0 & 0 & m_2 r_2^2 & 0 \\ 0 & 0 & 0 & 0 & m_3 r_3^2 & 0 & 0 & 0 & m_3 r_3^2 \end{bmatrix}$$

The states related to the mass matrix are order so that the first six states are the rigid body states, three translations followed by three rotations, and the remaining three states are the gear wheel states. It is assumed that the gear wheels rotate around the instantaneous y-axis. The summations are taken over all three gear wheels, and m_i and r_i are the mass and radius of gyration, respectively, for the individual gear wheels. A final reduction of the gearbox model is made by forcing the ring wheel state to be fixed resulting in a total of 8 states.

Detailed Aeroelastic Model

The *normal* (old) way of modeling the wind turbine structure is described in the introduction, i.e. it contains the tower, the shaft, and the rotor. The *detailed* (new) model includes the same three main components as the old, but the shaft end, where the generator mass was located in the normal model, is no longer constrained to the tower top node. The detailed model includes a frame structure with one end connected rigidly to the tower top. At the other end of the frame structure, a bearing (constraint) is positioned which connects the shaft end (closest to the rotor) and the frame. The gearbox model is fixed to the tower top and the planet carrier angle of the gearbox is fixed to rotate with the shaft end. Finally, a new generator body is introduced which is fixed to rotate with the sun wheel angle of the gearbox. The generator body is simply modeled as a rigid body with the same rotational inertia as the physical generator (i.e. not scaled by the gear ratio (squared) as for the normal model).

The same generator control algorithm as for the normal model is also used for the detailed model, however, the generator torque returned by the control algorithm is scaled by the gear ratio and acts on the new generator body and on the tower top in opposite directions.

Validation example

The new model and the implementation of the gearbox model were validated by a simulation run. All but the gearbox model was defined stiff leaving only the gearbox flexible. Knowing the inertia of the rotor and the generator, the natural frequency of the drive train can be calculated analytically and compared to the response of the simulation. As input signal to the simulation a random input to the generator body was used, and the natural frequency of the simulation model was then found by identification of the peak in one of the relevant output sensors – in this case from the shaft torque sensor.

The new model and the implementation of the gearbox model were validated by a simulation run

The analytical solution to the eigenvalue problem corresponding to stiff wind turbine structure and flexible gear box as described above is given by the following eigenfrequency (in Hz)

$$f = \frac{1}{2\pi}\sqrt{K_s\left(\frac{1}{I_{rotor}} + \frac{1}{n^2 I_{gen}}\right)}$$

and eigenvector

$$\mathbf{v} = \begin{Bmatrix} -\frac{nI_{gen}}{I_{rotor}} \\ 1 \end{Bmatrix}$$

The two terms in the eigenvector are the amplitude of the planet carrier and the sun wheel, respectively. From the eigenvector it is seen that the terms are of different signs meaning that this particular mode corresponds to the free-free mode of vibration where the rotor and the generator vibrates in counter-phase. From the HAWC2 model we obtain the following values for the rotor moment of inertia, $I_{rotor} = 3.9 \cdot 10^7 kg \cdot m^2$, the (effective) generator moment of inertia, $I_{gen} = (535 + 21) kg \cdot m^2$ (which is the sum of the generator structure and the sun wheel), the gear ratio, $n = 97$, and the gearbox stiffness, $K_s = 8.68 \cdot 10^8 Nm$. By use of these values we obtain the natural frequency $f = 2.18 Hz$ and the eigenvector $\mathbf{v} = (-0.00138, 1)$. These numerical values can be validated from the simulated response shown in Figure 9-2 from which a peak count gives the frequency (21 peaks/9.6s) = 2.19 Hz, and the ratio between sun and planet amplitude is read to be (-0.027/19.4) = -0.00139, i.e. in agreement with the analytically obtained values.

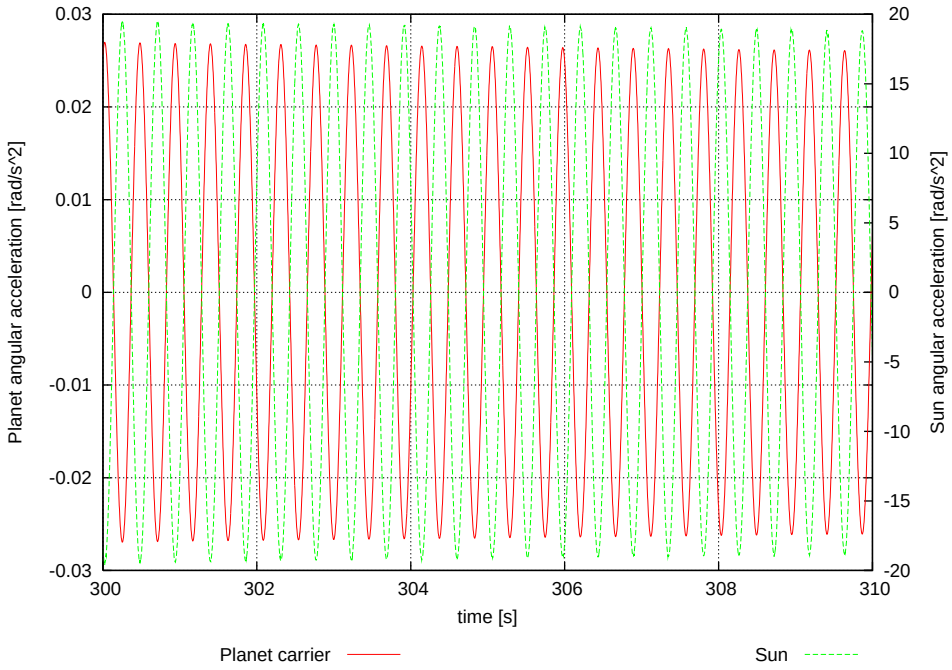

Figure 9-2; Simulated response of planet (left axis of ordinates) and sun (right axis of ordinates) angular acceleration.

Results of Aeroelastic Simulations

The new model and a traditional model is compared

The significance of using a more detailed model is investigated next by making a comparison between aeroelastic simulations with both models. The aeroelastic model used is of a fictitious 5MW wind turbine. The exact same wind input is used in both simulations and the results are compared after the time where all startup transients has died out.

Figure 9-3 and Figure 9-4 below show a comparison between the response of the normal and the detailed model for two different output sensors – the shaft torque moment sensor is shown in Figure 9-3 and the tower top moment sensor (side-to-side) is shown in Figure 9-4. Each figure contains two graphs, one showing the power spectrum of the respective sensor for the normal model and the other showing the same for the detailed model.

Generally, the response spectra show peaks at frequencies corresponding to multiple of 3 times the revolution frequency (i.e. 3P, 6P, 9P, etc) with the largest peak at 3P (approximately 0.42 Hz). At 12P, or approximately 1.7 Hz, another large peak is observed for the detailed model response. This peak represents the free-free mode where the rotor and the generator vibrate in counter-phase, and the ring wheel rotates in counter-phase with the rotor. The peak has moved from 2.19 Hz where it was observed in the stiff turbine case to approximately 1.7 Hz due to the flexibility of the rotor and tower, where the flexibility of the rotor is the main contributor to the lowered frequency. This free-free mode also exists in the normal model, however, obviously the amplification at this frequency is smaller for the normal model. The reasons for this discrepancy are the lack of damping in the detailed model which, if included, would result in a lower peak, and off course that the two models are in fact different.

It is also noticed by comparing the two power spectra for the detailed model in Figure 9-3 and Figure 9-4 that the power spectra are similar at high frequencies which implies that the shaft moment is transferred directly to the tower top via the ring of the gearbox, as expected.

Figure 9-3: Comparison between shaft torque for normal and detailed aeroelastic model.

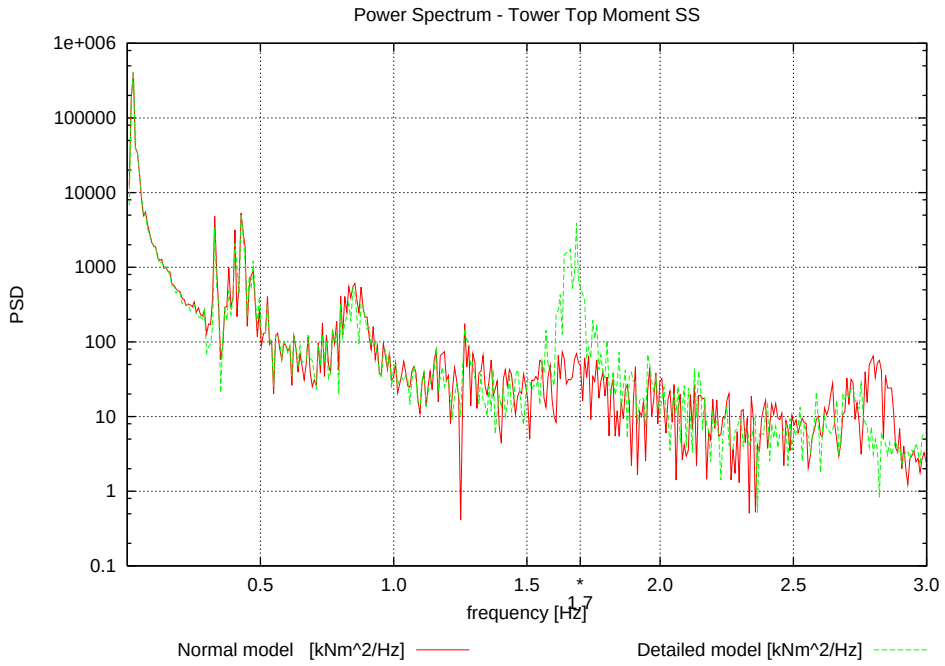

Figure 9-4: Comparison between tower top bending moment (side-to-side) for normal and detailed aeroelastic model.

9.5 Gearbox support flexibility

Also, the influence from the gearbox support flexibility was investigated

An assessment of the influence of the support flexibility (and inertia) associated with the ring wheel attachment to the rest of the structure has been made based on the simple three DOF model described in Section 9.4. This was done by including the support stiffness associated with ring wheel rotation relative to ground as an additional stiffness term in the stiffness matrix.

Three eigenmodes are associated with this three DOF model. The eigenmode with the lowest frequency is the free rotating mode at 0 Hz where the ratio between the rotation of the rotor and the generator is equal to the gear ratio. Besides from this eigenmode, additionally two modes exist which are both free-free modes where the rotor and the generator rotates in counter-phase. The difference between the two modes is the direction in which the ring wheel rotates – for one mode in phase and for the other in counter-phase with the rotor.

What this additional stiffness is actually equal to for a real turbine depends on how the gearbox is mounted to the rest of the structure. If the support stiffness is infinitely high (the gearbox may be mounted directly on the frame) then the ring wheel and the tower top will rotate simultaneously and thus the inertia and stiffness associated with ring wheel rotation will be dominated by the distribution of mass and stiffness in the tower. On the other hand, if the support stiffness is low then the inertia and stiffness associated with ring wheel rotation will be equal to the ring wheel inertia itself and the support stiffness itself. The two non-zero eigenmodes depend highly on this associated inertia and therefore on the support stiffness.

A parameter variation study is made next corresponding to infinitely high support stiffness. The aim is to study Figure 9-1how the dynamics of the support structure affects the rest of the system. In the example the eigenfrequency of the support structure itself is varied across the free-free eigenfrequency of the drivetrain, represented by the label “f” in Figure 9-5 – “f” is equal to the ratio between the eigenfrequency of the support structure itself and the free-free eigenfrequency. It is assumed that the support stiffness is infinitely high and thus that the inertia associated with ring wheel rotation is high – in the example it is of the same order as the modal inertia of the second tower mode and it is kept constant for all parameter variations. The associated stiffness is then varied in order to obtain the eigenfrequency of the support structure itself according to the label “f”.

Figure 9-5 shows the transfer function between the rotor moment input and the internal force between the gear wheels (represented by the spring force in the simplified gearbox model normalized by the same value at 0 Hz), however, this is not really important. The aim of the figure is to show that for realistic values of the tower stiffness and mass, two (free-free-like) eigenfrequencies appear in the low frequency range. From the figure it is seen that the two eigenfrequencies are located on each side of the free-free eigenfrequency (labeled “f=infinity”). It is therefore important that the support flexibility is considered in the design in order to avoid coincidence with resonance frequencies.

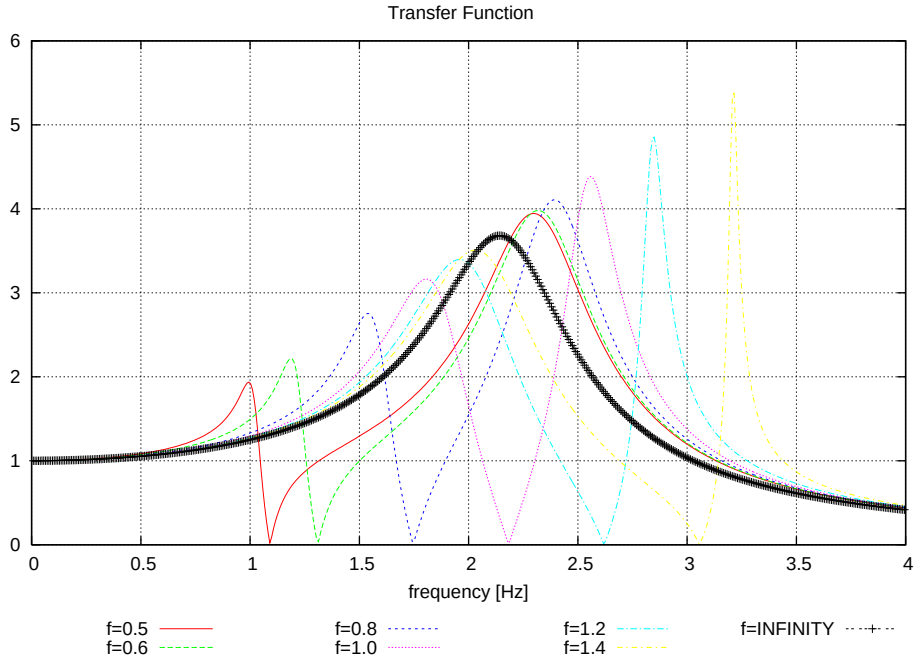

Figure 9-5: Transfer function between the rotor moment input and the internal force between the gear wheels (normalized by the same value at 0 Hz) for different support structure dynamics.

9.6 Conclusion

The main result of the present work is the development of a generalized method to interface dynamic systems to the aeroelastic program HAWC2. The method has been exemplified by modeling the nacelle of an aeroelastic wind turbine model in a more detailed way by including a single planet stage of a gearbox. This simplified gearbox model captures in essence the splitting of the driving torque from the rotor shaft to the frame of the nacelle and to the generator.

The main result of the work is the implementation of a generalized method for interfacing dynamic systems to HAWC2

It has been shown that the inclusion of the simplified gearbox model results in altered dynamics of the nacelle components where the free-free vibration mode of the drive train contributes more to both the shaft torque and the tower top moment responses and therefore also to the internal gearbox stresses.

The results are based on a simplified gearbox model, however, any gearbox model which can be formulated as a set of differential equations can now be interfaced to the aeroelastic model in HAWC2. This makes it possible to base future conclusions on even more detailed gearbox models with more degrees of freedom and to include dynamic models of e.g. the generator and the electrical grid.

Finally, a parameter study of the dynamics of the support structure was made. It was found that for realistic values of mass and stiffness associated with ring wheel rotation, two eigenfrequencies may appear in the low frequency range (both are a kind of free-free modes which differ in the way the ring wheel rotates). This should be considered in the design of the drive train.

10 Influence of wind shear on rotor aerodynamics, power and loads

Helge Aagaard Madsen, Robert Mikkelsen, Niels N. Sørensen, Martin O.L. Hansen, Stig Øye, Jeppe Johansen

10.1 Introduction

Wind shear for the largest wind turbines can be considerable

With the increasing size of wind turbines with rotor diameters for the largest turbines above 120 m, the variation of the mean wind speed over the rotor height due to wind shear can be considerable. As an example the measured wind speed at six different heights at the Test Site of Høvsøre during a period of 1 day is shown in Figure 10-1. During the night a considerable shear is developing with a difference in wind speed of about 5 m/s from height 40 m to 116 m.

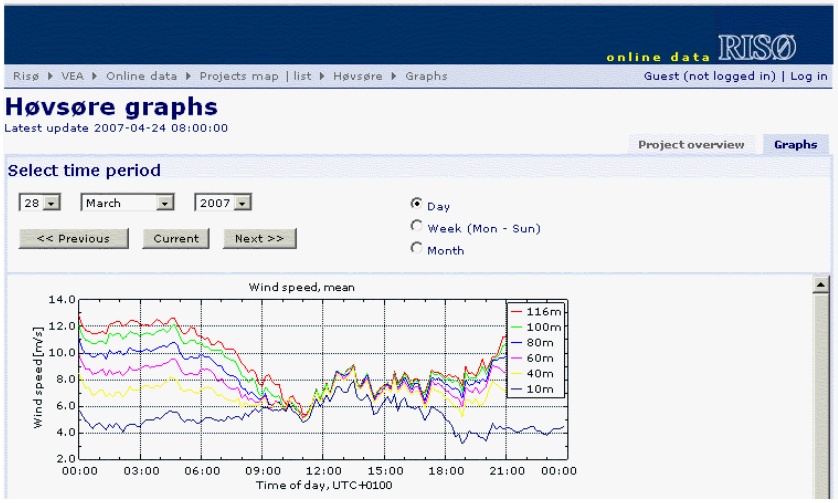

Figure 10-1 Measured wind speed at 6 heights during a period of one day, March 28 2007, (http://veaonline.risoe.dk) .

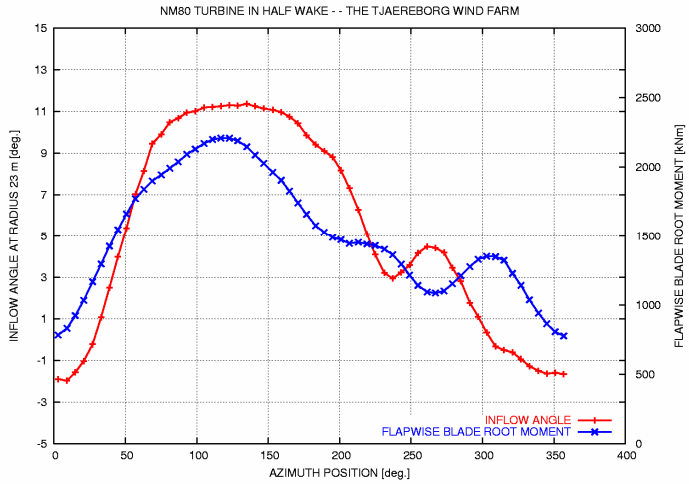

Figure 10-2 Measured inflow angle and flapwise blade root moment on a 2MW NM80 turbine during a half wake situation .

The wind shear results in variations in inflow angle and loads

Likewise, a considerable variation of the inflow to the rotor occurs in wind farms and in particular in half wake situations. The measured local inflow angle on the blade on a NM80 2MW turbine during operation in a half wake is shown in Figure 10-2 together with the flapwise blade root moment. A good correlation between the two signals are seen and the variation in inflow angle from about -1 deg. to 11 deg. indicates a corresponding variation in inflow velocity at the rotor disc of 9 m/s.

The situation with considerable variation of both the instantaneous and the average inflow velocity to the rotor disc is thus quite common for a MW turbine and the question then rises how well this situation is modeled in the common aerodynamic and aeroelastic codes. The blade element momentum model (BEM) is the engineering model for calculation of induction implemented in the aerodynamic and aeroelastic codes such as e.g. FLEX5 and HAWC2 , used by the industry. However, the specific implementation of the BEM model to handle shear in the inflow can be carried in different ways and there is thus an uncertainty in the modeling of this common flow situation. Using more advanced models such as the Actuator Line model or the EllipSys3D code, the flow field and the wake can be computed in much more details and without the assumptions in the BEM modeling. However, modeling or generation of complex shear in the inflow is a complex task but it is expected that the results of these models will hopefully tend to show how the BEM should be implemented to handle the shear in inflow.

Another important aspect is how the turbine control influences the energy capture and the loads in the case with shear in the inflow. One objective with an individual blade control on the turbine could be to maximize the energy capture for strong shear in the inflow. Another strategy could be to alleviate the varying flapwise loads occurring in this situation. Does these two objectives conflict with each other ?

To summarize, the objectives with the present investigation have been:

- clarify the aerodynamic aspects for MW rotors operating in inflow with shear
- investigate the uncertainties in modeling this flow situation
- investigate the aspects of using individual pitch control to 1) optimize power output and 2) alleviate the variation in flapwise loads

The results of the work carried out so far have mainly been within the first two objectives but investigations of the influence of control will be continued within the Aeroelastic Research Programme EFP-2007.

10.2 Approach

The investigations have been carried out using four codes for simulations on the 5MW reference turbine, defined by NREL [1] and used within the UPWIND project. A

A 5 MW turbine was investigated

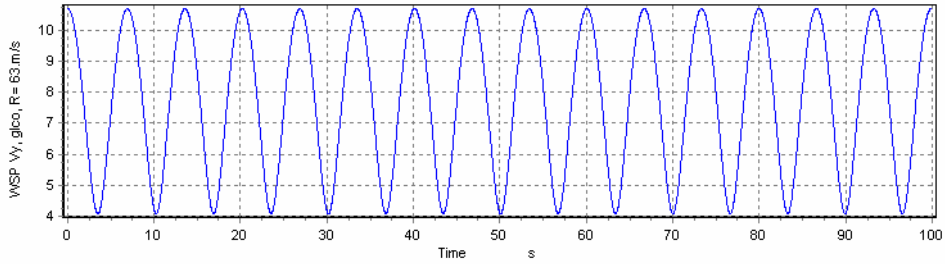

Figure 10-3 The variation in wind speed at the tip of the rotating blade of the 5MW RWT.

strong shear with an exponent of 0.55 for the in inflow has been defined which is a value approximating actual shear profiles measured at Høvsøre[1]. The simulations have been carried out at a single wind speed of 8 m/s at hub height which gives a total variation in inflow at the tip of the blade from 4 m/s to about 11 m/s, Figure 10-3.

Exactly the same airfoil data are used in the different codes and a stiff turbine structure has been assumed. Finnaly. the tilt was set to zero.

The four codes used in the simulations are:

1. EllipSys3D Navier Stokes solver
2. The Actuator Line code
3. FLEX5
4. HAWC2

The simulations with the different codes will be shortly described below and then follows a comparison and discussion of results.

10.3 Simulations with EllipSys3D

Full 3D CFD was used to investigate the wind shear effect

The rotor computations performed with the EllipSys3D code, are all using the same spherical domain. Two series of computations are performed, one for uniform inflow and one for a severe vertical shear at a wind speed of 8 [m/s] at hub height. For all computations the domain is centered on the rotor axis. In order to avoid negative velocities for $z \leq 0$ the power law used to specify the vertical shear profile is blended to a constant velocity profile near the location where the earth surface should have been located, see Figure 10-4.

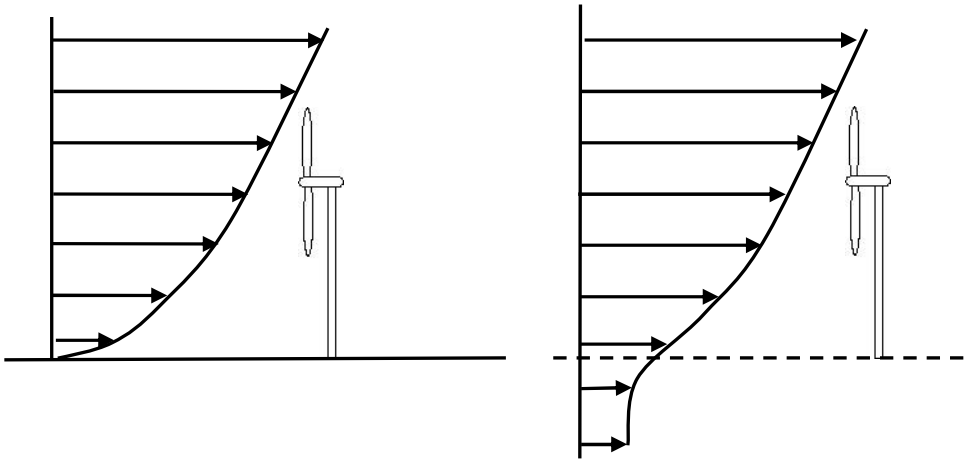

Figure 10-4 To avoid problems with negative velocity below ground level using a spherical domain, the shear profile is blended with a constant velocity profile below terrain level.

The shear profile of the velocity used in the present work is modeled in the following way

1 From communication with Ioannis Antoniou, Risoe National Laboratory.

$$U(z) = U_{hub}\left[\beta(z/z_{hub})^{\alpha} + (1-\beta)\right] \text{ , where } \beta = \begin{cases} 1 & , z \succ z_{\lim} \\ \dfrac{\gamma}{\exp(1.0)}\exp\left(\dfrac{z+z_l}{z_{\lim}+z_l}\right) & , z \le z_{\lim} \end{cases},$$

where U_{hub} = 8 [m/s], α =0.55, z_{hub} = 90[m], z_l = 20 [m], z_{lim} = 25 [m] and γ = 0.75. To assure that the shear layer computations could be performed with the present approach, a single case using the mesh described later with the rotor at zero rotational speed was first computed. This should correspond to the case of a parked rotor, and we should expect very limited disturbance or induction from the rotor. Additionally, it should be possible to verify that the use of laminar conditions together with the high Reynolds number would results in minimal streamwise development of the enforced velocity shear profile. In Figure 10-5 a vertical velocity profile at the symmetry plane of the turbine is shown. In agreement with expectations minimal development is seen from far upstream to far downstream.

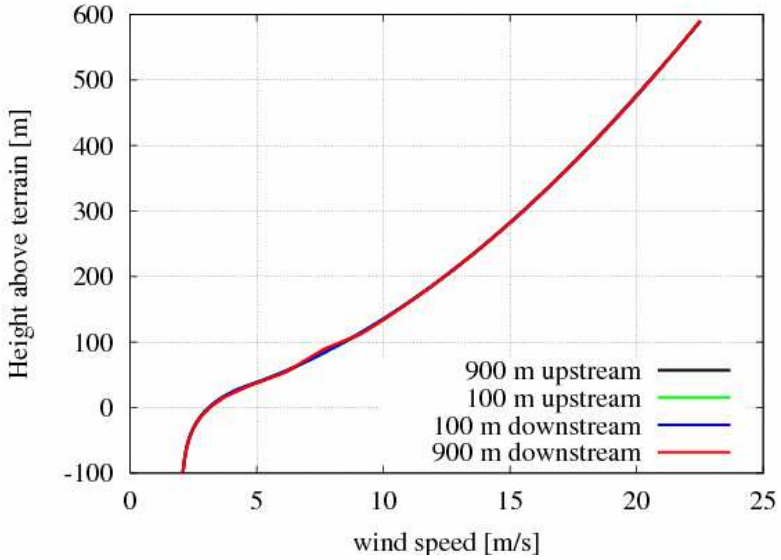

Figure 10-5 The development of the velocity profile from far upstream to far downstream for the case of the parked rotor.

Navier-Stokes Solver

The in-house flow solver EllipSys3D is used in all computations presented in the following. The code is developed in co-operation between the Department of Mechanical Engineering at the Technical University of Denmark and The Department of Wind Energy at Risø National Laboratory, see [2],[3],[4]. The EllipSys3D code is a multiblock finite volume discretization of the incompressible Reynolds Averaged Navier-Stokes (RANS) equations in general curvilinear coordinates. The code uses a collocated variable arrangement, and Rhie/Chow interpolation [5] is used to avoid odd/even pressure decoupling. As the code solves the incompressible flow equations, no equation of state exists for the pressure, and in the present work the PISO algorithm of Issa [6] is used to enforce the pressure/velocity coupling. The EllipSys3D code is parallelized with MPI for executions on distributed memory machines, using a non-overlapping domain decomposition technique.

Both steady state and unsteady computations can be performed. For the unsteady computations the solution is advanced in time using a 2nd order iterative time-stepping (or dual time-stepping) method. In each global time-step the equations are solved in an

iterative manner, using under relaxation. First, the momentum equations are used as a predictor to advance the solution in time. At this point in the computation the flowfield will not fulfil the continuity equation. The rewritten continuity equation (the so-called pressure correction equation) is used as a corrector making the predicted flowfield satisfy the continuity constraint. This two step procedure corresponds to a single sub-iteration, and the process is repeated until a convergent solution is obtained for the timestep. When a convergent solution is obtained, the variables are updated, and we continue with the next timestep.

For steady state computations, the global time-step is set to infinity and dual time stepping is not used, this corresponds to the use of local time stepping. In order to accelerate the overall algorithm, a multi-level grid sequence is used in the steady state computations. The convective terms are discretized using a third order QUICK upwind scheme, implemented using the deferred correction approach first suggested by Khosla and Rubin [7]. Central differences are used for the viscous terms, in each sub-iteration only the normal terms are treated fully implicit, while the terms from non-orthogonality and the variable viscosity terms are treated explicitly. Thus, when the sub-iteration process is finished all terms are evaluated at the new time level.

In the present work the turbulence in the boundary layer is modeled by the k-ω SST eddy viscosity model [8]. The equations for the turbulence model are solved after the momentum and pressure correction equations in every sub-iteration/pseudo time step.

The three momentum equations are solved decoupled using a red/black Gauss-Seidel point solver. The solution of the Poisson system arising from the pressure correction equation is accelerated using a multigrid method. In order to accelerate the overall algorithm, a multi-level grid sequence and local time stepping are used.

For the rotor computations with uniform inflow a steady state moving mesh approach is used [9], while for the shear layer computation a standard moving mesh formulation in a fixed frame of reference is used [10]. The moving mesh option has been implemented in the EllipSys3D solver in a generalized way allowing arbitrary deformation of the computational mesh, following [11]. It has been used for doing unsteady simulations for several years both for stiff rotors in yaw and fully coupled aeroelastic computations [9, 12, 13, 14]. For the present application of rotor in a shear flow, special care has to be taken with respect to the dependency of the inflow of the height over terrain, making the velocity at the inflow change when the mesh is rotated and thereby changing the physical location of the boundary points

Computational Grid

The rotor used in the present work, is designed in connection with the European UPWIND project, it is a three bladed rotor with a diameter of 126 meters, where the inner part of the blade uses DU airfoils and the outer part features the NACA64-XXX airfoils. The actual rotor design is heavily inspired by the design of the LM 61.5 rotor, see [1].

Typically, computations of rotor power using CFD are performed for uniform inflow allowing the computations to exploit the periodicity in the azimuth direction. For turbines operating in the upwind configurations, the assumption that the effect of the tower and the nacelle are weak and can be neglected is typically used. In the present work only the rotor is modeled, but as we are investigating a case where non-uniform inflow are present, the full three bladed rotor is modeled. Based on experience with

previous airfoil and rotor computations, 256 cells are distributed around the blade in chordwise direction, while 128 cells are used in the spanwise direction, and a square block of 64x64 cells are used at the blade tip to close the O-mesh 'tube', see Figure 10-6 left. In the normal direction 128 cells are used to march the grid to the farfield, starting with a cells size at the blade surface of ~$1x10^{-5}$ [m] assuring that the y+ is below two for the total blade surface. The total number of cells for the full three bladed rotor is around 14 million cells, and the outer boundary is placed ~10 rotor diameters away from the rotor centre.

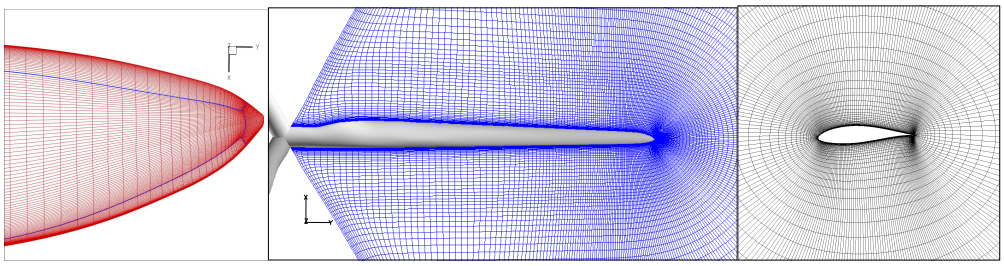

Figure 10-6 The square tip block (left picture), the spanwise resolution around the blade (centre picture), and the o-mesh around the chord (right picture).

At the blade surface no-slip wall boundary conditions are specified, while most of the outer boundary is specified as inflow conditions with the velocity prescribed in accordance with the undisturbed flow velocity, either uniform or given by the shear layer velocity profile. The remaining part of the outer boundary is specified as outlet conditions, where all flow quantities except the pressure is specified as fully developed, see Figure 10-7.

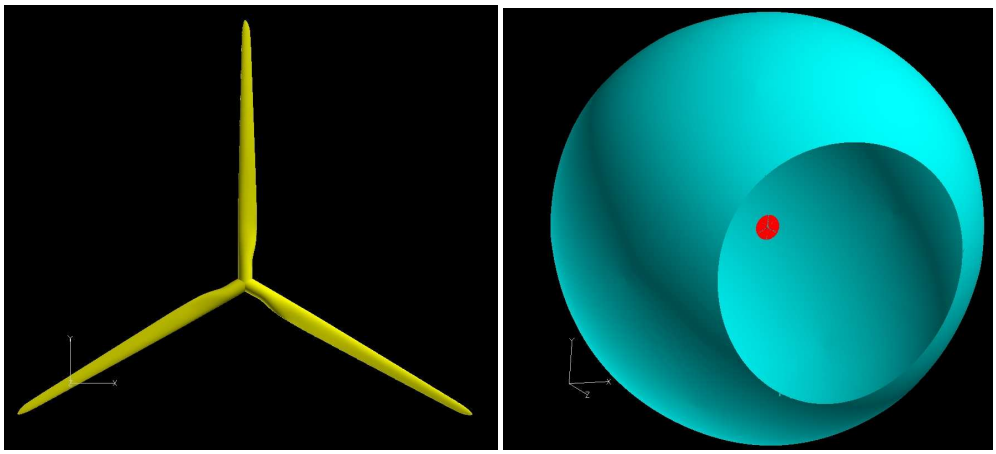

Figure 10-7 The three bladed UPWIND rotor, having a rotor diameter of 126 meter (left), and the full domain used for the rotor computations (right). The rotor disc is indicated in red to increase visibility; the inlet part of the outer spherical boundary is indicated in blue, while the remaining part of the spherical boundary is specified at outlet.

10.4 Simulations with the Actuator Line model

Also, an actuator line model was used to investigate the wind shear

The ACL method is based on solving the full Navier-Stokes equations including concentrated body forces (actuator lines) representing the aerodynamic loads from the blades. The computational domain extends many rotor diameters in all directions with boundaries typically 5-10 diameters away. Inflow settings are controlled by applying

appropriate conditions at the inflow boundary however, in order to include effects of wind shear in the flow modeling; a refined approach outlined below is needed.

Modeling of arbitrary wind shear, including wind direction

Flow over surfaces (ground) simulated by solving the Navier-Stokes with a turbulence model provides one with a range of wind profiles, but if an arbitrary steady wind profile is desired (preferably a profile obtained from measurements) turbulence modeling is not sufficient. In the present project a method has been developed in order to be able to impose "any" arbitrary steady wind shear profile including directional changes in flat terrain. Turbines operating in wind shear with substantial directional variation with height are not uncommon. Normally variations are small like 3-5^o across the rotor area but variation up 40^o between top and bottom has been reported. The basic idea is to use momentum sources applied to all computational cells in such a way that a desired wind shear profile is obtained everywhere in the computational domain. The approach is in essence straight forward. The momentum source field is found iteratively and since the wind shear profile is chosen by the user, a well-defined target is given and the momentum sources are simply adjusted until the desired profile is obtained. Convergence is generally good. Figure 10-8 shows an example of a wind shear profile including directional changes from the ground and upwards.

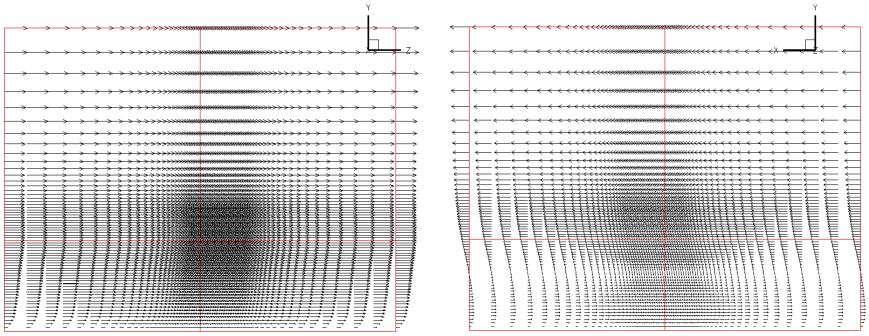

Figure 10-8 Steady wind shear profile including directional changes, (left) seen from the side, (right) seen in the main flow direction.

Initial suggestions proposed only to use the boundary conditions to impose a specific wind shear profile; however, as Figure 10-9 (left) shows using boundary conditions only does not fully insure that a desired profile is obtained.

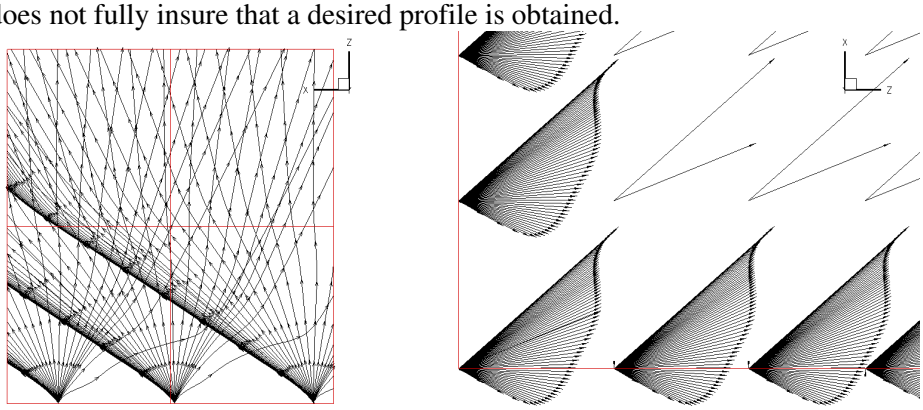

Figure 10-9 The streamlines (left) are seen from above starting at different heights on the inflow boundary. The streamlines are seen not all to be straight in the lower part of the domain since only boundary conditions are used, no momentum sources. The velocity profile (right) is seen from above, changes direction about 60^o in total from ground to the top of the domain.

The flow solver simply alters the imposed initial flow field mainly due to the numerical capability of the solver. It should be emphasized that the method proposed basically bypasses actual physically modeling of wind shear profiles. Actual wind shear profiles depends on numerous factors like stratification, temperature, Coriolis force, etc. which in the present modeling all are accounted for artificially by the use of momentum sources. Thus, the procedure in connection with ACL computation is first to obtain a converged solution for the desired wind shear profile only and second, restart the simulation with the ACL method turned on. The artificial force field varies through the domain depending on grid structure and imposed wind shear profile, however, the magnitude is generally found to be between 3-4 orders of magnitude smaller than the level of the ACL forces. A careful analysis (details not shown) on the Navier-Stokes equations directly shows that the error associated with the proposed method scales inversely with the applied Reynolds number. Thus, the Reynolds number should not be too small. Figure 10-10 shows shed vorticity contours from the tip and root of the ACL of a turbine inserted into the above wind shear with directional variations too. The transported wake is skewed forming a more and more elongated elliptic shape.

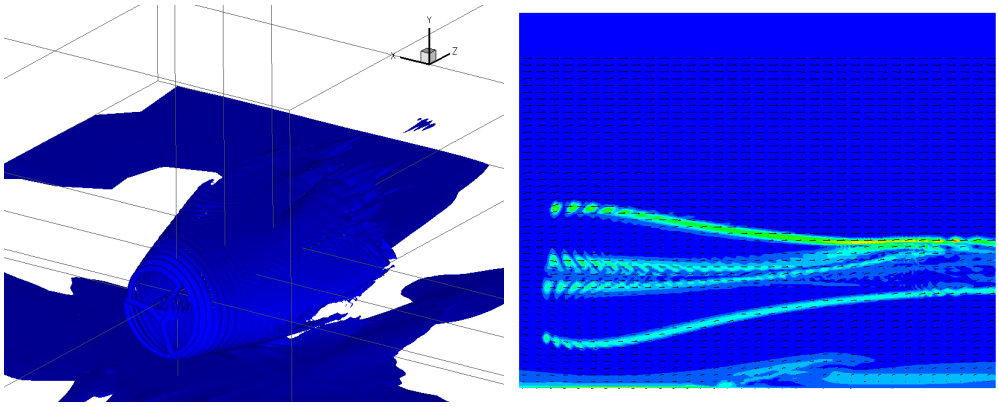

Figure 10-10 Shed vorticity from the ACL oprating in wind shear with wind directional change. The wake (left) is skewed forming a more and more elongated elliptic shape as it convects downstream. The sliced view through the rotor center (right) shows the development of velocity vectors and vorticity. The wake appers to narrow downstream but infact the elliptic shape of the wake is resposible for the appearance.

The method appears promising with respect to handle arbitrary wind shear profiles, however, presently further analysis on loadings, induced velocities, etc., has not been carried out in detail for the case including directional changes.

Computations on the NREL 5MW RWT

Computation on the 5MW RWT has been carried out using the parameters outlined in section 10.2. Figure 10-11 depicts views of the formed wake at 8m/s and extreme shear with an exponent of 0.55. The center of the rotor is located at 1.4 radii.

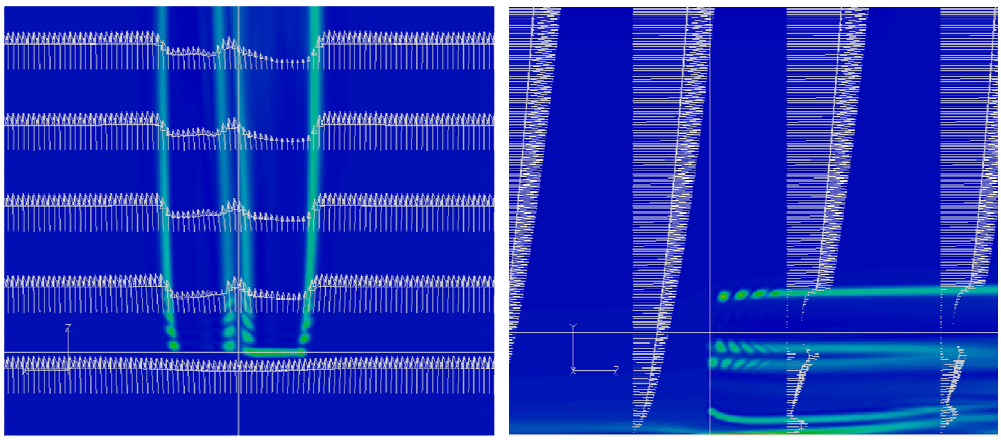

Figure 10-11 Horizontal (left) and side (right) view of wake. Seen from above the difference in induced velocities between the upward and downward rotating blade is evident. The side view also captures the formation of the decelerated wake and furthermore reveals some interaction with the ground boundary layer.

The comparison presented in Section 10.7 between the different codes indicates a distinct behavior near the tip using the ACL method, which address questions to how tip-correction is handled. Tip correction is accounted for in a comparable manner as compared to BEM using a refined procedure [15]. The main difference between BEM and ACL when handling tip correction is that using the ACL method, the flowfield is given and the loading has to be modified in contrast to the BEM method where the induced velocities are found directly from the iterative solution procedure. Other tip correction methods have been developed (Shen[16,17]) which predicts better in the in the tip region however presently, improvements to the current model remains to be implemented into the ACL method.

10.5 BEM implementation in FLEX5 with respect to shear

The implemented wind shear model in FLEX5 operates in a manner where the induced velocity remains unaffected. This is clearly seen from figures 1.13-1.14 where the blade at top and bottom position predicts exactly the same variation of the induced velocities.

10.6 BEM implementation in HAWC2 with respect to shear

In HAWC2 the induction is computed in the grid points of a non-rotating grid perpendicular to the shaft, at each time step. The grid points are the intersections between the radial lines and the circular lines in Figure 10-12.

Two aeroelastic codes, FLEX5 and HAWC2, were used in the wind shear investigation

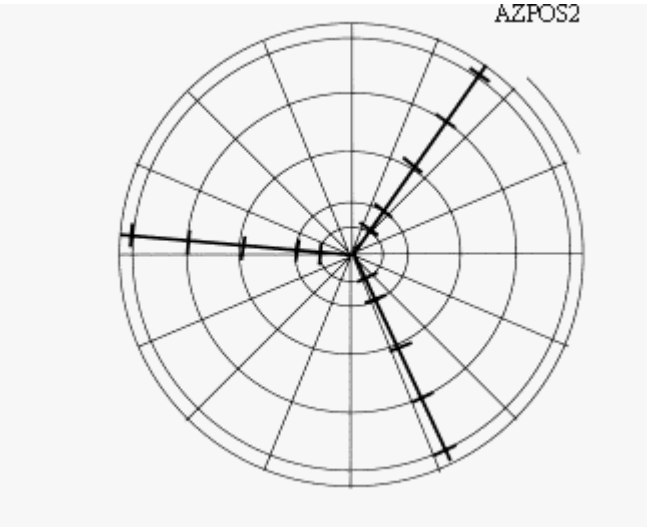

Figure 10-12 The induction is computed in a non-rotating grid at each time step.

We define in each grid point the local thrust coefficient $CT_G(\psi_G, r)$ and the local torque coefficient $CQ_G(\psi_G, r)$ and they are found by linear interpolation from the similar coefficients $CT_B(\psi_B, r)$ and $CQ_B(\psi_B, r)$ at the adjacent blade points (ψ_B, r).

$CT_B(\psi_B, r)$ is computed as:

$$CT_B(\psi_B, r) = \frac{dT_B(\psi_B, r)}{\frac{1}{2}\rho V_{\infty-av}^2 \, 2\pi r \, dr} = \frac{\frac{1}{2}\rho W^2 C_y(\psi_B, r) c B \, dr}{\frac{1}{2}\rho V_{\infty-av}^2 \, 2\pi r \, dr} \Rightarrow$$

$$CT_B(\psi_B, r) = \frac{W^2 C_y(\psi_B, r) c B}{V_{\infty-av}^2 \, 2\pi r} \tag{9.1}$$

where $V_{\infty-av}$ is the average, free stream velocity found as the average inflow velocity over all the grid points, W is the relative velocity at the blade section, c is the local chord length, B is number of blades and $C_y(\psi_B, r)$ is the projection of $C_L(\psi_B, r)$ and $C_D(\psi_B, r)$ for the blade on the non-rotational grid at the point of the blade section.

Likewise the torque coefficient $CQ_B(\psi_B, r)$ is computed as:

$$CQ_B(\psi, r) = \frac{dQ_B(\psi_B, r)}{\frac{1}{2}\rho V_{\infty-av}^2 \, r \, 2\pi r \, dr} = \frac{\frac{1}{2}\rho W^2 C_x(\psi_B, r) c B r \, dr}{\frac{1}{2}\rho V_{\infty-av}^2 \, r \, 2\pi r \, dr} \Rightarrow$$

$$CQ_B(\psi_B, r) = \frac{W^2 C_x(\psi_B, r) c B}{V_{\infty-av}^2 2\pi r} \tag{9.2}$$

where $C_x(\psi_B, r)$ is the projection of $C_L(\psi_B, r)$ and $C_D(\psi_B, r)$ for the blade on the tangential direction to the non-rotating grid at the point of the blade section. By interpolation in azimuth direction from the blade calculation points to the grid points, $CT_G(\psi_G, r)$ and $CQ_G(\psi_G, r)$ are derived.

Momentum theory relates CT with the induction a:

$$CT = 4a(1-a) \tag{9.3}$$

and at high loading we have the Glauert empirical relation. On basis of these two relations we write the relation between *a* and *CT* on the following polynomial formal:

$$a_G(\psi_G, r) = k_3 CT_G{}^3(\psi_G, r) + k_2 CT_G{}^2(\psi_G, r) + k_1 CT_G(\psi_G, r) + k_0 \tag{9.4}$$

and the tangential induction is found as:

$$a_{mG}(\psi_G, r) = CQ_G(\psi_G, r) \frac{V_{\infty-av}}{4r(1 - a_G)\Omega} \tag{9.5}$$

The filtering for dynamic inflow is now performed and then the induction $a_B(\psi_B, r), a_{mB}(\psi_B, r)$ factors at the blade calculation points (ψ_B, r) are found by interpolation from the induction at the grid points. Finally, the induced velocities $u_{axB}(\psi_B, r), u_{\tan B}(\psi_B, r)$ are derived as:

$$u_{axB}(\psi_B, r) = a_B(\psi_B, r) V_{\infty-av} \tag{9.6}$$

and

$$u_{\tan B}(\psi_B, r) = a_{mB}(\psi_B, r) \Omega r \tag{9.7}$$

The characteristics of this implementation of BEM with respect to wind shear is that the local thrust coefficient is based on the local loads of the blade at this specific point but normalized with an average, free stream velocity $V_{av-\infty}$, which is the average over the whole rotor disc. The final induced velocity will thus vary along the blade as function of azimuth position of the blade.

10.7 Results and discussions

A comparison of integrated quantities for the whole rotor computed with the different models is shown in Table 10-1. For the case of no shear there is a very good correlation between the two codes based on the BEM modeling (FLEX5 and HAWC2) whereas the

results from the two more advanced codes are above and below, respectively. However, it should be noted that the airfoil data used in the BEM computations and in the ACL model have not been calibrated and the 3D corrections applied to the data on the inner part of the rotor seems to overestimate the performance of the airfoils.

The effect of wind shear is seen to cause different influence on the power. HAWC2 computes a reduction in power whereas FLEX5 computes a small increase. Likewise EllipSys3D also computes a small reduction in power whereas the ACL model computes a considerable increase. A clear tendency for the influence of the wind shear on rotor power coefficient can thus not bee extracted from the results. In Table 10-1 is also shown the maximum and minimum flapwise moment and also for these quantities a considerable deviation is seen.

Table 10-1 Comparison of electrical power and flapwise loads at 8 m/s.

	El. power [kW] no shear	El. power [kW] shear	max. Flap. Moment [kNm]	min. Flap. moment [kNm]
HAWC2	**1906**	**1812**	**6306**	**3785**
EllipSys3D	**1867**	**1830**	**6295**	**1867**
FLEX5	**1900**	**1932**	**6677**	**3100**
AC-Line	**1995**	**2135**	**6860**	**3700**

Comparing the results from the different codes show no distinct picture of the influence of wind shear

A comparison of the normal and tangential force distribution along the blade is shown in the next figures from Figure 10-13 to Figure 10-18 for the blade in upward and downward position, respectively. In particular there is a considerable difference in the tangential load and unfortunately the advanced models do not correlate very well and do not give a clear indication of what is the correct result.

In the last two figures the axial induced velocity is shown and again for the blade in upward and downward position, respectively. The BEM model implementation in the FLEX5 code gives the same induction for the blade in the two position whereas the BEM implementation in HAWC2 gives a higher induction for the blade pointing upwards than for the blade pointing downwards. Comparing with the result of the ACL model it is seen that this model predicts a higher induction for the blade pointing upwards than for the blade pointing downwards but not as much as predicted with HAWC2.

10.8 Conclusions

The investigation of the influence of wind shear in the inflow has shown that there is a considerable uncertainty in modeling this rather common inflow case for a rotor. The implementation of the BEM model to handle this flow case can be carried out in different ways and the results of two advanced models have not so far indicated what the correct results are.

In the new Aeroelastic Research Programme EFP2007 the investigations will be continued and the aspect of influence of individual pitch control on the blades will also be considered.

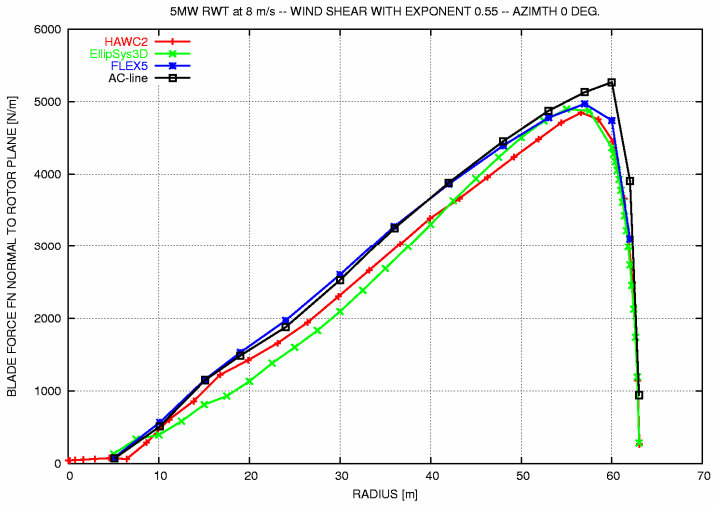

Figure 10-13 Comparison of the normal force distribution for the blade vertical upwards (0 deg. azimuth).

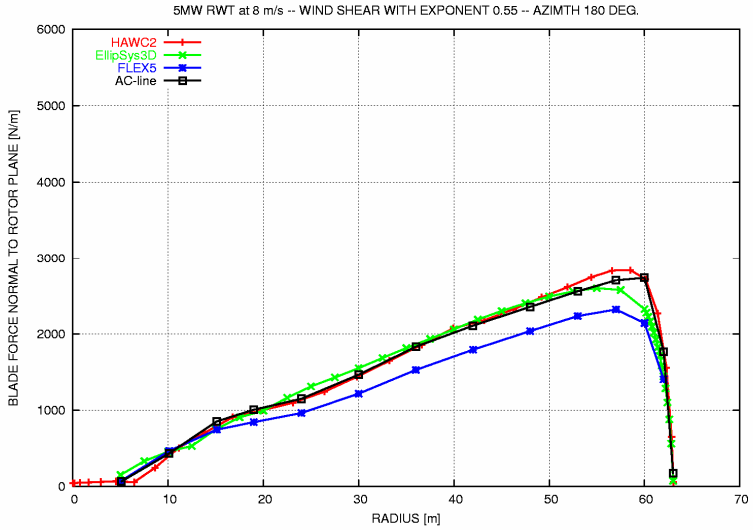

Figure 10-14 Comparison of the normal force distribution for the blade vertical downwards (180 deg. azimuth).

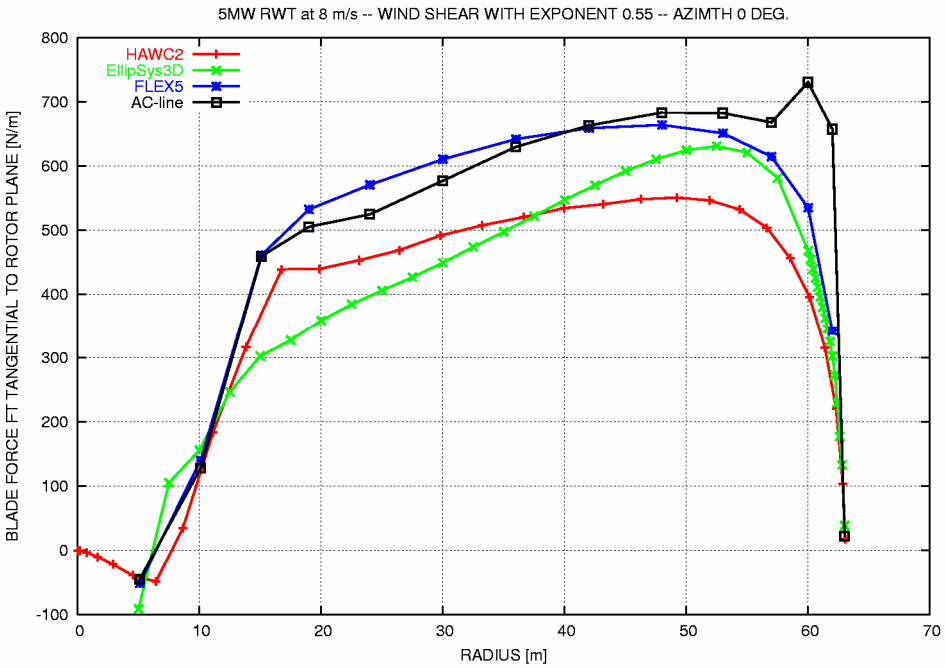

Figure 10-15 Comparison of the tangential force distribution for the blade vertical upwards (0 deg. azimuth).

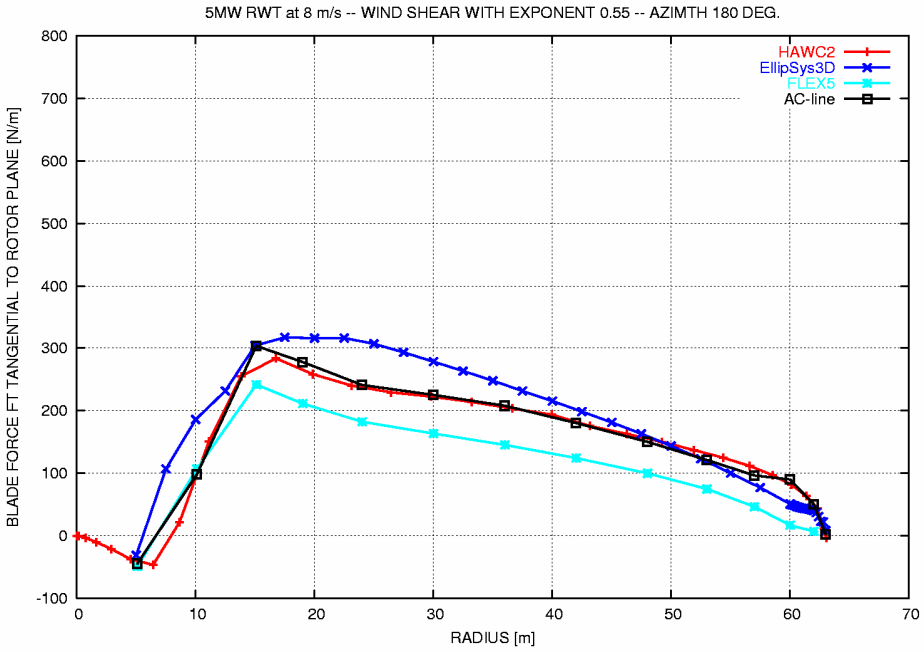

Figure 10-16 Comparison of the tangential force distribution for the blade vertical downwards (180 deg. azimuth).

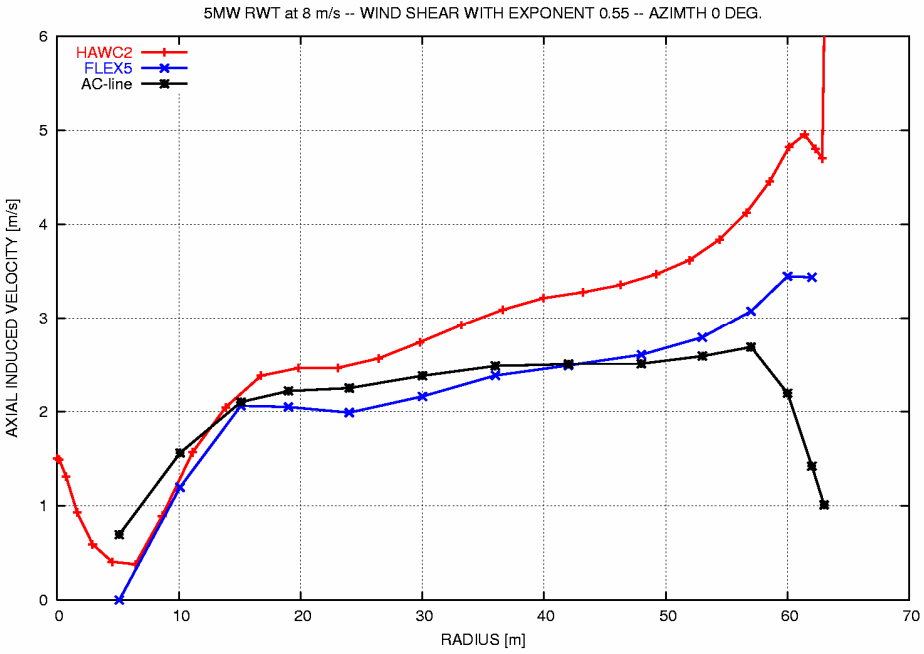

Figure 10-17 Comparison of the axial induced velocity distribution for the blade vertical upwards (0 deg. azimuth).

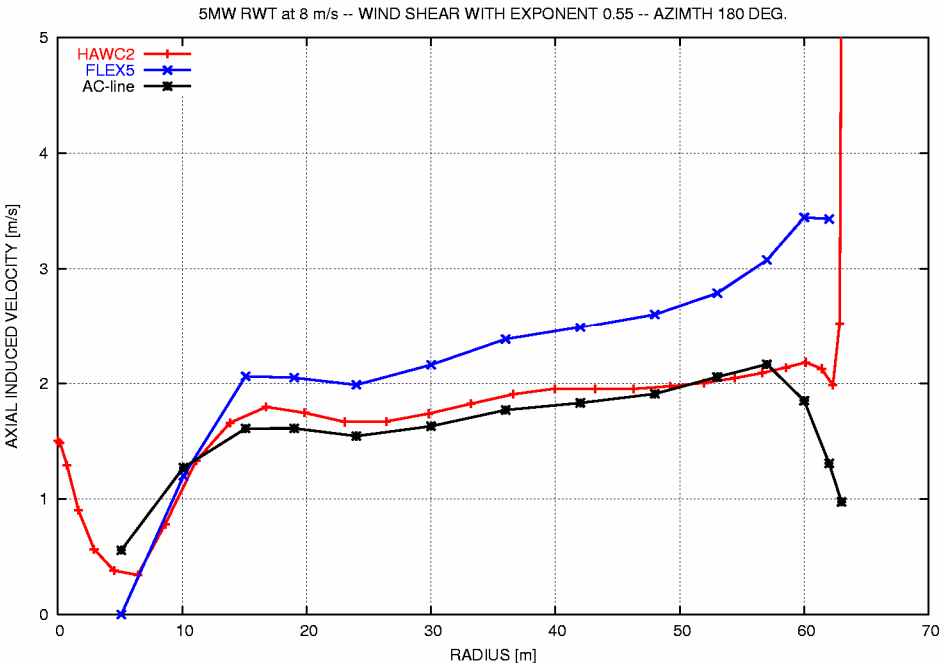

Figure 10-18 Comparison of the axial induced velocity distribution for the blade vertical downwards (180 deg. azimuth).

10.9 References

[1] Jonkman, J., IEA Annex XXIII document on NREL´s baseline wind turbine aeroelastic model. NREL/NWTC, August 11, 2005.

[2] Michelsen, J.A.. Basis3D - a Platform for Development of Multiblock PDE Solvers. Technical Report AFM 92-05, Technical University of Denmark, 1992.

[3] Michelsen J.A., ”Block structured Multigrid solution of 2D and 3D elliptic PDE's”, Technical Report AFM 94-06, Technical University of Denmark, 1994.

[4] Sørensen, N.N.. General Purpose Flow Solver Applied to Flow over Hills. Risø-R-827-(EN), Risø National Laboratory, Roskilde, Denmark, June 1995.

[5] Rhie C.M. ”A numerical study of the flow past an isolated airfoil with separation” Ph.D. thesis, Univ. of Illinois, Urbane-Champaign, 1981.

[6] Issa R.I. Solution of the implicitly discretised fluid flow equations by operator-splitting’ J. Comp. Pys., 61, 1985

[7] Khosla P.K. and Rubin S.G., ”A diagonally dominant second-order accurate implicit scheme”, Computers Fluids, 2:207-209, 1974.

[8] Menter F.R., ”Zonal Two Equation k-ω Turbulence Models for Aerodyanmic Flows”. AIAA-paper-932906, 1993.

[9] Sørensen, N.N., Rotor computations using a 'Steady State' moving mesh. IEA Joint Action Committee on aerodynamics, Annex XI and 20. Aero experts meeting, Pamplona (ES), 25-26 May 2005.

[10] Sørensen, N.N.; Michelsen, J.A., and Schreck S.,Application of CFD to Wind Turbine Aerodynamics. In: CD-Rom proceedings. 4. GRACM congress on computational mechanics, Patras (GR), 27-29 Jun 2002. Tsahalis, D.T. (ed.), (Greek Association of Computational Mechanics, [s.l.], 2002) 9 p.

[11] Demirdzic, I., Peric, M. (1988): Space conservation law in finite volume calculations of fluid flow. Int. J. Numer. Methods Fluids, 8, 1037-1050.

[12] Madsen, H.A.; Sørensen, N.N.;Schreck, S.,YAW AERODYNAMICS ANALYZED WITH THREE CODES IN COMPARISON WITH EXPERIMENT, 22rd ASME Wind Energy Symposium, RENO NV(US), 6-9 Jan 2003.

[13] Bertagnolio, F.; Gaunaa, M.; Hansen, M.; Sørensen, N.N.; Rasmussen, F., Computation of aerodynamic damping for wind turbine applications. In: CD-Rom proceedings. 4. GRACM congress on computational mechanics, Patras (GR), 27-29 Jun 2002. Tsahalis, D.T. (ed.), (Greek Association of Computational Mechanics, [s.l.], 2002) 8 p.

[14] Bertagnolio, F.; Gaunaa, M.; Sørensen, N.N.; Hansen, M.; Rasmussen, F., Computation of Modal Aerodynamic Damping Using CFD, 22rd ASME Wind Energy Symposium, RENO NV(US), 6-9 Jan 2003.

[15] Mikkelsen R. Actuator disc methods applied to wind turbines. *Ph.D. dissertation*, MEK-FM-PHD-2003-02, 2003, http://www.fm.mek.dtu.dk/English/Publications/PHDtheses.aspx

[16] Shen WZ, Mikkelsen R, Sørensen JN, Bak, Chr. Tip loss corrections for wind turbine computations. *Wind Energy*, 2005;**8**:457-475

[17] Shen WZ, Sørensen JN, Mikkelsen R. Tip loss corrections for actuator/Navier-Stokes computations. *J. Solar Energy Eng.*, May 2005;**127**:209-213

11 References

11.1 Journal papers

Hansen, M.O.L., Sørensen, J.N., Voutsinas, S., Sørensen, N. and Madsen, H.Aa. (2006) "State of the art in wind turbine aerodynamics and aeroelasticity". Progress in Aerospace Sciences, vol. 42, pp. 285-330.

Hansen, M.H., "Aeroelastic Instability Problems for Wind Turbines", (Submitted)

J. Johansen, H.Aa. Madsen, M. Gaunaa, N.N. Sørensen and C. Bak, "Design of a Wind Turbine Rotor for Aerodynamically Maximum Efficiency", Wind Energy Journal, submitted for publication.

Okulov, V. L. and Sørensen, J. N. (2007) "Stability of helical tip vortices in a rotor far wake". Journal of Fluid Mechanics, vol. 576, pp. 1-25.

Sørensen, J.N., Shen, W.Z. and Mikkelsen, R. (2006), "Wall Correction Model for Wind Tunnels with Open Test Section". AIAA Journal, vol. 44, no. 8, pp. 1890-1894.

11.2 Conference papers

Bak, C.; Gaunaa, M.; Antoniou, I., Performance of the Risø-B1 airfoil family for wind turbines. In: Wind energy. Proceedings of the Euromech colloquium. EUROMECH colloquium 464b: Wind energy. International colloquium on fluid mechanics and mechanics of wind energy conversion, Oldenburg (DE), 4-7 Oct 2005. Peinke, J.; Schaumann, P.; Barth, S. (eds.), (Springer, Berlin, 2006) p. 231-234

Bechmann, A.; Sørensen, N.N.; Johansen, J., Atmospheric flow over terrain using hybrid RANS/LES (Invited Paper and Presentation). In: Scientific proceedings. 2007 European Wind Energy Conference and Exhibition, Milan (IT), 7-10 May 2007. (2007) p. 9-19

Hansen, M.H. and Kallesøe, B.S., "Servo-Elastic Dynamics of Wind Turbine Blades with Large Deflections, Pitch Actuator Feedback and Pitch Bearing Friction", (To be presented at TWIND 2007)

Johansen, J., Madsen, H.A., Gaunaa, M., Sørensen, N.N. and Bak, C., "3D Navier-Stokes Simulations of a rotor designed for aerodynamically maximum efficiency", 26th ASME Wind Energy Symposium, 8-11 January, 2007, Reno, Nevada, USA

Johansen, J. and Sørensen, N.N., "Numerical Analysis of Winglets on Wind Turbine Blades using CFD", EWEC 2007, Milan, Italy, 7.-10. May, 2007.

Larsen, G.C.; Madsen, H.Aa.; Thomsen, K.; Larsen, T.J., Wake meandering - a pragmatic approach. International Energy Agency, Annex XXIII: Workshop on wake modelling and benchmarking of models, Billund (DK), 6-7 Sep 2006. Unpublished.

Larsen, T.J.; Aagaard Madsen, H.; Thomsen, K.; Rasmussen, F., Reduction of teeter angle excursions for a two-bladed downwind rotor using cyclic pitch control (Invited Paper and Presentation). 2007 European Wind Energy Conference and Exhibition, Milan (IT), 7-10 May 2007. Unpublished.

Madsen, H.A., Johansen, J., Sørensen, N.N., Larsen, G.C. and Hansen, M.H. "Simulation of Low Frequency Noise from a Downwind Wind Turbine Rotor". Presented at the 45th AIAA Aerospace Sciences Meeting and Exhibit, held at Grand Sierra Resort Hotel ,8 - 11 Jan 2007 Reno, Nevada.

Madsen, H.A., Johansen, J., Bak, C., Mikkelsen, R., and Øye, S. " Detailed Investigation of the Blade Element Momentum (BEM) Model based on analytical and numerical results and proposal for modifications of the BEM Model". To be presented at the conference TWIND2007 to be held at DTU in August 2007.

Madsen, H.A., The potential of reducing teeter angle amplitude and blade loads by using the delta3 coupling on an two-bladed teetering MW rotor (Invited Poster). 2007 European Wind Energy Conference and Exhibition, Milan (IT), 7-10 May 2007. Unpublished.

Mikkelsen R, Sørensen JN, Troldborg N. "Prescribed wind shear modeling combined with the actuator line technique", EWEC 2007, Milan, Italy, 7-10May, 2007.

Sørensen, N.N. and Johansen, J., "UPWIND, Aerodynamics and aero-elasticity. Rotor aerodynamics in atmospheric shear flow", EWEC 2007, Milan, Italy, 7.-10. May, 2007

Zahle, F.; Johansen, J.; Sørensen, N.N., Wind turbine aerodynamics using an incompressible overset grid method (Invited Paper and Presentation). In: Scientific proceedings. 2007 European Wind Energy Conference and Exhibition, Milan (IT), 7-10 May 2007. (2007) p. 9-19

11.3 Reports

Bertagnolio, F.; Sørensen, N.N.; Johansen, J., Profile catalogue for airfoil sections based on 3D computations. Risø-R-1581(EN) (2006) 72 p.

Larsen, T.J. How to HAWC2 - the users manual. Risø National Laboratory (DK). WInd Energy Department - Technical university of Denamark. Risø-R-1597(en) (2007)

11.4 Lectures

Hansen, M.H., "How hard can it be to pitch a wind turbine blade?", 11th DCAMM symposium, Silkeborg, 19-21 March 2007.

Landberg, L.; Rasmussen, F., Forskningscenter Risø. Forskning indenfor vindenergi - nyeste resultater indenfor meteorologi og aeroelasticitet. Vinddag 2006, Dansk Forskningskonsortium for Vindenergi, Risø (DK), 21 Nov 2006. Unpublished.

Rasmussen, F., Aerodynamics and aeroelastics (Invited Presentation). 2007 European Wind Energy Conference and Exhibition. UpWind workshop, Milan (IT), 10 May 2007. Unpublished.

Sørensen, J.N., Mikkelsen, R. and Troldborg, N. (2007), "Modelling of Wind Turbine wakes", Lecture Note at the von Karman Institute for Fluid Dynamics, March 19-23, 2007, 31 pages.

Sørensen, J.N., 'Wind Turbine Wake Structures', Invited lecture at the 6th Euromech Fluid Mechanics Conference, Stockholm, June 26-30, 2006.

Zahle, F., Bladtårn interaktion. Vinddag 2006, Dansk Forskningskonsortium for Vindenergi, Risø (DK), 21 Nov 2006. Unpublished.

Risø's research is aimed at solving concrete problems in the society.

Research targets are set through continuous dialogue with business, the political system and researchers.

The effects of our research are sustainable energy supply and new technology for the health sector.

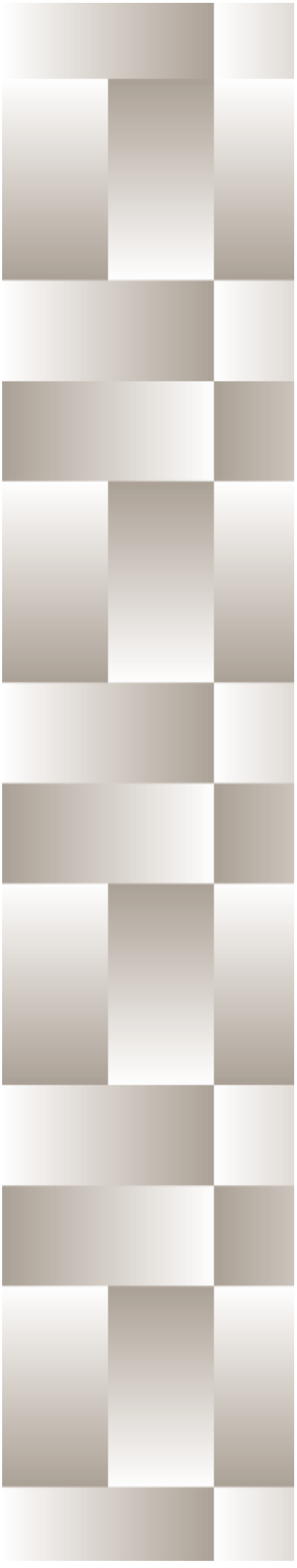

www.risoe.dk